

# Optimal Robust Output-tracking of Autonomous Rovers with Dynamic Traction Control

by

**Mohammadreza Mottaghi, B.Sc.**

A thesis submitted to the  
Faculty of Graduate and Postdoctoral Affairs  
in partial fulfillment of the requirements for the degree of

**Master of Applied Science in Mechanical Engineering**

Ottawa-Carleton Institute for Mechanical and Aerospace Engineering  
Department of Mechanical and Aerospace Engineering  
Carleton University  
Ottawa, Ontario  
November, 2021

©Copyright

Mohammadreza Mottaghi, 2021

The undersigned hereby recommends to the  
Faculty of Graduate and Postdoctoral Affairs  
acceptance of the thesis

**Optimal Robust Output-tracking of Autonomous Rovers  
with Dynamic Traction Control**

submitted by **Mohammadreza Mottaghi, B.Sc.**

in partial fulfillment of the requirements for the degree of

**Master of Applied Science in Mechanical Engineering**

---

Professor D. Spinello, External Examiner

---

Professor J. Liu, Internal Examiner

---

Professor R. Chhabra, Thesis Supervisor

---

Professor R. Miller, Chair  
Department of Mechanical and Aerospace Engineering

Ottawa-Carleton Institute for Mechanical and Aerospace Engineering  
Department of Mechanical and Aerospace Engineering  
Carleton University  
November, 2021

# Abstract

This thesis develops a robust output-tracking control strategy for autonomous rover systems with redundant control directions. Taking advantage of their redundancy, an optimal distribution of control actions is proposed to enhance the dynamic traction of such systems. In the first phase, a robust optimal output-tracking control strategy for underactuated mechanical systems subject to mixed holonomic and nonholonomic constraints is presented. I perform a comprehensive control analysis of this large class of nonlinear systems in terms of local reachability, input-output linearizability, and local observability. Based on the input-output linearization of the holonomically restricted nominal system, I develop a sliding mode control strategy that is robust against projected effects of uncertainties and disturbances on the system's output. Asymptotic stability of the output towards a bounded desired trajectory is proved using Lyapunov's direct method while the system's internal stability (in the sense of boundedness) is investigated based on the notion of tracking-error zero dynamics. Time-dependent bounded matched uncertainties in the inertia parameters and disturbance forces arising in the unrestricted system are considered in this study. I propose an optimal sliding manifold according to the finite-horizon linear-quadratic regulator design problem with split boundary value condition.

In the second phase, I develop a novel methodology to optimally lift the proposed robust control law from the output dynamics to the space of control actions. This methodology aims at enhancing the dynamic traction of autonomous rovers through minimizing the quadratic norm of tractive ratios, without affecting the tracking performance of the system. The novelty is in redefining the optimization problem to propose a practical real-time traction control in the control loop and to use minimum information about wheel-ground contact dynamics. Tractive forces are approximated based on the dynamical model of the system determined by Lagrange d'Alembert principle, under the ideal nonholonomic assumptions. Normal reaction forces are estimated using Newton-Euler equations, under the quasi-static assumption on the

motion perpendicular to the plane of rover. To improve such estimates, a disturbance observer is designed by including the undisturbed auxiliary system in the control loop and its convergence is proved.

The developed control strategy is implemented on a six-wheel autonomous Lunar rover in a simulation environment and its performance is compared with that of an optimal proportional-integral-derivative feedback, feedforward controller along with the conventional right pseudo-inverse distribution of the control actions. The proposed controller shows superior performance both in terms of traction and tracking capabilities. The developed traction control algorithm is also implemented in a software-in-the-loop simulation environment using Vortex Studio, which is a high-fidelity multi-body dynamics engine. This digital twin of the system includes a 3-dimensional model on arbitrary terrains, with different tire and wheel-ground interaction models. The software-in-the-loop simulation shows high degree of acceptance between the estimated and real tractive and normal forces. It also confirms a considerable improvement achieved in the dynamic traction of the system.

To international students who lost their lives in PS752 flight

# Acknowledgments

I would like to acknowledge my amazing supervisor Dr.Chhabra for all his help during this journey. Your guidance has been so important in shaping my engineering vision and problem solving abilities. I would also like to show gratitude to my fantastic co-supervisor Dr.Huang. I will never forget all your assistance, support and kindness. Furthermore, I want to thank Eric Karpman for his help in working with Vortex Studio software. Finally, I wish to acknowledge the support and great love of my family.

# Contents

<b>Abstract</b>	<b>iii</b>
<b>Acknowledgments</b>	<b>vi</b>
<b>Table of Contents</b>	<b>vii</b>
<b>List of Tables</b>	<b>ix</b>
<b>List of Figures</b>	<b>x</b>
<b>1 Introduction</b>	<b>1</b>
1.1 Motivations . . . . .	1
1.2 Problem Statement . . . . .	2
1.3 Statement of Contributions . . . . .	2
1.4 Thesis Overview . . . . .	4
<b>2 Literature Review</b>	<b>6</b>
2.1 Constrained Mechanical Control Systems . . . . .	6
2.2 Nonlinear Robust Control . . . . .	8
2.3 Control of Autonomous Rovers . . . . .	11
2.4 Traction Control . . . . .	12
<b>3 Constrained Mechanical Systems</b>	<b>15</b>
3.1 Overview . . . . .	15
3.2 Constrained Mechanical Systems . . . . .	15
3.3 Control Analysis . . . . .	18
3.3.1 Reachability and Full-state Feedback Linearizability . . . . .	19
3.3.2 Input-output Linearization and Output-tracking . . . . .	21

3.4	Implementation on a Six-wheel Type (1, 1) Autonomous Lunar Rover	25
3.5	Summary . . . . .	36
<b>4</b>	<b>Robust Optimal Output Tracking</b>	<b>38</b>
4.1	Overview . . . . .	38
4.2	Uncertain Model . . . . .	38
4.3	Optimal Sliding Manifold Design . . . . .	41
4.4	Switching Control Law . . . . .	43
4.5	Implementation on a Six-wheel Lunar Rover . . . . .	47
4.5.1	Simulation Results . . . . .	49
4.6	Summary . . . . .	52
<b>5</b>	<b>Traction Optimization</b>	<b>56</b>
5.1	Overview . . . . .	56
5.2	Optimal Control Distribution . . . . .	56
5.3	Dynamic Traction Control . . . . .	59
5.3.1	Moving on a Straight Line . . . . .	64
5.3.2	Moving on a Curve . . . . .	67
5.4	Implementation on a Six-wheel Lunar Rover . . . . .	73
5.5	Validation of Estimated Values . . . . .	81
5.6	Simulation Results . . . . .	88
5.7	Experimentation . . . . .	96
5.8	Summary . . . . .	102
<b>6</b>	<b>Robust Dynamic Traction Control</b>	<b>103</b>
6.1	Overview . . . . .	103
6.2	Robust Output-tracking Traction Control . . . . .	103
6.3	Implementation on a Six-wheel Lunar Rover . . . . .	107
6.4	Summary . . . . .	109
<b>7</b>	<b>Conclusions and Future Directions</b>	<b>114</b>
	<b>List of References</b>	<b>117</b>
	<b>Appendix A Matrices <math>\hat{M}</math> and <math>\hat{C}</math></b>	<b>125</b>
	<b>Appendix B Matrices <math>A_l</math> and <math>B_l</math></b>	<b>126</b>

# List of Tables

4.1	Kinematic and dynamic parameters of the Lunar rover, uncertain parameters defined in the simulation, and control parameters . . . . .	50
5.1	Kinematic and dynamic parameters of the Lunar rover, suspension spring constants, and controller gains . . . . .	83
5.2	Kinematic and dynamic parameters of the Lunar rover, suspension spring constants, and controller and traction optimization parameters	89
5.3	Kinematic and dynamic parameters of the Lunar rover, suspension spring constants and design parameters defined in the simulation, in case study 2 . . . . .	100

# List of Figures

2.1	Examples of nonholonomic systems [1].(a) rolling disk (b) knife edge (c) Chaplygin sleigh . . . . .	7
3.1	Schematic of the system . . . . .	26
3.2	The unstable behaviour of the system during backward motion . . . . .	35
4.1	Optimal output-tracking sliding mode control block diagram . . . . .	47
4.2	Desired trajectory for the rover: (a) desired path (b) desired forward velocity of the rover (c) desired steering angles of port (black line) and starboard (blue line) front wheels . . . . .	49
4.3	Performance comparison of OPID and ORS in terms of error in (a) $x_b$ , (b) $y_b$ , (c) $y_1$ , (d) $y_2$ , (e) $\delta_p$ , and (f) $\delta_s$ . . . . .	53
4.4	Comparison of control commands generated by OPID (left) and ORS (right) laws. From the top to the bottom row, the plots respectively correspond to torques at the front wheels, center wheels, rear wheels, and steering degrees of freedom. . . . .	54
5.1	Control block diagram with optimal control distribution . . . . .	59
5.2	Flowchart of the proposed traction optimization algorithm in linear motion . . . . .	68
5.3	Flow chart of the proposed traction optimization algorithm in turning . . . . .	74
5.4	Free body diagram of the system under study in the roll, pitch, and vertical directions . . . . .	76
5.5	The designed mechanism in Vortex . . . . .	82
5.6	Desired Trajectory. (a) Desired Velocity (b) Desired Steering Angle (c) desired path . . . . .	84
5.7	Comparison of the estimated normal reaction forces and the actual values. Plots on the left correspond to the wheels at port side and plots on the right correspond to the wheels on starboard side. Sequentially, rows correspond to the front, center, and rear wheels. . . . .	85

5.8	Comparison of the estimated longitudinal tractive forces and the actual values. Plots on the left correspond to the wheels at port side and plots on the right correspond to the wheels on starboard side. Sequentially, rows correspond to the front, center, and rear wheels. . . . .	86
5.9	Comparison of the estimated Lateral tractive forces and the actual values using default tire deformation. The plot on left corresponds to the front wheels and the plot on right corresponds to the center wheels.	87
5.10	Comparison of the estimated Lateral tractive forces and the actual values after decreasing tire deformation. The plot on left corresponds to the front wheels and the plot on right corresponds to the center wheels. . . . .	88
5.11	Comparison of the generated normal reaction forces and tractive forces in longitudinal direction in both front wheels and port center wheel. Normal reaction forces are depicted in left and longitudinal tractive forces are depicted in right. Sequentially, the rows illustrate the comparison for port front, starboard front, and port center wheels. . . .	91
5.12	Comparison of the generated normal reaction forces and tractive forces in longitudinal direction in both rear wheels and starboard center wheel. Normal reaction forces are depicted in left and longitudinal tractive forces are depicted in right. Sequentially, the rows illustrate the comparison for starboard center, port rear, and starboard rear wheels.	92
5.13	Comparison of the generated normal reaction forces and tractive forces in lateral direction in both front wheels and center wheels. Corresponded Normal reaction forces are depicted in left and lateral tractive forces are depicted in right. Sequentially, the rows illustrate the comparison for front and center wheels. . . . .	93
5.14	The root mean square of the tractive ratios in all wheels. (a) in the longitudinal direction and (b) in the lateral direction . . . . .	95
5.15	Control throttle/brake torques in Pinv . . . . .	96
5.16	Comparison of steering torque in Pinv and Optimal . . . . .	96
5.17	Control throttle/brake torques in Optimal: (a) front wheels, (b) center wheels, (c) rear wheels . . . . .	97
5.18	Tractive ratios at all wheels for case study 1: (a) longitudinal direction, (b) lateral direction . . . . .	98

5.19	Comparison of the error seen by the controller in both Pinv and Optimal: (a) in x direction, (b) in y direction . . . . .	99
5.20	Comparison between the generated path by Pinv, Optimal, and the desired path . . . . .	99
5.21	Desired trajectory in case study 2: (a) desired velocity, (b) desired steering . . . . .	101
5.22	Tractive ratios at all wheels for case study 2: (a) longitudinal direction, (b) lateral direction . . . . .	101
5.23	Comparison between the generated path by Pinv, Optimal, and the desired path in case study 2 . . . . .	102
6.1	Block Diagram of the proposed observer . . . . .	106
6.2	Comparison of the actual and estimated lateral disturbance force at rear wheels . . . . .	108
6.3	Comparison of the distribution of lateral tractive forces in Optimal with (left) and without (right) disturbance observer . . . . .	108
6.4	Comparison of the generated normal reaction forces and tractive forces in longitudinal direction in both front wheels and port center wheel applying robust traction controller. Normal reaction forces are depicted in left and longitudinal tractive forces are depicted in right. Sequentially, the rows illustrate the comparison for port front, starboard front, and port center wheels. . . . .	110
6.5	Comparison of the generated normal reaction forces and tractive forces in longitudinal direction in both rear wheels and starboard center wheel applying robust traction controller. Normal reaction forces are depicted in left and longitudinal tractive forces are depicted in right. Sequentially, the rows illustrate the comparison for starboard center, port rear, and starboard rear wheels. . . . .	111
6.6	Comparison of the generated normal reaction forces and tractive forces in lateral direction in both front wheels and center wheels applying robust traction controller. Corresponded Normal reaction forces are depicted in left and lateral tractive forces are depicted in right. Sequentially, the rows illustrate the comparison for front and center wheels. . . . .	112
6.7	Control throttle/brake torques in Pinv robust control . . . . .	112
6.8	Comparison of steering torque in Pinv and Optimal Traction . . . . .	113

6.9 Control throttle/brake torques in optimal robust traction control: (a)  
front wheels, (b) center wheels, (c) rear wheels . . . . . 113

# Chapter 1

## Introduction

### 1.1 Motivations

Constrained robotic systems play a central role in many modern applications, such as space exploration, search and rescue, and aerial package delivery. Such systems inherent complex dynamics and due to their mission requirements they must operate autonomously with reliable control. For example, in the case of autonomous planetary exploration rovers, due to large interplanetary distances, real-time teleoperation is almost impossible, and they should operate semi-autonomously to perform the prescribed control tasks. Constrained robotic systems, based on their mission description, are stabilized towards a point, path, or trajectory. In many applications, stabilizing an output function towards a desired path with prescribed timing law (output-tracking) while other states of the system are well-behaved is of higher priority than trajectory-tracking of all states. This control task can be performed applying velocity (kinematic control) or force/torque (dynamic control) commands to the defined control directions. Dynamic control schemes are more preferable in applications of constrained robotic systems in which system has considerable interactions with its operating environment. The reason is that the dynamics of the system continuously is considered in the control loop and that prevents incoordination between control inputs. Since constrained robotic systems are subject to different sources of uncertainties, such as, uneven terrains, rocks, dust, unpredictable weather and harsh sun light, robustness is a crucial factor that should be considered in the design of their controller. Apart from robustness, one of the main concerns in the control of autonomous rovers/vehicles, is keeping the system away from conditions resulting in the violation of the zero-velocity constraints at wheel-ground contact points. If such

violations happen, the system may lose mobility, become trapped, exhibit noticeable tracking error, and more importantly lose wheel odometry as a powerful localization approach [2].

## 1.2 Problem Statement

A class of mechanical control systems containing redundant control directions and subject to mixed holonomic and nonholonomic constraints in Pfaffian form is considered. The control design for such systems is particularly difficult due to their underactuation and existence of nonholonomic constraints. This thesis addresses the following two main control problems:

- (1) Given a desired feasible trajectory for the output of the system find a control law that asymptotically stabilizes the output error while (i) minimizing a norm of control actions and output errors, (ii) keeping internal states of the system well-behaved, and (iii) being robust against bounded sources of matched uncertainties.
- (2) Taking advantage of the redundant control directions, find an optimal distribution of control actions enhancing the dynamic traction of the system. In this thesis, the term “dynamic traction” refers to maintaining close-to-zero-velocity constraints at wheel-ground contact points, i.e., ensuring that the nonholonomic constraints are satisfied during dynamic tasks.

## 1.3 Statement of Contributions

The main contributions of this thesis can be summarized in the following.

- (1) In the first phase, a comprehensive control analysis is performed for a class of mechanical control systems subject to mixed holonomic and nonholonomic velocity constraints in Pfaffian form. Under the assumption that system is input-output linearizable, I propose an observability decomposition of the internal states. This decomposition enhances the stability analysis of the internal dynamics existing in the literature. In addition, I develop a robust output-tracking Sliding Mode Control (SMC) strategy that is applicable to a wide

range of constrained mechanical systems experiencing complex bounded time-dependent matched uncertainties in their inertia parameters. The proposed SMC contains an optimally designed sliding manifold at the output level that minimizes a functional based on a norm square of the output error and that of the control actions. This phase of the research is submitted for publication to the IEEE Transactions on Control Systems Technology.

- M. R. Mottaghi and R. Chhabra, “Robust optimal output-tracking control of constrained mechanical systems with application to autonomous rovers,” *IEEE Transactions on Control Systems Technology*, Under Review (Submitted June 2021).

- (2) In the second phase, employing redundant control directions, an optimal distribution of control actions is proposed to enhance the force/moment interaction of the system without affecting its tracking performance. The developed optimization is applied to dynamic traction control of autonomous rovers. I introduce a cost function resulting in linear necessary conditions of optimality and it considers the direction of tractive forces. In contrast to the optimal traction controllers proposed in the literature, the developed methodology is needless of numerical optimizations impeding real-time implementation in dynamic tasks, and it is applicable to various types of trajectories. In this approach, under the assumption of ideal nonholonomic constraints, the magnitude of tractive forces are computed based on the dynamic model of the system determined based on the Lagrange-D’Alembert principle. Accordingly, the dependency on the terrain parameters is significantly reduced and only the knowledge of static friction coefficients is necessary. This phase of the research is submitted for publication to the IEEE Transactions on Systems, Man, and Cybernetics: Systems.

- M. R. Mottaghi and R. Chhabra, “Fast Optimal Traction Control of Dynamic Autonomous Rovers on Prescribed Trajectories with Wheel-Fighting Consideration,” *IEEE Transactions on Systems, Man, and Cybernetics: Systems*, Under Review (Submitted November 2021).

- (3) In the last phase of this research, phases 1 and 2 are combined and a robust output-tracking controller with optimal distribution of control actions for the traction improvement is proposed. Firstly, I show that, the design of output-tracking control law and optimal distribution of control actions are independent,

and each can be performed using different models of the system. Secondly, an observer is designed to capture the lumped effect of uncertainties on the output of the system. The observed values are then exploited to improve the estimations of normal forces and tractive forces. I expand an observer proposed in [3] for single-input-single-output nonlinear systems to input-output feedback linearizable multi-input-multi-output systems. This observer is designed in time domain and it is needless of consideration of low-pass filters associated with the observers designed in frequency domain. The results of this phase will be submitted for publication to *Mechanical Systems and Signal Processing* and *Automatica*.

- M. R. Mottaghi and R. Chhabra, “Optimal Robust output-tracking of autonomous rovers with dynamic traction control,” *Mechanical Systems and Signal Processing*, To be submitted in January 2022.
- M. R. Mottaghi and R. Chhabra, “Disturbance observer design for MIMO input-output linearizable nonholonomic mechanical systems,” *Automatica*, To be submitted in March 2022.

## 1.4 Thesis Overview

Chapter 2 presents a brief background and state-of-the-art in description of constrained mechanical systems, nonlinear robust controller design and its application to autonomous rover systems. The concept of traction is defined and recent developments in traction controller design for autonomous rover/vehicle systems is discussed.

In Chapter 3, the reduced projected state space representation of a class of mechanical systems subject to mixed holonomic and nonholonomic constraints is obtained. Such systems are analysed in terms of different control aspects. The developed theory is then implemented on a six-wheel type (1, 1) autonomous Lunar rover.

In Chapter 4, the uncertain state space representation of the system is obtained and a robust control law is derived based on sliding mode control strategy. The proposed control law is then implemented on a six-wheel autonomous Lunar rover and the efficacy of that is shown through simulation results.

In Chapter 5, the concept of optimal distribution of control actions is introduced, and applied to traction improvement of autonomous rover/vehicle systems. The theory is implemented on an autonomous rover and the efficacy of the proposed traction

controller is investigated through a developed software-in-the-loop simulation environment.

Finally, the first and second phases of this research are combined in Chapter 6 and a robust output-tracking traction controller is proposed. To improve the estimations exploited in the traction control algorithm, an observer is designed to capture the effect of disturbances on such estimations. The efficacy of this control strategy is shown through the simulations.

Chapter 7 includes some concluding remarks and possible future directions of this thesis.

## Chapter 2

# Literature Review

### 2.1 Constrained Mechanical Control Systems

In most modern robotic applications, the evolution of a robot in the tangent bundle of its configuration manifold is restricted by constraints. Depending on the integrability condition, such constraints are categorized into holonomic and nonholonomic. The term holonomic refers to the category of constraints that are integrable on the configuration manifold of the system and limit the space of all possible configurations. Length and rigidity constraints are some examples of holonomic constraints. On the other hand, nonholonomic constraints are not integrable and they only restrict the evolution of the system in its configuration manifold. Rolling and sliding without slipping are some examples of nonholonomic constraints. Nonholonomic constraints also come in two types, namely, dynamic and kinematic. The former refers to the constraints preserved by dynamics of the system and they are not externally imposed, such as conservation of momentum in space robots. The latter describes the constraints externally imposed by the kinematics of the system, such as rolling constraints in wheeled mobile robots [1]. Presence of constraints in mechanical systems, introduces modelling and control challenges, e.g., loss of full-state controllability in holonomic systems, underactuation and loss of full-state feedback linearizability property in nonholonomic systems [4].

Several comprehensive frameworks have been presented to capture the behaviour of mechanical systems with constraints, specially in Pfaffian form [5–7]. In [8], a unified dynamical model of robotic systems subject to nonlinear constraints is outlined that is based on differential variational principles. Yun and Sarkar unify the

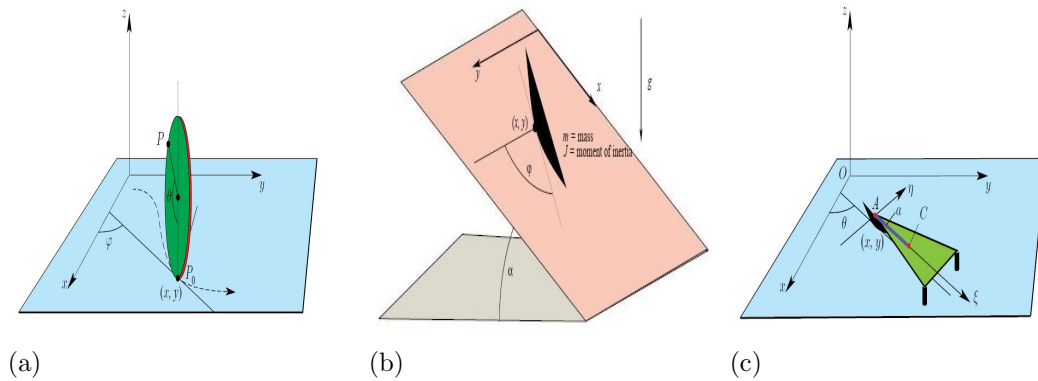


Figure 2.1: Examples of nonholonomic systems [1]. (a) rolling disk (b) knife edge (c) Chaplygin sleigh

state space representation of systems subject to mixed holonomic and nonholonomic constraints via substituting algebraic holonomic equations by stable first-order differential equations to improve the stability of numerical simulations [9]. A historical review of nonholonomic mechanics including the derivation of Lagrangian and Hamiltonian equations of motion along with recent developments, e.g., application of Hamilton-Jacobi theory in nonholonomic systems, is presented in [10]. In a book by Neimark et.al, the dynamic behavior of nonholonomic systems is studied from different perspectives including the Caplygin’s problem, the canonical form of the governing equations, and variational principles in nonholonomic systems [11]. Using the Generalized Program Motion Equation (GPME) method, a unified dynamical modeling framework is proposed for systems subject to nonholonomic constraints of any arbitrary order [12]. A geometric formalism for the Lagrangian systems subject to nonlinear nonholonomic constraints is also proposed in [13] using the concept of product structure on the tangent bundle of the configuration manifold and the space of all admissible velocities.

Control challenges associated with nonholonomic systems, such as motion planning and feedback stabilization, are well-documented in the literature [14, 15]. A geometric exposition on nonholonomic control is presented in a book by Bloch that includes studying symmetry properties, optimal control and energy-based methods of stabilization of nonholonomic systems [1]. Trajectory stabilization of nonholonomic systems has been also addressed using, e.g., a linearized model of system around a trajectory [16] or the integrator backstepping technique [17]. Further, output-tracking control laws for mechanical systems with nonholonomic rolling constraints have been

developed based on input-output linearization techniques [18]. Chhabra *et al.* propose an output-tracking control strategy for symmetric nonholonomic Hamiltonian systems [19], founded upon their dynamical reduction [20] and input-output linearization in their reduced state space, applying static state feedback. This technique is implemented to design a torque-based controller for the Lunar Exploration Light Rover [21].

## 2.2 Nonlinear Robust Control

Robust control refers to the problem of designing a control scheme with high accuracy for an uncertain plant [22]. A comparison of classical and modern robust control approaches and uncertainty modelling is documented in [23]. Depending on satisfaction of the so-called matching condition, uncertainties can be categorized into matched and mismatched. Matched uncertainties are appearing in the control input channel, such as disturbance forces and uncertainties in the inertia parameters in dynamic control. On the other hand, mismatched uncertainties are not appearing in input channels, e.g., uncertainties in the kinematic parameters of the system in dynamic control [24].

Robust control of nonlinear systems subject to matched uncertainties can be performed by considering uncertainties as bounded perturbations to the nominal plant and designing a controller with respect to such bounds. Some examples of such techniques including integral control, Sliding Mode Control (SMC), back-stepping and gain scheduling are discussed in a book by Khalil [24]. In addition, a general framework is introduced to extend the theory of Lyapunov design to uncertain plants by proposing a Robust Control Lyapunov Function (RCLF) [25]. A robust output tracking control is proposed in [26], using output feedback and applying a sliding mode controller to the input-output dynamics. The proposed control law contains a time-dependant exponent parameter law to ensure both accuracy and low energy consumption. On the other hand, when a system is subject to bounded mismatched uncertainties, robustness of the controller can be ensured for example, by applying high gains feedback technique [24], or by modelling the uncertainties' structure and designing a model predictive sliding mode controller [27]. Additionally, a robust control scheme for systems subject to mismatched disturbances is proposed in [28] by describing the bound of uncertainties via a fuzzy set. In this paper, the controller

gains are optimally designed to minimize the fuzzy performance index corresponding to the fuzzy behaviour and the control effort.

Nonlinear robust controllers can also be designed applying exogenous disturbance observers [29] and adaptive control laws. In such approaches, first, uncertainties are parameterized as some unknown parameters. Then, employing observers, the controller tries to learn them and produce an appropriate reaction [24,30,31]. In addition, the observed values can be used to enhance the performance of the designed nonlinear control law for example by adjusting the controller gains based on the estimated disturbances [32,33]. Robustness can also be guaranteed by observing the lumped effect of the disturbances and compensating that applying a proper feed-forward control command (composite controllers) [34,35]. Most proposed adaptation laws are designed in frequency domain and that leads to the generation of high-frequency noises at the observer's output channel. To resolve this issue, low pass filters are considered but that results in the elimination of high-frequency disturbance effects [36]. However, a disturbance observer is proposed for Single Input Single Output (SISO) nonlinear systems in the time domain employing an auxiliary system defined based on unperturbed plant and using the output feedback [3]. In observer-based robust controllers, in contrast to other approaches, the worst-case uncertainties are not considered in the controller (controller does not overestimate them) and consequently, the controller does not contain large control gains [37]. However, there is no fast and accurate estimation of the disturbances.

Sliding mode control, as a robust variable structure control strategy, has been employed in many control applications, due to its simple structure, guaranteed asymptotic stability, and introduction of a reduced-order error dynamics [38]. The main idea in SMC is (i) to design a sliding manifold on which the error is asymptotically stabilized towards the origin and determine an appropriate control law keeping the system on this manifold and (ii) to obtain a switching control law pushing the system towards that manifold whenever it is out of it [24]. Applying this approach, the stabilizing control law can be obtained based on the reduced-order dynamics of the system on the sliding manifold. The main two challenges associated with SMC are defining the sliding manifold and the discontinuity of the switching control law known as the chattering effect. It is also noteworthy that as the result of an initial error the switching control law produces a high-magnitude chattering, since its gains are in the direct proportion of the upper bound of the uncertainties. Accordingly, the sliding

manifold must contain the initial condition of the system.

To improve the performance of SMC, a chattering-free SMC is derived based on a time varying feedback gain, whose global stability is proven using the Lyapunov second theorem and invariance principle [39]. The method of boundary layer is also proposed, in which the discontinuous switching function is replaced by a saturation function and the error converges to a boundary layer around the origin. The thickness of such a boundary layer can be designed by adjusting the defined saturation points [40, 41]. In addition, to alleviate the chattering phenomenon, higher-order sliding mode controllers are proposed, in which the stability towards the sliding surface is investigated based on higher-order derivatives of the conventional sliding surface. This way, the discontinuity appears in the higher-order derivatives of the control input to the system and that results in the smoothness of actual control inputs. However, in such approaches particularly during dynamic control, higher order derivatives of the system states are required which can not be directly measured in practice and estimation of them results in noisy signals [42, 43]. Integral Sliding Mode Control (ISMC) is also proposed to eliminate the reaching phase and ensure the invariance of the sliding manifold for the entire system response [44].

Regarding the applications of SMC in control of constrained mechanical systems, Ge *et al.* propose a robust adaptive state/output feedback point stabilization of a class of nonholonomic systems in chained form along with an adaptive switching law guaranteeing the boundedness of the states [45]. A robust control scheme has also been developed for stabilization of nonholonomic systems with drift uncertainties, using time-varying SMC [46]. A general order sliding mode control algorithm along with determination of the sliding parameters to satisfy both input and states inequality constraints is developed in [47]. In [48], the second order sliding mode controller is proposed containing a saturation function of states maximizing the domain of attraction for nonlinear systems subject to state inequality constraints. By transforming the state space representation of the nonholonomic systems into a chained form and separating the uncertain dynamics, an adaptive ISMC is proposed in [49]. This strategy contains a control command for stabilization of the nominal plant and a compensator for observed disturbances.

## 2.3 Control of Autonomous Rovers

A category of mechanical systems that are subject to both holonomic and nonholonomic constraints is autonomous planetary exploration rovers that often experience several forms of uncertainties and disturbances. The nonholonomic constraints in such systems mostly correspond to the no velocity conditions at wheel-ground contact points. The holonomic constraints in rover systems are coming from some geometric restrictions to ensure the mobility of the system such as well known Ackerman condition. It is also noteworthy that the imposed nonholonomic constraints may also result in the restriction of the configuration manifold of the system by introducing some non-trivial holonomic constraints. Due to their mission requirements and the imposed constraints, such systems contain complex dynamics, which needs to be considered during robust control design, particularly for determination of uncertainty bounds. Sojourner, Lunar Exploration Light Rover, twin Mars Exploration Rovers, and Perseverance are some examples of such systems [50]. Different categories of autonomous rovers based on their mobility is introduced in [51].

The first step in designing a controller is obtaining a proper model of the system. In the case of autonomous rovers, the kinematic model of the system can be obtained based on the the imposed nonholonomic constraints and forming the space of the admissible velocities. This model is used in designing kinematic control and applying velocity commands in different control directions. However, the dynamical model of the system is also required to perform dynamic control. Dynamical model of autonomous rovers can be determined based on both the Newton-Euler equations or Euler-Lagrange formalism. In the Newton-Euler method, regardless of the imposed constraints (constrained free model) all external forces applied to the system are specified and considered as control directions. Then, using terramechanics relationships, such forces are converted to the actual control directions of the system which mostly are in the form of throttle/brake or steering torques. Such models are greatly dependant on different parameters describing wheel-soil interactions and the direction of all non-trivial external forces has to be completely specified. However, using the Euler-Lagrange method, the torques applied to the wheel-body joints are considered as control directions and the external wheel-ground contact forces associated with to the nonholonomic constraints are appearing as Lagrange multipliers in the governing equations of motions.

The evolution of control systems developed for nonholonomic rovers initiated

in 1990s. The full posture kinematic tracking control of Differential Drive Rovers (DDRs), based on Lyapunov design, is proposed in [52]. This result was extended to include robustness by designing a SMC in polar coordinates for DDRs experiencing unknown disturbing forces [53]. Ashrafiuon *et al.* develop a SMC for uncertain simple planar vehicles with only two control inputs that is robust against bounded time-dependant matched uncertainties. This method is based on a reduced order error dynamics obtained using the concept of transitional trajectory [54].

State feedback linearization of different types of rover systems has been also investigated, applying static or dynamic state feedback [55]. Wang and Xu propose a set of output functions for which rover systems are input-output linearizable applying static state feedback [56]. Their proposed output functions are path independent and in the form of a position of a virtual reference point. The location of such points is determined according to the type of the rover, e.g. in front of a center of rotation of the system in type (2,0) and in front of a steerable wheel in type (1,1) autonomous rovers. The stability of the internal dynamics of such systems is also investigated based on the concept of tracking-error zero dynamic and Lyapunov indirect method for a four-wheel autonomous rover in [56] and Lyapunov direct method for differential drive rover (DDR) in [57]. It is proved that the internal dynamics of autonomous rovers is asymptotically stable while the system is moving in forward direction and it is unstable when it moves in the backward direction. High gain observers are also proposed based on the kinematic model of system to overcome the problem of lack of measurements of the Cartesian velocities in dynamic feedback output tracking control of such systems [58]. A robust trajectory tracking control satisfying input constraints for autonomous rovers is also developed in [59]. In this paper, authors employ a smooth feedback law, whose time varying parameters are obtained through a geometric-based design strategy.

## 2.4 Traction Control

Traction is one of the main concerns in the control of autonomous rovers/vehicles. Deprived traction results in losing mobility and stability of control system, deteriorating tracking performance, and erroneous wheel odometry for localization [2]. Traction is particularly crucial when a rover undergoes dynamic motions on rough terrains.

In this thesis, the term *dynamic traction* is used to refer to maintaining close-to-zero-velocity condition at wheel-ground contact points during tracking a dynamic prescribed trajectory, i.e., respecting normally-imposed nonholonomic constraints. Accordingly, *dynamic traction control* means producing control inputs considering the dynamic traction on rough terrains. A dynamic traction controller must be real-time and have no influence on the tracking performance of the system.

The evolution of traction control systems for wheeled vehicles initiated in 1980s when different supervisory control strategies including anti-lock braking systems and anti-spin acceleration systems were proposed for commercialized vehicles [60]. Such supervisory control systems are enhanced by introducing a mathematical model of the vehicle and braking systems based on dynamics of the wheels, and accordingly employing a robust discrete-time nonlinear feedback control law [61]. Fuzzy logic-based [62, 63] and neural network-based [64] control strategies with the aim of controlling wheel slip in anti-lock braking systems have also been developed.

For autonomous systems, traction control strategies have been developed based on wheel slippage estimation, using, e.g., tire deformation models [65], inertia measurement unit [66–68], and visual odometry [69–71]. Such estimations not only can improve localization, but they also can be used in designing traction controllers [72–76]. Traction control algorithms working based on slippage estimation are divided into two categories: velocity-based and torque-based. In the former category, the estimated amount of slippage is compensated with appropriate speed commands [77]. Since the system’s dynamics is not continuously considered in the computation of control commands, such approaches lead to incoordination between wheels (wheel fighting) [78]. In the latter category, slippage is included in the dynamics of the system and it is compensated by applying appropriate control torque commands. For example in [79, 80], the average slip ratio is defined as a control target and it is maintained in an optimal region using sliding mode control. Slippage dynamics can be also approximated [81] and controlled applying an input-output linearizing feedback [82].

Due to the lack of accurate model for wheel slippage [83, 84], several traction control algorithms with minimal dependency on slip estimation have been introduced. Iagnemma *et al.* propose a traction controller under the quasi-static assumption for planetary rovers. They employ redundant control actions to offer an optimal force distribution minimizing the ratio of tractive to normal reaction forces, known as

“tractive ratios” [85]. This method is improved by introducing an enhanced quasi-static model independent of complex tire-soil interaction models for a rover named “SOLERO” [86]. For systems operating with high velocities, Sarkar *et al.* propose a torque-based traction control exploiting the redundancy in a mobile robot with two driven wheels and two active steering systems. They asymmetrically distribute the control torques when one wheel runs into a less desirable terrain condition. Their method is based on a primitive model of the system and relies on the wheels’ slip curves only in the longitudinal direction [87]. Another dynamic traction control strategy for redundant autonomous rovers is proposed in [88], where a rigid body dynamical model of the system and a terramechanics model are combined to introduce an optimal control distribution to maximize traction. This approach is enhanced by redefining the optimization criterion to consider the quadratic norm of tractive ratios [89].

In the mentioned studies, complex terramechanics models [90] or accelerometers at wheels [91] are often necessary to compute control torques based on the knowledge of optimal tractive forces obtained using constraint-free dynamical models. However, the real-time estimation of terramechanic parameters is computationally demanding and not accurate, and accelerometer signals are known to be noisy. Further, the developed traction controllers are normally either based on simplistic vehicle models, or rely on numerical solutions of nonlinear optimizations, impeding their real-time implementation during dynamic tasks. To the best of the authors’ knowledge, wheel-fighting phenomenon is also an understudied subject in the current optimal dynamic traction control strategies. Wheel-fighting results in deterioration of traction and increase of the power consumption in the system.

## Chapter 3

# Input-output Linearization of Constrained Mechanical Systems

### 3.1 Overview

In this chapter, kinematics and dynamics of mechanical systems subject to mixed holonomic and nonholonomic velocity constraints in Pfaffian form are investigated. The identified holonomic constraints are formally integrated and implemented in the governing equations of motion, and the space of admissible velocities is obtained based on the nonholonomic constraints. Accordingly, a reduced state-space representation of such systems is proposed and used in the analysis of constrained systems in terms of different control perspectives, including local reachability, full-state feedback linearizability, and input-output linearizability. Under some explained assumptions, input-output linearization is performed and the states of the system are decomposed into external and internal states. I also propose an observability decomposition for the internal states that is crucial to the stability analysis of the internal dynamics. Finally, the performed control analysis is discussed for a six-wheel type (1,1) autonomous Lunar rover used as the case study in this thesis.

### 3.2 Constrained Mechanical Systems

In this section, I describe a class of mechanical control systems with mixed holonomic and nonholonomic constraints. I consider the evolution of such systems in the tangent bundle of their  $\hat{n}$ -dimensional smooth configuration manifold, denoted by  $\hat{Q}$ . A set of  $\mathfrak{r}$  everywhere linearly independent constraints on velocities in Pfaffian form is

considered:

$$\hat{A}(\hat{\mathbf{q}})\dot{\hat{\mathbf{q}}} = 0 \quad (3.1)$$

where  $(\hat{\mathbf{q}}, \dot{\hat{\mathbf{q}}}) \in T\hat{Q}$ , the tangent bundle of the configuration manifold, and  $\hat{A} : \hat{Q} \rightarrow \mathbb{R}^{\mathfrak{r} \times \hat{\mathfrak{n}}}$  is the constraint matrix. All admissible velocities of the system must lie in the  $(\hat{\mathfrak{n}} - \mathfrak{r})$ -dimensional annihilator distribution  $\mathcal{D}$  resulted from the constraint equations. Let  $\hat{N} : \hat{Q} \rightarrow \mathbb{R}^{\hat{\mathfrak{n}} \times (\hat{\mathfrak{n}} - \mathfrak{r})}$  denote the matrix whose columns span  $\mathcal{D}$ , i.e.,  $\hat{N}(\hat{\mathbf{q}})\hat{A}(\hat{\mathbf{q}}) = 0$ .

Based on the Lagrange d'Alembert principle, dynamics of the constrained mechanical system is derived in matrix form:

$$\begin{aligned} \hat{M}(\hat{\mathbf{q}})\ddot{\hat{\mathbf{q}}} + \hat{C}(\hat{\mathbf{q}}, \dot{\hat{\mathbf{q}}})\dot{\hat{\mathbf{q}}} + \hat{\mathbf{g}}(\hat{\mathbf{q}}) &= \hat{B}(\hat{\mathbf{q}})\boldsymbol{\tau} + \hat{A}(\hat{\mathbf{q}})^T \hat{\boldsymbol{\lambda}}, \\ \hat{A}(\hat{\mathbf{q}})\dot{\hat{\mathbf{q}}} &= 0 \end{aligned} \quad (3.2)$$

where  $\hat{M} : \hat{Q} \rightarrow \mathbb{R}^{\hat{\mathfrak{n}} \times \hat{\mathfrak{n}}}$  is the symmetric positive definite mass matrix of the system,  $\hat{C} : T\hat{Q} \rightarrow \mathbb{R}^{\hat{\mathfrak{n}} \times \hat{\mathfrak{n}}}$  is the matrix of Coriolis and centrifugal forces,  $\hat{\mathbf{g}} : \hat{Q} \rightarrow \mathbb{R}^{\hat{\mathfrak{n}}}$  is the vector of potential forces,  $\boldsymbol{\tau} \in \mathbb{R}^{\mathfrak{s}}$  is the vector of control inputs,  $\hat{B} : \hat{Q} \rightarrow \mathbb{R}^{\hat{\mathfrak{n}} \times \mathfrak{s}}$  is the matrix whose columns are the control directions, and  $\hat{\boldsymbol{\lambda}} \in \mathbb{R}^{\mathfrak{r}}$  is the vector of Lagrange multipliers. Hereinafter, for brevity the dependency of the matrices and vectors is dropped wherever it does not raise confusion.

**Assumption 3.1.** The dimension of the vector  $\boldsymbol{\tau}$  is greater than the dimension of distribution  $\mathcal{D}$ , i.e.,  $\mathfrak{s} > \hat{\mathfrak{n}} - \mathfrak{r}$ , and no columns of  $\hat{B}$  are in the image of  $\hat{A}$ .

If the involutive closure of  $\mathcal{D}$ , denoted by  $\bar{\mathcal{D}}$ , is of system's dimension  $(\hat{\mathfrak{n}})$ , then all imposed constraints are nonholonomic (non-integrable). The involutive closure of  $\mathcal{D}$  is the minimal distribution that contains elements of  $\mathcal{D}$  and all iterative Lie-brackets of vector fields in  $\mathcal{D}$ . If the dimension of  $\bar{\mathcal{D}}$  is equal to  $\mathfrak{n} = \hat{\mathfrak{n}} - \mathfrak{p}$ , the system experiences  $\mathfrak{p}$  holonomic (integrable) constraints and  $\mathfrak{m} = \mathfrak{r} - \mathfrak{p}$  nonholonomic constraints.

After identifying the holonomic constraints, I introduce the restricted configuration manifold  $Q$ , with dimension  $\mathfrak{n}$ , which is an embedded sub-manifold of  $\hat{Q}$  with the inclusion map  $\iota_Q : Q \rightarrow \hat{Q}$ . Let  $(\mathbf{q}, \dot{\mathbf{q}}) \in TQ$  denote an element of the tangent bundle of  $Q$ , and let  $J(\mathbf{q})$  be the Jacobian of the inclusion map. The set of  $\mathfrak{m}$  remaining completely nonholonomic constraints on  $Q$  are defined by:

$$A(\mathbf{q})\dot{\mathbf{q}} = 0, \quad (3.3)$$

where

$$A(\mathbf{q}) = E\hat{A}(\iota_Q(\mathbf{q}))J(\mathbf{q}). \quad (3.4)$$

Due to inclusion of holonomic constraints, the rows of the matrix  $\hat{A}J$  are linearly dependant and they span a co-distribution of dimension  $\mathbf{m}$ . Here, the constant matrix  $E \in \mathbb{R}^{\mathbf{m} \times \mathbf{r}}$  introduces a minimal linear combination of the rows of  $\hat{A}J$  to parameterize the resultant co-distribution, which eliminates the redundant constraint directions.

Pre-multiplying both sides of (3.2) by  $J^T(\mathbf{q})$ , and substituting  $\dot{\hat{\mathbf{q}}}$  and  $\ddot{\hat{\mathbf{q}}}$ , based on the inclusion map, i.e.,

$$\begin{aligned} \dot{\hat{\mathbf{q}}} &= J(\mathbf{q})\dot{\mathbf{q}}, \\ \ddot{\hat{\mathbf{q}}} &= \dot{J}(\mathbf{q}, \dot{\mathbf{q}})\dot{\mathbf{q}} + J(\mathbf{q})\ddot{\mathbf{q}}, \\ \dot{J}(\mathbf{q}, \dot{\mathbf{q}}) &= \sum_{j=1}^n \frac{\partial J(\mathbf{q})}{\partial \mathbf{q}_j} \dot{\mathbf{q}}_j, \end{aligned} \quad (3.5)$$

the equations of motion in the restricted configuration manifold  $Q$  become:

$$\begin{aligned} \dot{\mathbf{q}} &= N(\mathbf{q})\boldsymbol{\eta}, \\ M(\mathbf{q})\ddot{\mathbf{q}} + C(\mathbf{q}, \dot{\mathbf{q}})\dot{\mathbf{q}} + \mathbf{g}(\mathbf{q}) &= B(\mathbf{q})\boldsymbol{\tau} + A(\mathbf{q})^T\boldsymbol{\lambda}. \end{aligned} \quad (3.6)$$

Here,  $\mathbf{q}_j$  denotes the  $j^{\text{th}}$  element of  $\mathbf{q}$ ,  $N : Q \rightarrow \mathbb{R}^{n \times n-m}$  is a matrix whose columns span the kernel of the constraint matrix  $A$ , and  $\boldsymbol{\eta} \in \mathbb{R}^{n-m}$  is the vector of quasi-velocities,  $M := J^T\hat{M}(\iota_Q(\mathbf{q}))J$  is the mass matrix,  $C := J^T(\hat{M}(\iota_Q(\mathbf{q}))\dot{J} + \hat{C}(\iota_Q(\mathbf{q}), J\dot{\mathbf{q}})J)$  is the matrix of Coriolis and centrifugal forces,  $\mathbf{g} := J^T\hat{\mathbf{g}}(\iota_Q(\mathbf{q}))$  is the vector of potential forces,  $B := J^T\hat{B}(\iota_Q(\mathbf{q}))$  is the matrix of control directions, and  $\boldsymbol{\lambda} := E\hat{\boldsymbol{\lambda}} \in \mathbb{R}^{\mathbf{m}}$  is the vector of Lagrange multipliers.

Pre-multiplying both sides of the set of equations representing the dynamics of the system in (3.6) by  $N^T$ , and substituting

$$\begin{aligned} \ddot{\mathbf{q}} &= \dot{N}(\mathbf{q}, \dot{\mathbf{q}})\boldsymbol{\eta} + N(\mathbf{q})\dot{\boldsymbol{\eta}}, \\ \dot{N}(\mathbf{q}, \dot{\mathbf{q}}) &= \sum_{j=1}^n \frac{\partial N(\mathbf{q})}{\partial \mathbf{q}_j} \dot{\mathbf{q}}_j, \end{aligned} \quad (3.7)$$

the set of equations on the state space of the system  $\mathcal{X} \subset TQ$ , which is the distribution

spanned by the columns of  $N$ , is obtained as:

$$\begin{aligned} \dot{\mathbf{q}} &= N(\mathbf{q})\boldsymbol{\eta}, \\ M_r(\mathbf{q})\dot{\boldsymbol{\eta}} + C_r(\mathbf{q}, \boldsymbol{\eta})\boldsymbol{\eta} + \mathbf{g}_r(\mathbf{q}) &= B_r(\mathbf{q})\boldsymbol{\tau}. \end{aligned} \quad (3.8)$$

Here, given  $N^T A^T = 0$ , the constraint forces are eliminated, and

$$\begin{aligned} M_r &:= N^T M N, \\ C_r &:= N^T (M \dot{N}(\mathbf{q}, N\boldsymbol{\eta}) + C(\mathbf{q}, N\boldsymbol{\eta})N), \\ B_r &:= N^T B, \\ \mathbf{g}_r &:= N^T \mathbf{g}, \end{aligned}$$

are respectively the reduced mass matrix, the reduced matrix of Coriolis and centrifugal forces, the reduced matrix of control directions, and the reduced vector of potential forces.

I denote a member of  $\mathcal{X}$  by  $\mathbf{x} = [\mathbf{q}^T, \boldsymbol{\eta}^T]^T$  that is a  $(2\mathbf{n} - \mathbf{m})$ -dimensional vector of system states. The state space representation of the governing equations of motion is

$$\dot{\mathbf{x}} = \mathbf{f}(\mathbf{x}) + G(\mathbf{x})\boldsymbol{\tau}, \quad (3.9)$$

where

$$\mathbf{f}(\mathbf{x}) = \begin{bmatrix} N\boldsymbol{\eta} \\ -M_r^{-1}(C_r\boldsymbol{\eta} + \mathbf{g}_r) \end{bmatrix}, \quad (3.10)$$

$$G(\mathbf{x}) = \begin{bmatrix} \mathbb{O}_{\mathbf{n} \times \mathbf{s}} \\ M_r^{-1}B_r \end{bmatrix}, \quad (3.11)$$

and  $\mathbb{O}$  denotes the matrix of zeros with proper dimensions.

### 3.3 Control Analysis

In this section, I analyze different control aspects of the system in (3.9). First, the full-state reachability of the system, as the necessary condition for controllability, is studied. Then, the full-state feedback linearizability of the system is investigated. Finally, the output-tracking control problem for the system in (3.9) is defined, and

input-output linearizability and the stability of the internal dynamics are discussed.

### 3.3.1 Reachability and Full-state Feedback Linearizability

Let us introduce the control input  $\boldsymbol{\mu} \in \mathbb{R}^{n-m}$ , based on

$$B_r \boldsymbol{\tau} = C_r \boldsymbol{\eta} + \mathbf{g}_r + M_r \boldsymbol{\mu}, \quad (3.12)$$

that partially linearizes the system in (3.9). Under this transformation, the resultant closed-loop system becomes

$$\begin{aligned} \dot{\mathbf{x}} &= \mathbf{f}^1(\mathbf{x}) + G^1 \boldsymbol{\mu}, \\ \mathbf{f}^1(\mathbf{x}) &= \begin{bmatrix} N\boldsymbol{\eta} \\ \mathbf{0} \end{bmatrix}, \quad G^1 = \begin{bmatrix} \mathbb{O}_{n \times (n-m)} \\ \mathbb{I}_{(n-m) \times (n-m)} \end{bmatrix}, \end{aligned} \quad (3.13)$$

where  $\mathbb{I}$  denotes the identity matrix with appropriate dimensions.

The control system in (3.13) is fully reachable if and only if for any arbitrary pair of an initial state  $\mathbf{x}_0$  and a terminal state  $\mathbf{x}_f$ , one can find a control input  $\boldsymbol{\mu}$  moving the system from  $\mathbf{x}_0$  to  $\mathbf{x}_f$ .

**Proposition 3.1.** *The control system in (3.9) is fully locally reachable.*

*Proof.* Let  $\mathcal{H}$  be a family of nonsingular involutive distributions containing the columns of  $G^1$  and being invariant under the drift vector field  $\mathbf{f}^1(\mathbf{x})$  and the columns of  $G^1$ .

**Lemma 3.1.** *The family of distributions  $\mathcal{H}$  has a minimal element [92].*

I denote the minimal element of  $\mathcal{H}$  by  $\mathcal{H}_0$  that has dimension  $\mathfrak{d}$ . At each state  $\mathbf{x}_0$  there is an open neighbourhood  $U_0 \subset \mathbb{R}^{2n-m}$  of  $\mathbf{x}_0$  on which  $\mathcal{H}_0$  defines a foliation of embedded  $\mathfrak{d}$ -dimensional slices in  $U_0$ . The slice containing  $\mathbf{x}_0$  is the set of all states that are reachable along trajectories of the system starting from  $\mathbf{x}_0$  and staying in  $U_0$ . This slice is called the reachable set from  $\mathbf{x}_0$  and it is denoted by  $\mathcal{R}_{\mathbf{x}_0} \subset U_0$ .

**Lemma 3.2.** *The system in (3.13) is fully locally reachable, if and only if  $\mathcal{H}_0$  is of system's dimension, i.e.,  $\mathfrak{d} = 2n - m$  [92].*

To construct  $\mathcal{H}_0$  for the system in (3.13), first the distribution spanned by the columns of matrix  $G^1$  is considered. Then, the invariance condition of  $\mathcal{H}_0$  under the drift vector field  $\mathbf{f}^1(\mathbf{x})$  is imposed that results in the distribution

$$\begin{aligned} \mathcal{K} &:= \text{im}(G^1) + \text{span}\{\mathcal{L}_{\mathbf{f}^1}G_j^1 | j = 1, \dots, \mathbf{n} - \mathbf{m}\} \\ &= \text{im}(G^1) \oplus \text{im} \begin{bmatrix} -N \\ \mathbb{O}_{(\mathbf{n}-\mathbf{m}) \times (\mathbf{n}-\mathbf{m})} \end{bmatrix}. \end{aligned} \quad (3.14)$$

Here,  $G_j^1$  is the  $j^{\text{th}}$  column of  $G^1$ , and  $\mathcal{K}$  is of dimension  $2\mathbf{n} - 2\mathbf{m}$ . The operators  $\text{im}(\cdot)$  and  $\text{span}(\cdot)$  refer to the image of a matrix and span of a set of vectors, respectively. Finally, since I assumed completely nonholonomic constraints in (3.3), the involutivity condition of  $\mathcal{H}_0$  results in at least a  $2\mathbf{n} - \mathbf{m}$ -dimensional distribution which is equal to the dimension of the system. Therefore, Based on dimension counting the dimension of  $\mathcal{H}_0$  is equal to that of the system, and (3.13) is fully locally reachable. Since the system in (3.13) is a special case of the system in (3.9), its fully locally reachability can be extended to the system in (3.9). ■

Reachability is the necessary condition for local controllability . A fully locally reachable system is locally controllable assuming that every initial state  $\mathbf{x}_0$  is in the interior of the reachable set  $\mathcal{R}_{\mathbf{x}_0}$  [93].

**Assumption 3.2.** The system in (3.13) and hence the system in (3.9) is locally controllable.

**Proposition 3.2.** *The systems in (3.9) is not full-state feedback linearizable by a smooth state feedback.*

*Proof.* A nonlinear control system is full-state feedback linearizable applying a smooth state feedback if and only if it is fully locally reachable and also a nested sequence of distributions defined by

$$\mathcal{F}_k := \text{span}\{\mathcal{L}_{\mathbf{f}}^i G_j | i = 0, \dots, k - 1, j = 1, \dots, \mathbf{n} - \mathbf{m}\}, \quad (3.15)$$

for  $k = 1, 2, \dots$ , are all involutive and constant dimensional [94].  $G_j$  denotes the  $j^{\text{th}}$

column of matrix  $G$ . The distribution  $\mathcal{F}_2$  is

$$\begin{aligned}\mathcal{F}_2 &= \text{im}(G) + \text{span}\{\mathcal{L}_{\mathbf{f}}G_j | j = 1, \dots, s\} \\ &= \text{im}(G) \oplus \text{im} \begin{bmatrix} -NM_r^{-1}B_r \\ W(q) \end{bmatrix},\end{aligned}\quad (3.16)$$

where  $G_j$  is the  $j^{\text{th}}$  column of  $G$  and  $W : Q \rightarrow \mathbb{R}^{(n-m) \times s}$ . Since  $\text{im}\left(\begin{bmatrix} \mathbb{O}_{s \times n} & W(q)^T \end{bmatrix}^T\right) \subset \text{im}(G)$  and  $\text{im}(G)$  covers all directions tangent to  $Q$ , based on the nonholonomicity of the constraints and positive definiteness of  $M_r$  and  $B_r$  being full rank,  $\mathcal{F}_2$  is not involutive and hence the system in (3.9) is not full-state linearizable by a smooth feedback. ■

### 3.3.2 Input-output Linearization and Output-tracking

Let the  $\mathbf{b}$ -dimensional vector  $\mathbf{y} \in \mathbb{R}^{\mathbf{b}}$  denote the output of the system in (3.13). I define the relationship between the states and the output of the system with the smooth function

$$\begin{aligned}\mathbf{h} : Q &\rightarrow \mathbb{R}^{\mathbf{b}} \\ \mathbf{q} &\mapsto \mathbf{y} = \mathbf{h}(\mathbf{q}).\end{aligned}\quad (3.17)$$

The relationship between the control input and the  $i^{\text{th}}$  component of the output is obtained by ( $i = 1, \dots, \mathbf{b}$ ):

$$\begin{aligned}\dot{\mathbf{y}}_i &= \mathcal{L}_{\dot{\mathbf{x}}}\mathbf{h}_i = \mathcal{L}_{\mathbf{f}^1}\mathbf{h}_i \\ \ddot{\mathbf{y}}_i &= \mathcal{L}_{\dot{\mathbf{x}}^2}\mathbf{h}_i = \mathcal{L}_{\mathbf{f}^1}^2\mathbf{h}_i + \mathcal{L}_{G^1\boldsymbol{\mu}}\mathcal{L}_{\mathbf{f}^1}\mathbf{h}_i.\end{aligned}\quad (3.18)$$

The Lie derivatives in (3.18) are calculated as:

$$\mathcal{L}_{\mathbf{f}^1}\mathbf{h}_i = \left(\frac{\partial \mathbf{h}_i}{\partial \mathbf{x}}\right)^T \mathbf{f}^1 = \left(\frac{\partial \mathbf{h}_i}{\partial \mathbf{q}}\right)^T N \boldsymbol{\eta} \quad (3.19)$$

$$\mathcal{L}_{\mathbf{f}^1}^2\mathbf{h}_i = \left(\frac{\partial(\mathcal{L}_{\mathbf{f}^1}\mathbf{h}_i)}{\partial \mathbf{x}}\right)^T \mathbf{f}^1 = \boldsymbol{\eta}^T N^T \frac{\partial^2 \mathbf{h}_i}{\partial \mathbf{q}^2} N \boldsymbol{\eta} + \sum_{j=1}^{n-m} \left(\left(\frac{\partial \mathbf{h}_i}{\partial \mathbf{q}}\right)^T \frac{\partial N_j}{\partial \mathbf{q}} N \boldsymbol{\eta}\right) \boldsymbol{\eta}_j$$

$$\mathcal{L}_{G^1\boldsymbol{\mu}}\mathcal{L}_{\mathbf{f}^1}\mathbf{h}_i = \left(\frac{\partial \mathbf{h}_i}{\partial \mathbf{q}}\right)^T N \boldsymbol{\mu} \quad (3.20)$$

where  $N_j$  denotes the  $j^{\text{th}}$  column of the matrix  $N$ ,  $\boldsymbol{\eta}_j$  is the  $j^{\text{th}}$  component of the

vector  $\boldsymbol{\eta}$ ,  $\frac{\partial}{\partial \mathbf{q}}$  is the Jacobian of a scalar or vector function, and  $\frac{\partial^2}{\partial \mathbf{q}^2}$  denotes the Hessian of a scalar function.

Let us define the input-output decoupling matrix

$$F := \frac{\partial \mathbf{h}}{\partial \mathbf{q}} N, \quad (3.21)$$

and the vector function  $\mathbf{w} : \mathcal{X} \rightarrow \mathbb{R}^b$ , whose  $i^{\text{th}}$  component is given in (3.20). Then, the input-output map is described by:

$$\ddot{\mathbf{y}} = \mathbf{w} + F\boldsymbol{\mu}. \quad (3.22)$$

**Assumption 3.3.** Hereinafter, the dimension of the output equals to the difference between the dimension of  $Q$  and the number of completely nonholonomic constraints. i.e.,  $b = n - m$ . Hence the decoupling matrix  $F$  is square.

**Assumption 3.4.** The decoupling matrix  $F$  is everywhere nonsingular.

*Remark 3.1.* Since the output is a smooth function on  $Q$ , and based on Assumption 3.2 and 3.4, the system in (3.9) along with the output defined in (3.17) is locally input-output controllable.

**Proposition 3.3.** *Based on Assumption 3 and 4, the system in (3.9) along with the output defined in (3.17) is input-output linearizable with relative degree 2, applying a static state feedback.*

*Proof.* Based on Assumption 3 and 4, the decoupling matrix  $F$  is everywhere invertible and hence the system in (3.13) along with the output in (3.17) is input-output linearizable applying the static state feedback:

$$\boldsymbol{\mu}(\mathbf{x}, \mathbf{u}) = F^{-1}(\mathbf{q})(\mathbf{u} - \mathbf{w}) \quad (3.23)$$

where the vector  $\mathbf{u} \in \mathbb{R}^b$  denotes the vector of control inputs in the resulting closed loop system. Under this feedback transformation, the input-output relation is in the form of a double integrator.

$$\ddot{\mathbf{y}} = \mathbf{u}. \quad (3.24)$$

Clearly, the control input obtained from substitution of (3.23) in (3.12) results in the same input-output linearized system in (3.24) for the system in (3.9).  $\blacksquare$

In (3.24) I introduce the external dynamics of the system in (3.9) along with the output in (3.17), applying the feedback transformation in (3.23) and (3.12). Hence, the state space  $\mathcal{X}$  can be partitioned into the  $2\mathbf{b}$ -dimensional space of external states denoted by  $\mathcal{Z}_2 \subset \mathcal{X}$  (the space of output and its velocity) and an  $(\mathbf{n} - \mathbf{b})$ -dimensional space of the internal states, denoted by  $\mathcal{Z}_1$ . The external states  $\mathbf{z}_2 \in \mathcal{Z}_2$  are in the following form:

$$\mathbf{z}_2 = \begin{bmatrix} \mathbf{y}^T & \dot{\mathbf{y}}^T \end{bmatrix}^T. \quad (3.25)$$

The components of the internal states  $\mathbf{z}_1 \in \mathcal{Z}_1$  are obtained as  $\mathbf{n} - \mathbf{b}$  arbitrary real valued functions  $\mathbf{z}_{1i} : \mathcal{X} \rightarrow \mathbb{R}$  satisfying two conditions: (i) the coordinate transformation mapping  $\mathfrak{T} : \mathcal{X} \rightarrow \mathcal{Z}_1 \times \mathcal{Z}_2$  that maps  $\mathbf{x}$  to the vector  $\mathbf{z} = [\mathbf{z}_1^T, \mathbf{z}_2^T]^T$  must be a local diffeomorphism, and (ii) the dynamics of the internal states must be independent of  $\boldsymbol{\tau}$ , i.e.,

$$\left(\frac{\partial \mathbf{z}_{1i}}{\partial \mathbf{x}}\right)^T G = 0 \quad i = 1, \dots, \mathbf{n} - \mathbf{b}. \quad (3.26)$$

**Proposition 3.4.** *Real-valued functions  $\mathbf{z}_{1i}$  locally exist for the system in (3.9) with the output in (3.17).*

*Proof.* This proposition is a direct consequence of Theorem 13.1 in [24]. ■

The internal/external state decomposition (known as the normal form) for the system in (3.9) is expressed as:

$$\begin{aligned} \dot{\mathbf{z}}_1 &= \boldsymbol{\omega}(\mathbf{z}_1, \mathbf{z}_2) \\ \dot{\mathbf{z}}_2 &= A_c^2 \mathbf{z}_2 + B_c^2 \mathbf{u} \end{aligned} \quad (3.27)$$

where the  $i^{th}$  component of  $\boldsymbol{\omega}$  is

$$\boldsymbol{\omega}_i = \left( \frac{\partial \mathfrak{T}}{\partial \mathbf{x}} \mathbf{f}(\mathfrak{T}^{-1}(\mathbf{z})) \right)_i, \quad i = 1 \dots \mathbf{n} - \mathbf{b} \quad (3.28)$$

and  $A_c^2 \in \mathbb{R}^{2\mathbf{b} \times 2\mathbf{b}}$  and  $B_c^2 \in \mathbb{R}^{2\mathbf{b} \times \mathbf{b}}$  are the constant matrices representing the conical form of a chain of two integrators.

A local diffeomorphism as a state transformation can also be defined to partition the space of internal states into: (i) the  $\mathbf{a}$ -dimensional space  $\mathcal{Z}_1^o \subset \mathcal{Z}_1$  containing the observable internal states from the output in (3.17) for the control system in (3.9), and (ii)  $(\mathbf{n} - \mathbf{b} - \mathbf{a})$ -dimensional space  $\mathcal{Z}_1^u \subset \mathcal{Z}_1$  containing the states that are unobservable from the output in (3.17) for both control systems in (3.27) and (3.9).

Let us consider the elements  $\mathbf{z}_1^o \in \mathcal{Z}_1^o$  and  $\mathbf{z}_1^u \in \mathcal{Z}_1^u$ . Based on this decomposition, the system in (3.27) can be further transformed to

$$\begin{aligned}\dot{\mathbf{z}}_1^u &= \boldsymbol{\omega}^u(\mathbf{z}_1^u, \mathbf{z}_1^o, \mathbf{z}_2) \\ \dot{\mathbf{z}}_1^o &= \boldsymbol{\omega}^o(\mathbf{z}_1^o, \mathbf{z}_2) \\ \dot{\mathbf{z}}_2 &= A_c^2 \mathbf{z}_2 + B_c^2 \mathbf{u},\end{aligned}\tag{3.29}$$

where the functions  $\boldsymbol{\omega}^u$  and  $\boldsymbol{\omega}^o$  describe the dynamics of the observable and unobservable internal states, respectively.

*Remark 3.2.* Given the fact that the observability decomposition is dependent on the output function, this decomposition is discussed in details in Section 3.4 for a specific output function.

I denote the desired trajectories for the external states by  $\mathbf{z}_{2d}(t)$ , for the observable internal states by  $\mathbf{z}_{1d}^o(t)$ , and for the unobservable internal states by  $\mathbf{z}_{1d}^u(t)$ , where  $t \in \mathbb{R}^+$  refers to time.

*Remark 3.3.* Based on Assumption 3, the system in (3.9) is not kinematically redundant. Hence,  $\mathbf{z}_{1d}^o(t)$  and  $\mathbf{z}_{1d}^u(t)$  are uniquely determined based on  $\mathbf{z}_{2d}(t)$  and the initial desired configuration of the system, applying the set of kinematic equations in (3.6).

The tracking error dynamics of the system in (3.29) can be formed as

$$\begin{aligned}\dot{\mathbf{z}}_{1e}^u &= \boldsymbol{\omega}_e^u(\mathbf{z}_{1e}^u, \mathbf{z}_{1e}^o, \mathbf{z}_{2e}, t), \\ \dot{\mathbf{z}}_{1e}^o &= \boldsymbol{\omega}_e^o(\mathbf{z}_{1e}^o, \mathbf{z}_{2e}, t), \\ \dot{\mathbf{z}}_{2e} &= A_c \mathbf{z}_{2e} + B_c \mathbf{v},\end{aligned}\tag{3.30}$$

where  $\mathbf{z}_{1e}^o := \mathbf{z}_1^o - \mathbf{z}_{1d}^o(t)$  is the tracking error of the observable internal states,  $\mathbf{z}_{1e}^u := \mathbf{z}_1^u - \mathbf{z}_{1d}^u(t)$  is the tracking error of the unobservable internal states,  $\mathbf{z}_{2e} := \mathbf{z}_2 - \mathbf{z}_{2d}$  is the tracking error of external states and finally  $\mathbf{v} := \mathbf{u} - \ddot{\mathbf{y}}_d(t)$ . The functions  $\boldsymbol{\omega}_e^u$  and  $\boldsymbol{\omega}_e^o$  respectively describe the error dynamics of the observable and unobservable internal states, based on (3.29).

*Remark 3.4.* Since the elements of  $\mathcal{Z}_1^u$  are not affecting the output in (3.17) for the control system in (3.9), their asymptotic stability in an output-tracking control problem is of less importance as long as they are bounded.

*Problem 3.1 (Output-tracking Control Problem).* Given a twice differentiable desired feasible trajectory  $\mathbf{y}_d(\mathbf{t})$  for the output of the system, find a control law  $\mathbf{v}$  that

tracks  $\mathbf{z}_{2d}(t)$  with an asymptotically stable tracking errors  $\mathbf{z}_{2e}$  and  $\mathbf{z}_{1e}^o$ , and a bounded tracking error  $\mathbf{z}_{1e}^u$ .

The stability of the tracking error for the elements of  $\mathcal{Z}_1^o$  can be investigated based on the concept of tracking-error zero dynamics. The tracking-error zero dynamics is the error dynamics of the internal states when the output error is kept identically zero applying an appropriate control input. Accordingly, the tracking-error zero dynamics of  $\mathbf{z}_{1e}^o$  is

$$\dot{\mathbf{z}}_{1e}^o = \boldsymbol{\omega}_e^o(\mathbf{z}_{1e}^o, 0, t) \quad (3.31)$$

**Assumption 3.5.** The function  $\boldsymbol{\omega}_e^o$  is locally Lipschitzian in  $(\mathbf{z}_{1e}^o, \mathbf{z}_{2e})$ , uniformly with respect to  $t \geq 0$ .

**Proposition 3.5.** *If the tracking-error zero dynamics in (3.31) is locally uniformly asymptotically stable, then  $\mathbf{z}_{1e}^o$  is locally uniformly asymptotically stable, after determining  $\mathbf{v}$  as a solution of output tracking control problem.*

*Proof.* Considering Assumption 3.5, this proposition is the direct consequence of lemma B.2.4 on page 514 in [92]. ■

**Assumption 3.6.** I assume that the tracking error  $\mathbf{z}_{1e}^u$  is bounded, if the tracking errors  $\mathbf{z}_{2e}$  and  $\mathbf{z}_{1e}^o$  are both locally uniformly asymptotically stable and the desired trajectories are bounded.

## 3.4 Implementation on a Six-wheel Type (1, 1) Autonomous Lunar Rover

In this section, the developed theory is implemented on a Lunar six-wheel type (1, 1) autonomous rover. Type (1, 1) autonomous rovers is referring to the category of such systems whose motion in only one direction (forward/backward) can be directly controlled and their orientation is indirectly controlled during the forward/backward motion through a single steering command [51].

*Remark 3.5.* In type (1, 1) autonomous rovers, system may contain more than one steering degree-of-freedom, but to ensure mobility of the system axes of rotations of all steerable wheels must intersect at the center of turning (Ackerman Condition). See Fig. 3.1. This results in holonomic constraints between steering degrees of freedom and hence system indirectly rotates by a single steering command.

The system under study can be modelled as the composition of a main body which is the most massive part of the rover and six driven wheels located on three parallel axes and connected to the main body by ideal joints. Wheels located on centre and rear axes can only have axial rotation while the front wheels are allowed to have both steering and axial rotation relative to the main body. To each part, a body-fixed coordinate frame is assigned. For the main body, the origin of the coordinate frame is located at the middle of the center wheels' axis, its  $x$ -axis is aligned with the rover's forward direction of motion and its  $y$ -axis is in the lateral direction pointing towards the port side ( $xy$ -frame). For the wheels, the assigned body coordinate frames are located at the centre of the wheels and their axes are parallel to those of main body frame when axial rotation and steering angles are all equal to zero. The schematic of the system is depicted in Fig. 3.1, where  $x_0y_0$ -frame is the inertial coordinate frame, the vector  $[x_{cm} \ y_{cm}]^T$  denotes the position of the main body's centre of mass in  $xy$ -frame,  $2c$  is the lateral distance between the wheels, and  $L$  and  $L_0$  are respectively the longitudinal distances between the front and rear wheels from the origin of  $xy$ -frame. Further, the radius of the wheels is denoted by  $R_w$ . Assuming that the system

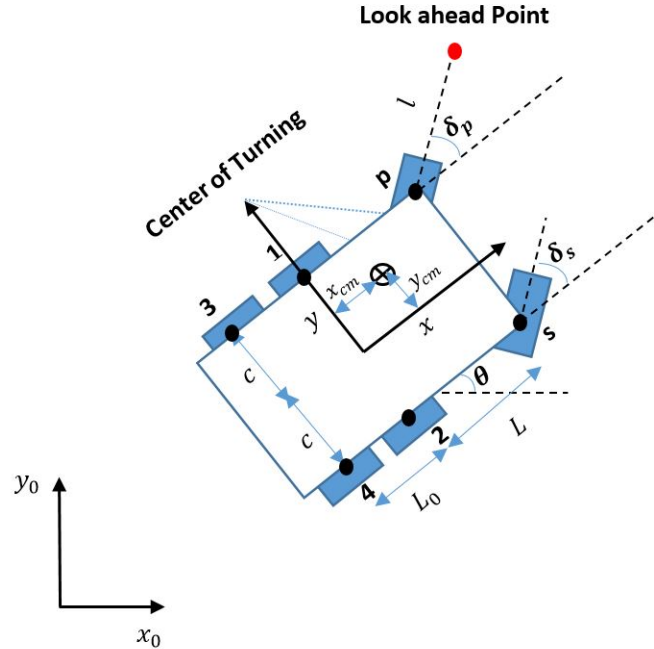


Figure 3.1: Schematic of the system

only has planar motion, the configuration manifold of the system  $\hat{Q} = \text{SE}(2) \times \mathbb{T}^8$

(Cartesian product of Special Euclidean group and 8-torus) is 11 dimensional, i.e.,  $\hat{\mathbf{n}} = 11$ , and the generalized coordinates of the system are

$$\hat{\mathbf{q}} = \left[ x_b \ y_b \ \theta \ \psi_s \ \delta_s \ \psi_1 \ \psi_2 \ \psi_3 \ \psi_4 \ \psi_p \ \delta_p \right]^T \in \hat{Q}. \quad (3.32)$$

Here,  $[x_b \ y_b \ \theta]^T \in \text{SE}(2)$  is the position and orientation of  $xy$ -frame from  $x_0y_0$ -frame and expressed in the inertial frame,  $\psi_s, \psi_p \in \mathbb{T}^1$  are respectively the rotation of the starboard and port front wheels,  $\delta_s, \delta_p \in \mathbb{T}^1$  are the steering angle of the starboard and port front wheels, respectively, and  $\psi_1, \psi_2, \psi_3, \psi_4 \in \mathbb{T}^1$  refer to the axial rotations of port center wheel, starboard center wheel, port rear wheel, and starboard rear wheel, respectively.

The imposed constraints on the system are (i) a constraint between steering angles of the front wheels due to the Ackerman condition, and (ii) the no longitudinal and lateral slip condition at all wheels, except rear wheels. Considering the rover's mobility, the no-lateral velocity constraint at the rear wheels is relaxed in this thesis, and they are assumed to skid-steer.

Accordingly, the number of everywhere linearly independent constraints is  $\mathbf{r} = 9$  and the constraint matrix  $\hat{A}$  is formed as in (3.33).

$$\hat{A}(\hat{\mathbf{q}}) = \begin{bmatrix} 0 & 0 & 0 & 0 & 1 & 0 & 0 & 0 & 0 & 0 & 0 & -\frac{df_A}{d\delta_p} \\ -\sin(\delta_p + \theta) & \cos(\delta_p + \theta) & L \cos(\delta_p) + c \sin(\delta_p) & 0 & 0 & 0 & 0 & 0 & 0 & 0 & 0 & 0 \\ -\sin(\theta) & \cos(\theta) & 0 & 0 & 0 & 0 & 0 & 0 & 0 & 0 & 0 & 0 \\ \cos(\delta_p + \theta) & \sin(\delta_p + \theta) & L \sin(\delta_p) - c \cos(\delta_p) & 0 & 0 & 0 & 0 & 0 & 0 & -R_w & 0 & 0 \\ \cos(\delta_s + \theta) & \sin(\delta_s + \theta) & L \sin(\delta_s) + c \cos(\delta_s) & -R_w & 0 & 0 & 0 & 0 & 0 & 0 & 0 & 0 \\ \cos(\theta) & \sin(\theta) & -c & 0 & 0 & -R_w & 0 & 0 & 0 & 0 & 0 & 0 \\ \cos(\theta) & \sin(\theta) & c & 0 & 0 & 0 & -R_w & 0 & 0 & 0 & 0 & 0 \\ \cos(\theta) & \sin(\theta) & -c & 0 & 0 & 0 & 0 & -R_w & 0 & 0 & 0 & 0 \\ \cos(\theta) & \sin(\theta) & c & 0 & 0 & 0 & 0 & 0 & -R_w & 0 & 0 & 0 \end{bmatrix} \quad (3.33)$$

The first row of  $\hat{A}$  captures the constraint between the steering degrees of freedom, where

$$\delta_s = f_A(\delta_p) = \tan^{-1} \left( \frac{\tan(\delta_p)}{1 + \frac{2c \tan(\delta_p)}{L}} \right). \quad (3.34)$$

The second and third rows of  $\hat{A}$  refer to the no-lateral velocity constraint at the wheel-ground contact point of the port front wheel and the center wheels, respectively. The remaining rows correspond to the no-longitudinal velocity constraint at the wheel-ground contact point of all six wheels.

*Remark 3.6.* Since the center wheels are always parallel, their corresponding no-lateral velocity constraints are linearly dependant. Hence, to include both constraints only one equation is considered when forming  $\hat{A}$ . Further, since the steering angles are assumed to satisfy the Ackerman condition, the no-lateral velocity constraint at the starboard front wheel is linearly dependant on the second and third rows of  $\hat{A}$ ; and hence it is excluded, when forming  $\hat{A}$ .

Based on the Lagrange d'Alembert principle, the equations of motion of the rover are derived. The matrices  $\hat{M}(\theta)$  and  $\hat{C}(\theta, \dot{\mathbf{q}})$  in (3.2) are obtained and presented in Appendix A. Assuming that only planar motion is allowed, the vector  $\hat{\mathbf{g}} \equiv 0$ . The vector of control inputs  $\boldsymbol{\tau}$  consists of the torques applied to all wheels collocated to their axial motion along with the steering torques applied to the front wheels, i.e.,  $\dim(\boldsymbol{\tau}) = \mathfrak{s} = 8$  and the matrix of control directions  $\hat{B}$  is

$$\hat{B} = \begin{bmatrix} \mathbb{O}_{3 \times 8} & \mathbb{I}_{8 \times 8} \end{bmatrix}^T. \quad (3.35)$$

Based on the imposed constraints, one possible choice of matrix  $\hat{N}$  is:

$$\hat{N} = \begin{bmatrix} \frac{R_w}{L} \cos(\theta)(L \cos(\delta_p) + c \sin(\delta_p)) & 0 \\ \frac{R_w}{L} \sin(\theta)(L \cos(\delta_p) + c \sin(\delta_p)) & 0 \\ \frac{R_w}{L} \sin(\delta_p) & 0 \\ \hat{N}_{4,1} & 0 \\ 0 & \hat{N}_{5,2} \\ \cos(\delta_p) & 0 \\ \frac{2c}{L} \sin(\delta_p) + \cos(\delta_p) & 0 \\ \cos(\delta_p) & 0 \\ \frac{2c}{L} \sin(\delta_p) + \cos(\delta_p) & 0 \\ 1 & 0 \\ 0 & 1 \end{bmatrix}, \quad (3.36)$$

where

$$\begin{aligned}\hat{N}_{4,1} &= \sin(\delta_p) \left( \frac{2c}{L} \cos(\delta_s) + \sin(\delta_s) \right) + \cos(\delta_p) \cos(\delta_s), \\ \hat{N}_{5,2} &= \frac{L^2}{2c^2 + L^2 - 2c^2 \cos(2\delta_p) + 2cL \sin(2\delta_p)}.\end{aligned}$$

The dimension of the involutive closure of the distribution  $\mathcal{D} = \text{im}(\hat{N})$  is calculated using Wolfram Mathematica software and it is equal to seven. This means that the system experiences  $9 - (11 - 7) = 5$  completely nonholonomic constraints. In addition to the Ackerman condition, which is the holonomic constraint reflected in the first row of  $\hat{A}$ , system experiences three other holonomic constraints:

- (i) Subtracting the constraint equation associated with the seventh row of  $\hat{A}$  from that associated with its sixth row leads to a holonomic constraint between the rotation of the main body and axial rotations of the center wheels:

$$\begin{aligned}-2c\dot{\theta} - R_w(\dot{\psi}_1 - \dot{\psi}_2) &= 0 \\ \Rightarrow \theta - \frac{R_w}{2c}(\psi_2 - \psi_1) &= 0\end{aligned}\tag{3.37}$$

- (ii) Similarly, repeating the same procedure for the last two rows of  $\hat{A}$ , I obtain:

$$\begin{aligned}-2c\dot{\theta} - R_w(\dot{\psi}_4 - \dot{\psi}_3) &= 0 \\ \Rightarrow \theta - \frac{R_w}{2c}(\psi_4 - \psi_3) &= 0.\end{aligned}\tag{3.38}$$

Accordingly by equating (3.37) and (3.38), the following equivalent holonomic constraint is obtained.

$$(\psi_2 - \psi_1) - (\psi_4 - \psi_3) = 0.\tag{3.39}$$

- (iii) Finally, subtracting the summation of the constraint equations corresponding to the sixth and seventh rows of  $\hat{A}$  from the summation of the constraint equations corresponding to its last two rows, the following holonomic constraint is formed.

$$(\dot{\psi}_2 + \dot{\psi}_1) - (\dot{\psi}_4 + \dot{\psi}_3) = 0 \Rightarrow (\psi_2 + \psi_1) - (\psi_4 + \psi_3) = 0\tag{3.40}$$

**Assumption 3.7.** In this thesis, it is assumed that based on the assignment of body coordinate frames, the integration constant after integrating the holonomic constraint equations are all equal to zero.

Combining (3.37)-(3.40), I derive the following set of holonomic constraint equations to be imposed on the system.

$$\begin{aligned}\theta - \frac{R_w}{2c}(\psi_2 - \psi_1) &= 0, \\ \psi_1 - \psi_3 &= 0, \\ \psi_2 - \psi_4 &= 0.\end{aligned}\tag{3.41}$$

According to all holonomic constraints, I form the 7-dimensional restricted configuration manifold  $Q = \mathbb{R}^2 \times \mathbb{T}^5$  whose elements are denoted by  $\mathbf{q} = [x_b \ y_b \ \psi_s \ \psi_1 \ \psi_2 \ \psi_p \ \delta_p]^T$  and I have the inclusion map

$$\hat{\mathbf{q}} = \iota_Q(\mathbf{q}) = \left[ x_b \ y_b \ \frac{R_w}{2c}(\psi_2 - \psi_1) \ \psi_s \ f_A(\delta_p) \ \psi_1 \ \psi_2 \ \psi_1 \ \psi_2 \ \psi_p \ \delta_p \right]^T \tag{3.42}$$

Therefore, the nonzero elements of the Jacobian of this inclusion map  $J$  are

$$\begin{aligned}J_{1,1} &= J_{2,2} = J_{4,3} = J_{6,4} = J_{7,5} \\ &= J_{8,4} = J_{9,5} = J_{10,6} = J_{11,7} = 1 \\ J_{3,4} &= -J_{3,5} = \frac{-R_w}{2c} \\ J_{5,7} &= \frac{df_A}{d\delta_p}(\delta_p)\end{aligned}\tag{3.43}$$

The constraint matrix  $A$  associated with the remaining linearly independent nonholonomic constraints is obtained based on (3.4), where the matrix

$$E = \begin{bmatrix} \mathbb{O}_{5 \times 1} & \mathbb{I}_{5 \times 5} & \mathbb{O}_{5 \times 3} \end{bmatrix}.\tag{3.44}$$

I choose the directly measurable states of the rotational velocity and steering velocity of the port front wheel as the 2-dimensional quasi-velocity vector, i.e.,  $\boldsymbol{\eta} =$

$\begin{bmatrix} \dot{\psi}_p & \dot{\delta}_p \end{bmatrix}^T$ . Hence, the matrix  $N$  is identified as

$$N = \begin{bmatrix} \frac{R_w}{L} \cos(\theta)(L \cos(\delta_p) + c \sin(\delta_p)) & 0 \\ \frac{R_w}{L} \sin(\theta)(L \cos(\delta_p) + c \sin(\delta_p)) & 0 \\ \hat{N}_{4,1} & 0 \\ \cos(\delta_p) & 0 \\ \frac{2c}{L} \sin(\delta_p) + \cos(\delta_p) & 0 \\ 1 & 0 \\ 0 & 1 \end{bmatrix}. \quad (3.45)$$

The reduced state space representation in (3.9) for the autonomous Lunar rover can now be formulated based on the determined matrices  $N$ ,  $J$ ,  $\hat{B}$ ,  $\hat{M}$ , and  $\hat{C}$  (see Appendix A), and the definition of  $\boldsymbol{\eta}$  and the map  $\iota_Q$ . Note that the vector of system states is  $\mathbf{x} = [\mathbf{q}^T, \boldsymbol{\eta}^T]^T \in \mathcal{X}$ .

The output functions for various types of rovers that make the system in (3.9) input-output linearizable by applying static state feedback is presented in [56]. The type (1, 1) autonomous rover systems are input-output linearizable by applying static state feedback, if the inertial location of a virtual reference point in front of the steerable port front wheel (look-ahead point) is defined as the output (see Fig.3.1). This output function and its corresponding decoupling matrix  $F$  are respectively

$$\mathbf{y}(\mathbf{q}) = \begin{bmatrix} x_b + L \cos(\theta) - c \sin(\theta) + l \cos(\delta_p + \theta) \\ y_b + L \sin(\theta) + c \cos(\theta) + l \sin(\delta_p + \theta) \end{bmatrix}, \quad (3.46)$$

$$F = \begin{bmatrix} \frac{R_w}{L} (L \cos(\theta + \delta_p) - l \sin(\delta_p + \theta) \sin(\delta_p)) & -l \sin(\delta_p + \theta) \\ \frac{R_w}{L} (L \sin(\theta + \delta_p) + l \cos(\theta + \delta_p) \sin(\delta_p)) & l \cos(\theta + \delta_p) \end{bmatrix}, \quad (3.47)$$

where  $l > 0$  is the distance between the look-ahead point and the center of port front

wheel and  $\theta$  is substituted from (3.41). With this choice of output the determinant of the decoupling matrix  $F$  is equal to  $lR_w$  and it is everywhere full rank. Therefore, the system is input-output linearizable applying static state feedbacks in (3.12) and (3.23).

**Proposition 3.6** (observability). *For the system under study, considering the state space representation in (3.9) and output in (3.46), the axial rotation of both front wheels  $\psi_s$ ,  $\psi_p$  along with the summation of the axial rotation of the center wheels  $\psi_1 + \psi_2$  are locally unobservable at all states.*

*Proof.* Let  $\mathcal{S}$  be a family of nonsingular involutive co-distributions, being invariant under the drift vector field  $\mathbf{f}(\mathbf{x})$  and the columns of  $G(\mathbf{x})$  in (3.9) and they contain the span of exact co-vector fields corresponding to the components of the output in (3.46):

$$\mathcal{G}_0 := \text{span}\left\{\left(\frac{\partial \mathbf{y}_1}{\partial \mathbf{x}}\right)^T, \left(\frac{\partial \mathbf{y}_2}{\partial \mathbf{x}}\right)^T\right\}. \quad (3.48)$$

**Lemma 3.3.** *The set of co-distributions  $\mathcal{S}$  has a minimal element [92].*

I denote the minimal element of  $\mathcal{S}$  by  $\mathcal{S}_0$  and its involutive annihilator distribution by  $\mathcal{S}_0^\perp$ . At each state  $\mathbf{x}_0 \in \mathcal{X}$  there is an open neighbourhood  $U_0 \subset \mathcal{X}$  of  $\mathbf{x}_0$  on which the integral of  $\mathcal{S}_0^\perp$  defines a foliation of largest possible embedded slices with dimension equal to that of  $\mathcal{S}_0^\perp$  in  $U_0$  containing the unobservable states from the output in (3.46).

To construct  $\mathcal{S}_0$  for the system under study based on (3.9) and (3.46), first the co-distribution  $\mathcal{G}_0$  is formed. Since  $\mathbf{y}$  is only a function of  $\mathbf{q}$ , the Lie-bracket of any co-vector field in  $\mathcal{G}_0$  with respect to columns of  $G(\mathbf{x})$  remains in  $\mathcal{G}_0$  and hence  $\mathcal{G}_0$  is invariant under the columns of  $G(\mathbf{x})$ . Then, the invariance condition of elements of  $\mathcal{S}_0$  under the drift vector field  $\mathbf{f}$  is checked. For the first basis element of  $\mathcal{G}_0$  this condition results in the co-distribution  $\mathcal{G}_1$ :

$$\mathcal{G}_1 = \mathcal{G}_0 + \text{span}\left\{\mathcal{L}_{\mathbf{f}}\left(\frac{\partial \mathbf{y}_1}{\partial \mathbf{x}}\right)^T\right\}, \quad (3.49)$$

where

$$\mathcal{L}_{\mathbf{f}}\left(\frac{\partial \mathbf{y}_1}{\partial \mathbf{x}}\right)^T = \mathbf{f}^T \left(\frac{\partial^2 \mathbf{y}_1}{\partial \mathbf{x}^2}\right)^T + \left(\frac{\partial \mathbf{y}_1}{\partial \mathbf{x}}\right)^T \frac{\partial \mathbf{f}}{\partial \mathbf{x}}. \quad (3.50)$$

For the system under study this Lie derivative is calculated using Wolfram Mathematica and the result is a co-vector field that is always traverse to  $\mathcal{G}_0$ . Therefore,  $\mathcal{G}_1$  is of dimension 3. Repeating the same procedure for the second basis element of  $\mathcal{G}_0$ ,

I obtain the four dimensional co-distribution  $\mathcal{G}_2$ :

$$\mathcal{G}_2 = \mathcal{G}_1 \oplus \text{span}\left\{\mathcal{L}_f\left(\frac{\partial \mathbf{y}_2}{\partial \mathbf{x}}\right)^T\right\}. \quad (3.51)$$

Based on the normal form in (3.27), I have at least 4 observable states, i.e., output and its velocity, which is consistent with what I have found so far. Imposing the involutivity condition, the co-distribution  $\mathcal{S}_0$  is obtained as the involutive closure of  $\mathcal{G}_2$ . Calculating  $\mathcal{G}_2$  and its involutive closure using Wolfram Mathematica software, the annihilator distribution of  $\mathcal{S}_0$  at non-zero velocity states of the system is obtained as

$$\mathcal{S}_0^\perp = \begin{bmatrix} 0 & 0 & 0 & 1 & 1 & 0 & 0 & 0 & 0 \\ 0 & 0 & 0 & 0 & 0 & 1 & 0 & 0 & 0 \\ 0 & 0 & 1 & 0 & 0 & 0 & 0 & 0 & 0 \end{bmatrix}^T. \quad (3.52)$$

To obtain the unobservable states, the distribution  $\mathcal{S}_0^\perp$  needs to be integrated. Hence, the unobservable states are  $\{\psi_1 + \psi_2, \psi_p, \psi_s\}$ .

The dimension of the co-distribution  $\mathcal{S}_0$  for the system under study based on the state space representation in (3.9) along with the output in (3.46), differs at different states of the system. For example, when the system is stationary the dimension of  $\mathcal{S}_0$  is 4, i.e., the system contains  $9 - 4 = 5$  unobservable states (only output and its velocities are observable). However, the maximum dimension of  $\mathcal{S}_0$  is 6 indicating that regardless of the state, the system always has at least the 3 unobservable states identified earlier. ■

To construct the normal form state space representation in (3.29) for the system under study, including the observability decomposition of the internal dynamics, I introduce  $\mathbf{z}_1^o = \left[\theta = \frac{R_w}{2c}(\psi_2 - \psi_1) \quad \delta_p\right]^T$ ,  $\mathbf{z}_1^u = \left[\psi_2 + \psi_1 \quad \psi_s \quad \psi_p\right]^T$ , and

$$\mathbf{z}_2 = \left[z_6 \quad z_7 \quad z_8 \quad z_9\right]^T := \left[\mathbf{y}^T \quad \dot{\mathbf{y}}^T\right]^T. \quad (3.53)$$

It can be simply validated that this set of internal states satisfies the condition in (3.26) and the state transformation  $\mathfrak{T}$  is a diffeomorphism. Accordingly, the functions

$\boldsymbol{\omega}^u$  and  $\boldsymbol{\omega}^o$  in (3.29) for the system under study are

$$\begin{aligned}\boldsymbol{\omega}^u &= N^u(\delta_p) F^{-1} \begin{bmatrix} z_8 \\ z_9 \end{bmatrix} \\ \boldsymbol{\omega}^o &= N^o(\delta_p) F^{-1} \begin{bmatrix} z_8 \\ z_9 \end{bmatrix}\end{aligned}\tag{3.54}$$

where

$$\begin{aligned}N^o &= \begin{bmatrix} \frac{R_w \sin(\delta_p)}{L} & 0 \\ 0 & 1 \end{bmatrix}, \\ N^u &= \begin{bmatrix} \hat{N}_{4,1} & 0 \\ \frac{2c}{L} \sin(\delta_p) + 2 \cos(\delta_p) & 0 \\ 1 & 0 \end{bmatrix}.\end{aligned}\tag{3.55}$$

The tracking-error zero dynamics corresponding to  $\mathbf{z}_1^o$  is formed as:

$$\begin{aligned}\dot{\theta}_e &= \begin{bmatrix} \frac{R_w \sin(\delta_p)}{L} & 0 \end{bmatrix} F^{-1} \begin{bmatrix} z_{8d} \\ z_{9d} \end{bmatrix} - \dot{\theta}_d \\ \dot{\delta}_{pe} &= \begin{bmatrix} 0 & 1 \end{bmatrix} F^{-1} \begin{bmatrix} z_{8d} \\ z_{9d} \end{bmatrix} - \dot{\delta}_{pd},\end{aligned}\tag{3.56}$$

where  $\theta_e$  and  $\delta_{pe}$  respectively refer to the error in  $\theta$  and  $\delta_p$ , and  $z_{8d}$ ,  $z_{9d}$ ,  $\dot{\theta}_d$ , and  $\dot{\delta}_{pd}$  denote the desired velocities of the output,  $\theta$ , and  $\delta_p$ , respectively. Applying Lyapunov's indirect method, it is proved that based on this choice of output for type (1, 1) rovers, the tracking-error zero dynamics and consequently the error dynamics of  $\mathbf{z}_1^o$  is asymptotically stable, if the system moves in forward direction, and it is unstable during backward motion [56]. During backward motion when the system is slightly perturbed, it completely turns and continues its motion in forward direction. The reasons behind this behaviour are: (i) the location of the virtual reference point is in

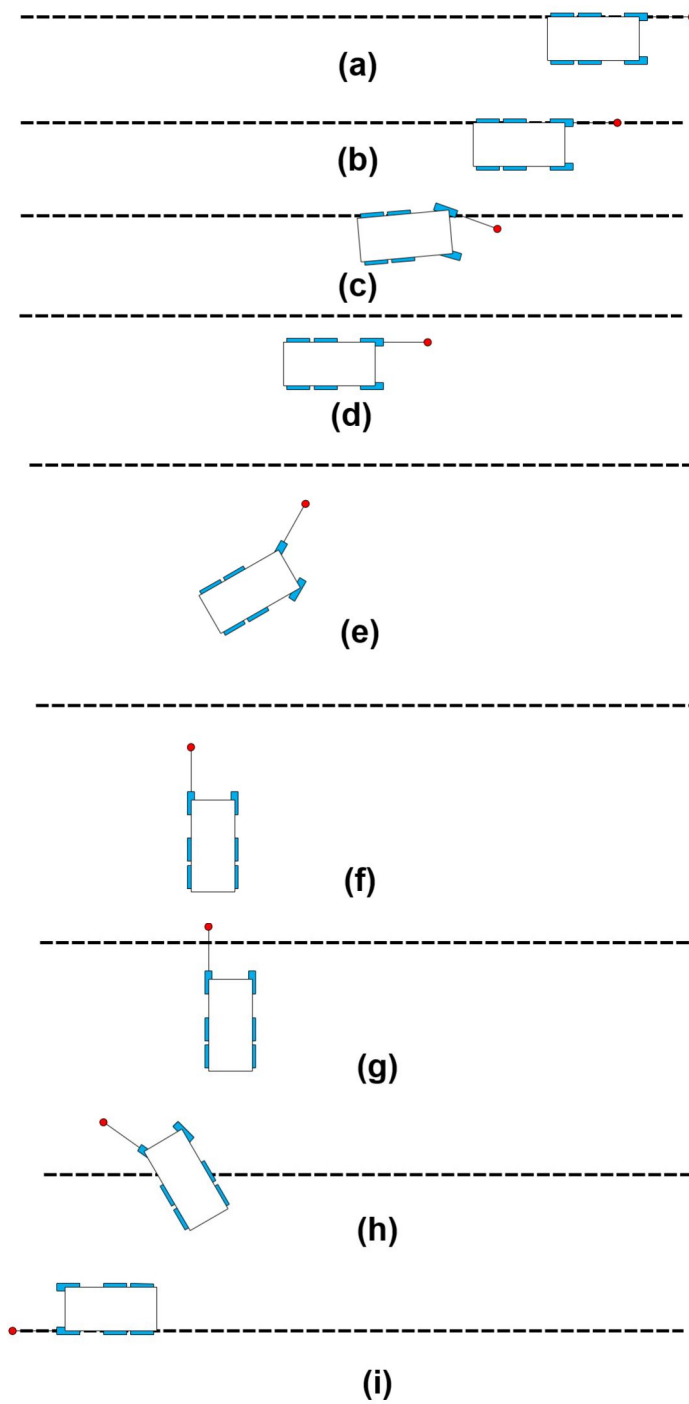


Figure 3.2: The unstable behaviour of the system during backward motion

front of the center of rotation of the system located at the middle of center wheels' axis. (rear wheels are allowed to skid), and (ii) in backward motion the rotation of the main body is in opposite direction of the steering.

This non-minimum phase behaviour during backward motion can be resolved by revising the output in (3.46) in order for the virtual reference point to be behind the center of rotation (look-behind case) and to turn in the negative direction of the steering.

**Assumption 3.8.** In this thesis, I assume that the Lunar autonomous rover only moves in forward direction, and hence  $\mathbf{z}_{1e}^o$  is asymptotically stable towards origin based on the output defined in 3.46.

*Remark 3.7.* Since for the Lunar rover the dynamics of  $\mathbf{z}_1^u$  in (3.29) only depends on  $\mathbf{z}_1^o$  and  $\mathbf{z}_2$ , and  $\mathbf{z}_{2e}$  and  $\mathbf{z}_{1e}^o$  are asymptotically stable due to the proposed output-tracking control law in (4.14) and Assumption 3.8, respectively, the error dynamics  $\dot{\mathbf{z}}_{1e}^u \rightarrow 0$  while  $t \rightarrow \infty$ ; and hence  $\mathbf{z}_1^u$  is bounded.

## 3.5 Summary

In this chapter, a reduced state-space representation of the governing equations of motion of constrained mechanical systems was proposed. It was proved that such systems are fully locally reachable, and fully locally controllable under the assumption that both initial and terminal states are in the interior of the reachable set. However, due to the nonholonomicity of the constraints, such systems are not full-state linearizable, but they are input-output linearizable if the input-output decoupling matrix is everywhere invertible. The input-output linearization was performed and the internal-external state decomposition (normal form) was obtained. To investigate the stability of the internal dynamics, internal states were also decomposed into the set of states which are observable from the output before applying the feedback transformation and the unobservable ones. Since the unobservable internal states are not affecting the output, their asymptotic stability towards the desired trajectory is of less importance if they are bounded. The concept of tracking-error zero dynamics was defined to examine the asymptotic stability of the observable internal states. Finally, a six-wheel type (1, 1) autonomous rover was considered as the case study, and it was shown that it is input-output linearizable if the location of a virtual reference

point in front of the steerable wheel is defined as the output. Based on this output, the steering angle and the rotation of the body are observable internal states, and the rotations of the wheels are unobservable internal states. It was shown that if the rover moves in the forward direction the observable internal states are asymptotically stable and the unobservable internal states are bounded.

## Chapter 4

# Robust Optimal Output Tracking

### 4.1 Overview

The input-output feedback linearized control system in (3.27) is only valid if all system's parameters are completely known and the system is not subject to any disturbances. In this chapter, a control law is proposed based on Sliding Mode Control (SMC) scheme to ensure robustness against bounded time-dependant matched uncertainties in the inertia parameters. Applying the input-output linearization feedback transformation to the nominal plant, an uncertain input-output map is introduced. Then, an optimal sliding manifold is proposed based on the finite-horizon linear-quadratic regulator design problem with split boundary value conditions. In the next stage, a switching control law is proposed and its stability towards the sliding manifold is proved using Lyapunov's direct method. To alleviate the chattering effect, the method of boundary layer is implemented. The developed theory is implemented on the type (1,1) six-wheel autonomous Lunar rover and its efficacy is compared to the proposed optimal proportional integral derivative (PID) controller through a developed simulation environment.

### 4.2 Uncertain Model

**Assumption 4.1.** In this thesis, perfect sensory data acquisition and complete knowledge of kinematic (geometric) parameters of the system is assumed.

Let us introduce a time-dependant  $\mathbf{c}$ -dimensional vector of uncertain inertia parameters and disturbance forces  $\boldsymbol{\rho}$  in a bounded neighbourhood  $\mathcal{U} \subset \mathbb{R}^{\mathbf{c}}$ , i.e.,

$\boldsymbol{\rho} : \mathbb{R}^+ \rightarrow \mathcal{U}$ . In the mechanical system described in (3.2), the uncertainties appear in the form of addition of uncertain terms  $\Delta\hat{M} : \hat{Q} \times \mathcal{U} \rightarrow \mathbb{R}^{\hat{n} \times \hat{n}}$ ,  $\Delta\hat{C} : T\hat{Q} \times \mathcal{U} \rightarrow \mathbb{R}^{\hat{n} \times \hat{n}}$ , and  $\Delta\hat{\mathbf{g}} : \hat{Q} \times \mathcal{U} \rightarrow \mathbb{R}^{\hat{n}}$  to the mass matrix, Coriolis matrix, and the vector of potential forces, respectively. I consider disturbance forces in the following form

$$\hat{\boldsymbol{\omega}} = \sum_1^w \hat{J}_{di} \hat{\boldsymbol{\omega}}_i, \quad (4.1)$$

where  $\hat{\boldsymbol{\omega}}_i$  are functions of time and  $\hat{J}_{di} : \hat{Q} \rightarrow \mathbb{R}^{\hat{n}}$  are the directions of disturbance forces. Accordingly, the uncertain state space representation of the system in (3.9) is

$$\dot{\mathbf{x}} = \mathbf{f}_u(\mathbf{x}) + G_u(\mathbf{x})\boldsymbol{\tau}, \quad (4.2)$$

where

$$\mathbf{f}_u(\mathbf{x}) = \begin{bmatrix} N\boldsymbol{\eta} \\ -(M_r + \Delta M_r)^{-1}((C_r + \Delta C_r)\boldsymbol{\eta} + (\mathbf{g}_r + \Delta\mathbf{g}_r) - \boldsymbol{\omega}_r) \end{bmatrix}, \quad (4.3)$$

$$G_u(\mathbf{x}) = \begin{bmatrix} \mathbb{O}_{n \times s} \\ (M_r + \Delta M_r)^{-1}B_r \end{bmatrix}, \quad (4.4)$$

and I have the terms

$$\Delta M_r := N^T J^T \Delta\hat{M} J N, \quad (4.5)$$

$$\Delta C_r := N^T J^T \Delta\hat{M} J \dot{N} + N^T (J^T \Delta\hat{M} \dot{J}) N + N^T J^T \Delta\hat{C} J N, \quad (4.6)$$

$$\Delta\mathbf{g}_r := N^T J^T \Delta\hat{\mathbf{g}}, \quad (4.7)$$

$$\boldsymbol{\omega}_r := N^T J^T \hat{\boldsymbol{\omega}}. \quad (4.8)$$

Let us separate the nominal dynamics from the terms involving uncertainties and disturbances in (4.2). Applying the partially linearizing feedback in (3.12) and the input-output linearization feedback in (3.23) to the system in (4.2) and substituting  $\boldsymbol{\eta}$  and  $\dot{\boldsymbol{\eta}}$  by

$$\begin{aligned} \boldsymbol{\eta} &= F^{-1}\dot{\mathbf{y}}, \\ \dot{\boldsymbol{\eta}} &= \sum_{j=1}^b \frac{\partial F_j^{-1}}{\partial \mathbf{q}} N F^{-1} \dot{\mathbf{y}} \dot{\mathbf{y}}_j + F^{-1} \ddot{\mathbf{y}}, \end{aligned} \quad (4.9)$$

the resultant uncertain closed loop input-output map becomes

$$\ddot{\mathbf{y}} = \Lambda(\mathbf{q}, \boldsymbol{\rho})^{-1}(\mathbf{u} + \boldsymbol{\sigma}(\mathbf{q}, \dot{\mathbf{q}}, \boldsymbol{\rho}, \dot{\mathbf{y}})). \quad (4.10)$$

Here,  $F_j^{-1}$  refers to the  $j^{\text{th}}$  column of the matrix  $F^{-1}$ ,  $\dot{\mathbf{y}}_j$  refers to the  $j^{\text{th}}$  component of output velocity and

$$\Lambda := \mathbb{I}_{\mathbf{b} \times \mathbf{b}} + FM_r^{-1}\Delta M_r F^{-1}, \quad (4.11)$$

$$\boldsymbol{\sigma} := FM_r^{-1}(-\Delta M_r \sum_{j=1}^b \frac{\partial F_j^{-1}}{\partial q} NF^{-1} \dot{\mathbf{y}} \dot{\mathbf{y}}_j - \Delta C_r F^{-1} \dot{\mathbf{y}} - \Delta \mathbf{g}_r + \boldsymbol{\omega}_r). \quad (4.12)$$

**Assumption 4.2.** I assume the following bound for the Frobenius norms  $FM_r^{-1}\Delta M_r F^{-1} < \epsilon_1$  where  $\epsilon_1$  is constant real numbers.

*Remark 4.1.* In this thesis, by the norm of a matrix or a vector I always mean the square Frobenius norm.

**Assumption 4.3.** In many applications of the developed theory, the dimension of the output  $\mathbf{b} = \mathbf{n} - \mathbf{m} = 2$ . Examples include different types of autonomous rovers, under water or aerial vehicles moving in a plane. Therefore, I assume  $\mathbf{b} = 2$  in the rest of the thesis. With some extra work, the analysis presented in this thesis may be extended to higher dimensional outputs.

**Assumption 4.4.** I assume  $\epsilon_1 < \frac{1}{1+\sqrt{2}}$ .

Consequently based on Assumption 4.3 and 4.4, the determinant of matrix  $\Lambda$  is always strictly positive. Hence, this matrix is always invertible and its diagonal elements are strictly positive. The state-space representation of the error-dynamics of the uncertain mapping in (4.10) becomes:

$$\ddot{\mathbf{e}} = \Lambda(\mathbf{q}, \boldsymbol{\rho})^{-1}(\mathbf{v} + \boldsymbol{\sigma}_e(\mathbf{q}, \boldsymbol{\rho}, \dot{\mathbf{e}}, t)), \quad (4.13)$$

where  $\mathbf{e} = \mathbf{y} - \mathbf{y}_d$ , and  $\boldsymbol{\sigma}_e = \boldsymbol{\sigma} + (\mathbb{I} - \Lambda)\ddot{\mathbf{y}}_d$ .

**Assumption 4.5.**  $\boldsymbol{\sigma}_e < \epsilon_2$ , where  $\epsilon_2$  is a constant real number.

Sliding mode control as a variable structure control method can be applied to the system in (4.13) to stabilize the tracking error of the output, which guarantees robustness against bounded uncertainties. The design of SMC is performed in two

steps: (i) designing the sliding manifold on which error becomes asymptotically stable towards the origin, (ii) designing a switching control law pushing a system outside of the sliding manifold towards it. Accordingly, the control law designed based on SMC consists of an equivalent control input denoted by the 2-dimensional vector  $\mathbf{v}_{eq}$  associated with the motion on the sliding manifold, and a switching control law denoted by the 2-dimensional vector  $\mathbf{v}_s$ , i.e.,

$$\mathbf{v} = \mathbf{v}_{eq} + \mathbf{v}_s. \quad (4.14)$$

### 4.3 Optimal Sliding Manifold Design

The sliding manifold determines the convergence behaviour of the output error to zero, when the system operates in nominal conditions (with no uncertainties and disturbances). Considering the nominal linearized input-output map in (3.24) along with an integral action to eliminate steady state error and improve robustness, the state space representation of the error dynamics becomes :

$$\dot{\mathbf{y}}_e = A_c^3 \mathbf{y}_e + B_c^3 \mathbf{v}_{eq}, \quad (4.15)$$

where

$$\mathbf{y}_e := \left[ \left( \int_0^t \mathbf{e}^T(\tau) d\tau \right) \mathbf{e}^T \dot{\mathbf{e}}^T \right]^T \in \mathbb{R}^6,$$

and  $A_c^3 \in \mathbb{R}^{6 \times 6}$  and  $B_c^3 \in \mathbb{R}^{6 \times 2}$  are the constant matrices representing the canonical form of a chain of three integrators. Note.  $\tau$  denotes a dummy time.

*Problem 4.1* (LQR Control Problem). In system (4.15) find the control input  $\mathbf{v}_{eq}(t)$  to asymptotically stabilize the origin for  $\mathbf{y}_e$ , while reaching the origin in a pre-specified finite time  $t_f$  and minimizing the following performance measure functional,

$$\Pi(\mathbf{v}_{eq}(t), \mathbf{e}(t)) = \frac{1}{2} \int_0^{t_f} (\mathbf{v}_{eq}^T K_v \mathbf{v}_{eq} + \mathbf{e}^T K_e \mathbf{e}) dt, \quad (4.16)$$

where  $K_v$  and  $K_e$  are both  $2 \times 2$  positive definite diagonal weighting matrices.

The solution can be found based on the variational principle. I first form the Hamiltonian function  $\mathcal{H}$  as :

$$\mathcal{H}(\mathbf{v}_{eq}, \mathbf{y}_e, \mathbf{p}) = \mathbf{v}_{eq}^T K_v \mathbf{v}_{eq} + \mathbf{e}^T K_e \mathbf{e} + \mathbf{p}^T \dot{\mathbf{y}}_e(\mathbf{v}_{eq}, \mathbf{y}_e), \quad (4.17)$$

where the 6-dimensional vector  $\mathbf{p}$  is a vector of Lagrange multipliers, i.e., co-states, and the functionality of  $\dot{\mathbf{y}}_e$  is in (4.15). The necessary conditions for the optimal trajectory and the optimal control input beside the constraint coming from the error dynamics in (4.15) are [95]:

$$\dot{\mathbf{p}}^* = -\frac{\partial \mathcal{H}}{\partial \mathbf{y}_e}(\mathbf{y}_e^*, \mathbf{v}_{eq}^*, \mathbf{p}^*), \quad (4.18)$$

$$0 = \frac{\partial \mathcal{H}}{\partial \mathbf{v}_{eq}}(\mathbf{y}_e^*, \mathbf{v}_{eq}^*, \mathbf{p}^*) \Rightarrow \mathbf{v}_{eq}^* = -K_v^{-1} \begin{bmatrix} \mathbb{O}_{2 \times 4} & \mathbb{I}_{2 \times 2} \end{bmatrix} \mathbf{p}^*, \quad (4.19)$$

where the superscript asterisk refers to the optimal curves. Substituting  $\mathbf{v}_{eq}^*$  in (4.15) and (4.18), the 12 number of linear first order ordinary differential equations known as the reduced state co-state equations become:

$$\dot{\mathbf{x}}_{ep}^* = A_L \mathbf{x}_{ep}^*, \quad (4.20)$$

where the 12-dimensional vector  $\mathbf{x}_{ep}^* = [(\mathbf{y}_e^*)^T, (\mathbf{p}^*)^T]^T$  and  $A_L \in \mathbb{R}^{12 \times 12}$  is a constant matrix (see Appendix B). The solution of this equation is

$$\mathbf{x}_{ep}^* = B_L(t) \mathbf{x}_{ep}^*(t_0) \quad (4.21)$$

where  $B_L = \exp(A_L t)$  is the state transition matrix.

Let  $B_{Lf} = B_L(t_f)$ , which can be partitioned as

$$B_{Lf} = \begin{bmatrix} B_{Lf1,1} & B_{Lf1,2} \\ B_{Lf2,1} & B_{Lf2,2} \end{bmatrix}, \quad (4.22)$$

where  $B_{Lfi,j} \in \mathbb{R}^{6 \times 6}$  ( $i, j = 1, 2$ ). Considering the split boundary value conditions  $\mathbf{y}_e^*(t_f) = 0$  and  $\mathbf{y}_e^*(0) = \mathbf{y}_e$ , the optimal control input  $\mathbf{v}_{eq}^*$  is obtained in the form of a PID controller. I set the equivalent control input  $\mathbf{v}_{eq}$  as

$$\mathbf{v}_{eq} = \mathbf{v}_{eq}^* = - \begin{bmatrix} K_I^* & K_p^* & K_d^* \end{bmatrix} \mathbf{y}_e, \quad (4.23)$$

where the matrix of optimal gains is:

$$\begin{bmatrix} K_I^* & K_p^* & K_d^* \end{bmatrix} = -K_v^{-1} \begin{bmatrix} \mathbb{O}_{2 \times 4} & \mathbb{I}_{2 \times 2} \end{bmatrix} B_{Lf12}^{-1} B_{Lf11}. \quad (4.24)$$

The matrix  $B_{Lf12}$  based on the structure of matrix  $A_L$  is invertible (see Appendix B). The obtained control law in (4.23) results in the convergence of the error on the following manifold

$$\ddot{\mathbf{e}} + K_d^* \dot{\mathbf{e}} + K_p^* \mathbf{e} + K_I^* \int_0^t \mathbf{e}(\tau) d\tau = 0. \quad (4.25)$$

Integrating this manifold, the following 2-dimensional relative degree one sliding manifold  $\mathbf{s}$  is designed:

$$\mathbf{s} = \dot{\mathbf{e}} + K_d^* \mathbf{e} + K_p^* \int_0^t \mathbf{e}(\tau) d\tau + K_I^* \int_0^t \left( \int_0^\tau \mathbf{e}(\tau_1) d\tau_1 \right) d\tau = 0. \quad (4.26)$$

## 4.4 Switching Control Law

After designing an optimal sliding manifold, the switching control law  $\mathbf{v}_s$  is obtained based on the uncertain error dynamics in (4.13), such that the sliding manifold  $\mathbf{s} = 0$  is attractive in finite time. Let us define the function  $\alpha(\mathbf{y}_e)$  and the constant  $k_0$  as

$$\alpha(\mathbf{y}_e) := \frac{(\sqrt{2} + \epsilon_1)(\mathbf{v}_{eq} + \epsilon_2) + \mathbf{v}_{eq}}{1 - \epsilon_1}, \quad (4.27)$$

$$k_0 := \frac{\epsilon_1}{1 - \epsilon_1}. \quad (4.28)$$

**Theorem 4.1.** *For any function  $\beta$  satisfying the condition*

$$\beta(\mathbf{y}_e) \geq \frac{\alpha}{1 - \sqrt{2}k_0} + \beta_0, \quad (4.29)$$

where  $\beta_0$  is a strictly positive arbitrary constant, the switching control law,

$$\mathbf{v}_{si} = -\beta \operatorname{sgn}(\mathbf{s}_i) \quad (4.30)$$

makes the system in (4.10) asymptotically stable towards the optimal sliding manifold in (4.26) as long as  $FM_r^{-1} \Delta M_r F^{-1} < \epsilon_1 < \frac{1}{1 + \sqrt{2}}$  and  $\sigma_e < \epsilon_2$ .

*Proof.* Prior to providing the stability proof of the proposed switching control law,

let us remind some important properties of the matrix  $\Lambda$ . Based on Assumption 4.3, 4.2, and 4.4, I have:

- (i) Due to triangle inequality,  $\sqrt{2} - \epsilon_1 < \Lambda < \sqrt{2} + \epsilon_1$
- (ii) Decomposing  $\Lambda$  into matrices of its diagonal elements  $\Lambda_d$  and its off-diagonal elements  $\Lambda_o$ , i.e.,  $\Lambda = \Lambda_d + \Lambda_o$ , it can be deduced that  $\Lambda_o < \epsilon_1$ , and the diagonal elements of  $\Lambda_d$  are strictly positive.
- (iii) The determinant of  $\Lambda$  is strictly positive.
- (iv) Since  $\Lambda$  is two by two,  $\Lambda^{-1} = \frac{\Lambda}{\det(\Lambda)}$ .
- (v) The matrix  $\Lambda^{-1}$  can be also decomposed into the matrices of its diagonal elements  $\Lambda_d^{-1}$  and its off-diagonal elements  $\Lambda_o^{-1}$ , i.e.,  $\Lambda^{-1} = \Lambda_d^{-1} + \Lambda_o^{-1}$ . Since  $\Lambda$  is two by two, it can be deduced that  $\Lambda_o^{-1} = \frac{\Lambda_o}{\det(\Lambda)}$  and  $\Lambda_d^{-1} = \frac{\Lambda_d}{\det(\Lambda)}$ .

For stability proof, I consider the following positive definite function as a Lyapunov candidate

$$V(\mathbf{s}) = \frac{1}{2} \mathbf{s}^T \mathbf{s}. \quad (4.31)$$

The time derivative of  $V$  is

$$\dot{V} = \mathbf{s}^T \dot{\mathbf{s}} = \mathbf{s}^T [\Lambda^{-1}(\mathbf{v}_s + \mathbf{v}_{eq} + \boldsymbol{\sigma}_e) + \mathbf{v}_{eq}], \quad (4.32)$$

using the definition of the sliding surface in (4.26) and  $\mathbf{v}_{eq}$  in (4.23), and the uncertain error dynamics in (4.13). I write  $\dot{V} = \dot{V}_1 + \dot{V}_2$ , where  $\dot{V}_i = \mathbf{s}_i \dot{\mathbf{s}}_i$ , for  $i = 1, 2$ . Decomposing the matrix  $\Lambda^{-1}$  into the matrices of its diagonal elements  $\Lambda_d^{-1}$  and its off-diagonal elements  $\Lambda_o^{-1}$ , (4.32) becomes:

$$\dot{V} = \mathbf{s}^T \Lambda_d^{-1} \mathbf{v}_s + \mathbf{s}^T \Lambda_o^{-1} \mathbf{v}_s + \mathbf{s}^T [\Lambda^{-1}(\mathbf{v}_{eq} + \boldsymbol{\sigma}_e) + \mathbf{v}_{eq}]. \quad (4.33)$$

Hence,

$$\dot{V}_i \leq \mathbf{s}_i \Lambda_{di}^{-1} \mathbf{v}_{si} + \mathbf{s}_i (\Lambda_o^{-1} \mathbf{v}_s + \Lambda^{-1}(\mathbf{v}_{eq} + \boldsymbol{\sigma}_e) + \mathbf{v}_{eq}), \quad (4.34)$$

where  $\Lambda_{di}^{-1}$  refers to the  $i^{th}$  diagonal element of matrix  $\Lambda_d^{-1}$ , and  $\mathbf{s}_i$  denotes the  $i^{th}$  component of vector  $\mathbf{s}$ . Since  $\Lambda_{di}^{-1}$  is a positive number,

$$\frac{\dot{V}_i}{\Lambda_{di}^{-1}} \leq \mathbf{s}_i \mathbf{v}_{si} + \mathbf{s}_i \frac{\Lambda_o^{-1} \mathbf{v}_s}{\Lambda_{di}^{-1}} + \mathbf{s}_i \frac{\Lambda^{-1}(\mathbf{v}_{eq} + \boldsymbol{\sigma}) + \mathbf{v}_{eq}}{\Lambda_{di}^{-1}}. \quad (4.35)$$

Considering the norm inequality for a diagonal element of  $\Lambda$ , i.e.,  $1 - \epsilon_1 < \Lambda_{di}$ , and based on property (v) for the matrix  $\Lambda$ , an upper bound for the right hand side of (4.35) is obtained by substituting a lower bound of the denominators.

$$\begin{aligned} \frac{\dot{V}_i}{\Lambda_{di}^{-1}} &\leq \mathbf{s}_i \mathbf{v}_{si} + \mathbf{s}_i \frac{\det(\Lambda) \Lambda_o^{-1} \mathbf{v}_s}{1 - \epsilon_1} + \mathbf{s}_i \frac{\det(\Lambda) \Lambda^{-1} (\mathbf{v}_{eq} + \boldsymbol{\sigma}) + \mathbf{v}_{eq}}{1 - \epsilon_1} \\ &= \mathbf{s}_i \mathbf{v}_{si} + \mathbf{s}_i \frac{\Lambda_o \mathbf{v}_s}{1 - \epsilon_1} + \mathbf{s}_i \frac{\Lambda (\mathbf{v}_{eq} + \boldsymbol{\sigma}) + \mathbf{v}_{eq}}{1 - \epsilon_1}. \end{aligned} \quad (4.36)$$

Based on properties (i) and (ii) for the matrix  $\Lambda$  and Assumption 4.4, an upper bound for the right hand side of (4.36) is obtained by substituting the upper bounds of the nominators. According to (4.27) and (4.28) I have

$$\frac{\dot{V}_i}{\Lambda_{di}^{-1}} \leq \mathbf{s}_i \mathbf{v}_{si} + \mathbf{s}_i \frac{\epsilon_1 \mathbf{v}_s}{1 - \epsilon_1} + \mathbf{s}_i \frac{(\sqrt{2} + \epsilon_1) (\mathbf{v}_{eq} + \epsilon_2) + \mathbf{v}_{eq}}{1 - \epsilon_1} = \mathbf{s}_i \mathbf{v}_{si} + \mathbf{s}_i (\alpha + k_0 \mathbf{v}_s). \quad (4.37)$$

Substituting  $\mathbf{v}_{si}$  from (4.30) and considering the fact that  $\mathbf{v}_s \leq \sqrt{2}\beta$ , I obtain

$$\frac{\dot{V}_i}{\Lambda_{di}^{-1}} \leq -\beta \mathbf{s}_i \text{sgn}(\mathbf{s}_i) + \mathbf{s}_i (\alpha + \sqrt{2} k_0 \beta) = \mathbf{s}_i (\alpha - \beta (1 - \sqrt{2} k_0)).$$

Since based on Assumption 4.4,  $1 - \sqrt{2} k_0 > 0$ , it can be deduced from (4.29) that  $-\beta (1 - \sqrt{2} k_0) \leq -\alpha - \beta_0 (1 - \sqrt{2} k_0)$ . Hence,

$$\frac{\dot{V}_i}{\Lambda_{di,i}^{-1}} \leq -\mathbf{s}_i (\beta_0 (1 - \sqrt{2} k_0)) < 0. \quad (4.38)$$

Since  $\dot{V} = \dot{V}_1 + \dot{V}_2$ , the inequality in (4.38) guarantees that  $\dot{V}$  is negative definite under the assumptions of the theorem and the closed-loop system is stable towards the sliding manifold  $\mathbf{s} = 0$ . ■

To alleviate the chattering effects, the sign function in the switching control law (4.30) can be approximated by a high-slope continuous saturation function

$$\mathbf{v}_{si} = -\beta (\mathbf{y}_e) \text{sat}\left(\frac{\mathbf{s}_i}{\kappa}\right), \quad (4.39)$$

where for a constant  $0 < \kappa \ll 1$

$$\text{sat}\left(\frac{\mathbf{s}_i}{\kappa}\right) := \begin{cases} -1 & \mathbf{s}_i \leq -\kappa \\ \frac{\mathbf{s}_i}{\kappa} & -\kappa < \mathbf{s}_i < \kappa \\ +1 & \mathbf{s}_i \geq \kappa \end{cases}$$

Based on the switching control law in (4.39), the two components of the Lyapunov function  $V$ , i.e.,  $V_1$  and  $V_2$ , satisfy the following inequality instead of (4.37):

$$\frac{\dot{V}_i}{\Lambda_{di}^{-1}} \leq -\beta \mathbf{s}_i \text{sat}\left(\frac{\mathbf{s}_i}{\kappa}\right) + \mathbf{s}_i(\alpha + k_0 \mathbf{v}_s). \quad (4.40)$$

Clearly in the region where  $\mathbf{s}_i \geq \kappa$  (for  $i = 1, 2$ ), the inequality (4.38) still holds; and hence the system in (4.10) reaches the boundary layer  $\mathbf{s}_i \leq \kappa$  (for  $i = 1, 2$ ) around the optimal sliding manifold (4.26) in finite time and remains inside thereafter.

*Remark 4.2.* Inside of the boundary layer  $\mathbf{s}_i \leq \kappa$  (for  $i = 1, 2$ ) around the optimal sliding manifold, the vector  $\mathbf{y}_e$  is bounded and reaches a positively invariant set in finite time. This leads to tracking with a guaranteed precision which can be arbitrarily adjusted by choosing  $\kappa$  [24, 96].

The block diagram of the proposed control strategy is depicted in Fig. 4.1, where the vectors  $\mathbf{q}_m$  and  $\dot{\mathbf{q}}_m$  are the set of measurable generalized coordinates and velocities. The states and the outputs of the system that are not measurable can be computed using the inverse differential kinematics relationship in (3.6) based on the nonholonomic constraints and the kinematics equations in (3.17) and (3.18), respectively.

*Remark 4.3.* If  $\mathfrak{s} > \mathfrak{n} - \mathfrak{m}$ , i.e., if the system contains redundant control directions, the matrix  $B_r$  in (3.12) is not a square invertible matrix. Accordingly, specifying the vector of control inputs  $\boldsymbol{\mu}$  to accomplish a control task does not result in a unique solution for the control inputs  $\boldsymbol{\tau}$  in (3.8). In this thesis, the right pseudo-inverse algorithm is employed to find a solution for  $\boldsymbol{\tau}$  that minimizes the quadratic norm of the control actions.

*Remark 4.4.* If the system starts its motion with an initial error, it might be far from the optimal sliding manifold in (4.26). This can result in producing large amounts of

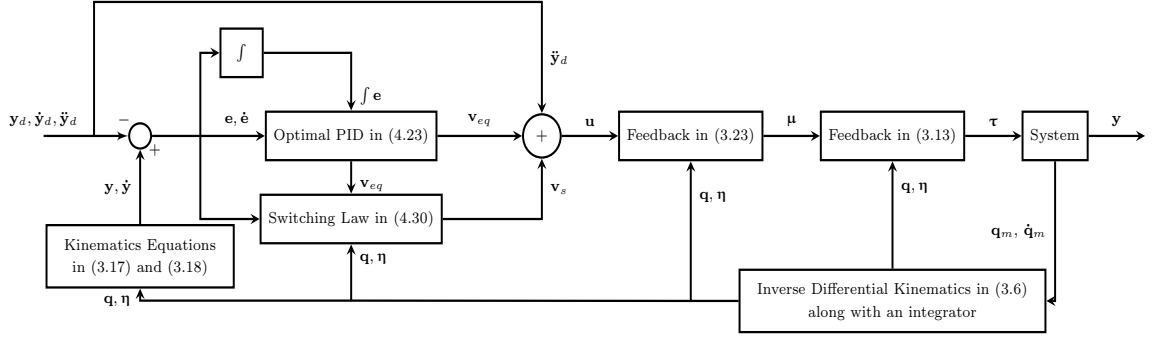


Figure 4.1: Optimal output-tracking sliding mode control block diagram

control actions by the proposed switching control law at the beginning of the motion. This drawback can be rectified by properly setting initial values for the integral or double integral terms in (4.26) in order for the system to start its motion on the sliding manifold.

## 4.5 Implementation on a Six-wheel Lunar Rover

For this case study, I consider the following uncertainties in the inertia parameters: (i) an unknown constant mass  $m_l$  with a bounded time-varying unknown moment of inertia about the  $z$ -axis (out of the plane of motion)  $I_{zl}(t)$  that moves with a bounded unknown time varying trajectory  $[x_l(t) \ y_l(t)]^T$  in the main body's  $xy$ -frame, (ii) an unbalanced port center wheel modeled as an unknown bounded time-varying added  $m_u$  to the wheel at an unknown constant radius  $R_u$ . In terms of disturbances, I consider an unknown bounded time-varying friction force with the magnitude of  $-\omega_r \text{sgn}(\dot{\theta})$  that is applied on the rear wheels in the lateral direction. Accordingly, the vector of uncertain parameters  $\boldsymbol{\rho}$  is formed as:

$$\boldsymbol{\rho}(t) = \begin{bmatrix} m_l & x_l & y_l & I_{zl} & m_u & R_u & \omega_r \end{bmatrix}^T. \quad (4.41)$$

As the result, the non-zero elements of the matrix  $\Delta\hat{M}(\theta, \psi_1, \boldsymbol{\rho})$  are

$$\begin{aligned}
\Delta\hat{M}_{1,1} &= \Delta\hat{M}_{2,2} = m_l + m_u \\
\Delta\hat{M}_{1,3} &= \Delta\hat{M}_{3,1} = -m_l x_l \sin(\theta) - (cm_u + m_l y_l) \cos(\theta) \\
\Delta\hat{M}_{1,6} &= \Delta\hat{M}_{6,1} = -m_u R_u \sin(\psi_1) \\
\Delta\hat{M}_{2,3} &= \Delta\hat{M}_{3,2} = m_l x_l \cos(\theta) - (cm_u + m_l y_l) \sin(\theta) \\
\Delta\hat{M}_{3,3} &= I_{zl} + c^2 m_u + m_l (x_l^2 + y_l^2) \\
\Delta\hat{M}_{3,6} &= \Delta\hat{M}_{6,3} = cm_u R_u \cos(\theta) \sin(\psi_1) \\
\Delta\hat{M}_{6,6} &= m_u R_u^2.
\end{aligned} \tag{4.42}$$

The matrix  $\Delta\hat{C}(\theta, \psi_1, \boldsymbol{\rho}, \dot{\boldsymbol{\rho}}, \dot{\mathbf{q}})$  is then obtained as

$$\Delta\hat{C} = \frac{\partial\Delta\hat{M}}{\partial\theta} \dot{\theta} + \frac{\partial\Delta\hat{M}}{\partial\psi_1} \dot{\psi}_1 + \sum_{i=1}^7 \frac{\partial\Delta\hat{M}}{\partial\boldsymbol{\rho}_i} \dot{\boldsymbol{\rho}}_i + \begin{bmatrix} \mathbb{O}_{2 \times 11} \\ \dot{\mathbf{q}}^T \frac{\partial\Delta\hat{M}}{\partial\theta} \\ \mathbb{O}_{2 \times 11} \\ \dot{\mathbf{q}}^T \frac{\partial\Delta\hat{M}}{\partial\psi_1} \\ \mathbb{O}_{5 \times 11} \end{bmatrix}, \tag{4.43}$$

where  $\boldsymbol{\rho}_i$  refers to the  $i^{th}$  element of  $\boldsymbol{\rho}$ . The vector of uncertain potential forces  $\Delta\hat{\mathbf{g}}$  due to the unbalanced wheel is

$$\Delta\hat{\mathbf{g}} = \begin{bmatrix} \mathbb{O}_{5 \times 1} \\ -m_u g_u R_u \cos(\psi_1) \\ \mathbb{O}_{5 \times 1} \end{bmatrix}, \tag{4.44}$$

where  $g_u$  denotes the gravitational constant. Finally, the direction of the friction disturbance force is determined to be

$$\hat{J}_d = \begin{bmatrix} -\sin(\theta) & \cos(\theta) & -L_0 & \mathbb{O}_{1 \times 8} \end{bmatrix}. \tag{4.45}$$

Subsequent to determining the uncertain matrices  $\Delta\hat{M}$  and  $\Delta\hat{C}$ , the vector  $\Delta\hat{\mathbf{g}}$ , and the row vector  $\hat{J}_d$ , the uncertain state-space representation in (4.2) can be formed

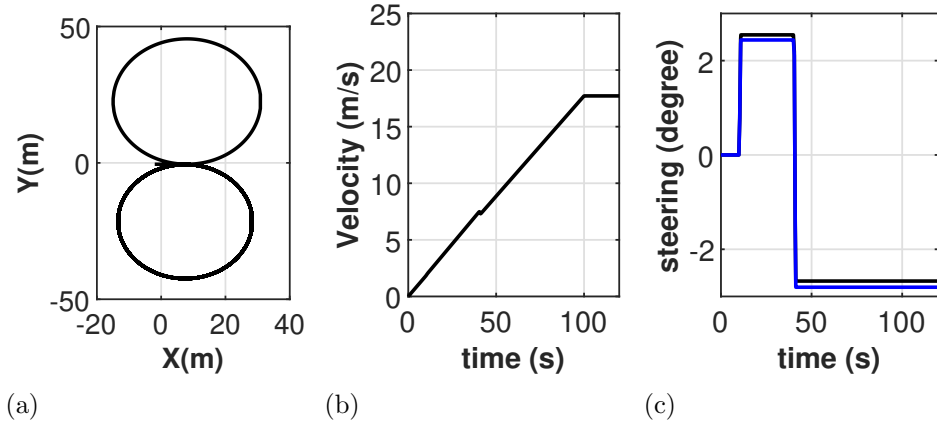


Figure 4.2: Desired trajectory for the rover: (a) desired path (b) desired forward velocity of the rover (c) desired steering angles of port (black line) and starboard (blue line) front wheels

for the Lunar autonomous rover and the proposed robust optimal output-tracking control law can be implemented.

#### 4.5.1 Simulation Results

The Lunar autonomous rover system along with the proposed controller is modeled in MATLAB R2019b. Table 4.1 depicts the values of the parameters used in the model of the system, modeled uncertainties, and the controller. A desired trajectory for the rover is considered that includes an acceleration from zero velocities with  $0.18\text{m/s}^2$  in the forward direction of motion for 100s and two steering commands at 10s and 40s. The desired initial value for the vector of generalized coordinates  $\hat{\mathbf{q}}$  is set to be

$$\hat{\mathbf{q}}_d(0) = \begin{bmatrix} -L - l & -c & \mathbb{O}_{1 \times 9} \end{bmatrix}^T,$$

such that the initial value of the desired output trajectory is zero. Following this desired trajectory, the origin of the  $xy$ -frame moves on a figure-eight path while it is continuously accelerating (see Fig. 4.2). Based on (3.46) the desired trajectory for the output is determined. Note that the designed trajectory has large velocities to highlight the effect of uncertainties at the output.

According to the weighting matrices  $K_v$  and  $K_e$  and the convergence time  $t_f$

Rover Parameters			
$L[\text{m}]$	$L_0[\text{m}]$	$c[\text{m}]$	$R_w[\text{m}]$
1	0.5	0.5	0.3
$l[\text{m}]$	$x_{cm}[\text{m}]$	$y_{cm}[\text{m}]$	$m_r[\text{Kg}]$
1	0.25	0	600
$m_w[\text{Kg}]$	$J_r[\text{Kg/m}^2]$	$J_{wy}[\text{Kg/m}^2]$	$J_{wz}[\text{Kg/m}^2]$
40	450	1.3	1
Uncertain Parameters			
$m_l[\text{Kg}]$	$x_l[\text{m}]$	$\dot{x}_l[\text{m/s}]$	$y_l[\text{m}]$
250	$-0.5 \cos(t/3)$	$0.16 \sin(t/3)$	$0.3 \sin(t/3)$
$\dot{y}_l[\text{m/s}]$	$m_u[\text{Kg}]$	$\dot{m}_u[\text{Kg/s}]$	$R_u[\text{m}]$
$0.1 \cos(t/3)$	$0.1 - 0.025 \cos(5t)$	$0.125 \sin(5t)$	0.3
$I_{zl}[\text{Kg/m}^2]$	$\dot{I}_{zl}[\text{Kg/m}^2\text{s}]$	$\omega_r[\text{N}]$	$g_u[\text{m/s}^2]$
$75 - 20 \cos(t/2)$	$10 \sin(t/2)$	140	1.636
Control Parameters			
$K_v$	$K_e$	$t_f[\text{s}]$	$\epsilon_1$
$\mathbb{I}_{2 \times 2}$	$\mathbb{I}_{2 \times 2}$	10	0.31
$\epsilon_2$	$\kappa$	$\beta_0$	
1	0.55	0.0001	

Table 4.1: Kinematic and dynamic parameters of the Lunar rover, uncertain parameters defined in the simulation, and control parameters

reported in Table 4.1, the matrix of optimal gains in (4.26) is obtained as:

$$[K_I^* \ K_p^* \ K_d^*] = \begin{bmatrix} 0.14 & 0 & 1.19 & 0 & 1.55 & 0 \\ 0 & 0.14 & 0 & 1.19 & 0 & 1.55 \end{bmatrix}.$$

The function  $\beta$  in the switching control law (4.30) is selected using the equality condition in (4.29) to be

$$\beta(\mathbf{y}_e) = \frac{\alpha}{1 - \sqrt{2}k_0} + \beta_0, \quad (4.46)$$

where  $\alpha$  and  $k_0$  are defined in (4.27) and (4.28), respectively. I assume that the rover starts its motion with zero velocity, an initial error  $[0 \ 0.5]^T$  in the output, and at the configuration described by

$$\hat{\mathbf{q}}(0) = \begin{bmatrix} -L - l & -c + 0.5 & \mathbb{O}_{1 \times 9} \end{bmatrix}^T.$$

To start the motion of the system on the optimal sliding manifold, I introduce an initial value for the integral of the error, based on (4.26).

The simulation is once conducted only with the proposed optimal PID control law obtained in (4.23) as part of the output-tracking SMC design. The results corresponding to this simulation are labeled by ‘‘OPID’’. The same scenario is simulated using the optimal output-tracking SMC with both  $\mathbf{v}_{\text{eq}}$  in (4.23) and the switching control law in (4.39), whose results are labeled by ‘‘ORS’’. The errors in the trajectory tracking for the rover, the output and the steering angles are shown in Fig. 4.3. Further, the control torques at all wheels and the steering degrees of freedom are compared in Fig. 4.4.

Based on Fig. 4.3 in both control approaches, system is navigated from its initial location towards the desired trajectory and tracks it with an acceptable amount of error, caused by the imposed uncertainties and disturbances (maximum error almost equals to  $0.2m$  in OPID and  $0.02m$  in ORS for  $1.2km$  traveled distance). However, it is evident that adding the proposed switching control law improves the robustness of the controller and reduces the error by one order of magnitude (from near  $0.2m$  to near  $2cm$ ). Considering Fig. 4.3.c and Fig. 4.3.d, the output converges to its desired trajectory almost at the prescribed time of  $t_f = 10s$ , while according to Fig. 4.3.a and Fig. 4.3.b the rover reaches its prescribed trajectory slightly after

10s. In addition since the controllers were designed to regulate the system output, it is observed from Fig. 4.3 that the magnitude of the error in the rover motion is marginally more than that of the output, throughout the simulation. This difference is directly influenced by the location of the look-ahead point. The system particularly demonstrate non-minimum phase behaviour due to its nonholonomicity in the first 10s of its motion, where the controller attempts to zero the error in  $\mathbf{y}_2$  in the expense of introducing considerable errors in  $x_b$  and steering angles. It is also noted that the effects of uncertainties at the output are directly correlated with the amount of the rover acceleration and its velocity, due to the appearance of uncertainties in the mass matrix and the Coriolis and Centrifugal terms. This is the reason behind the observed increase in the error in Fig. 4.3 as the time elapses.

According to Fig. 4.4, the control actions produced by the ORS control scheme follow the same trend comparing with those obtained in the OPID case, with the addition of some chattering effects as the result of the proposed switching control law. The magnitude of the chattering can be adjusted by a proper choice of the variable  $\kappa$ . Generally, smaller  $\kappa$  results in smaller magnitude of errors but larger amplitude of chartering in control actions. Based on the adjusted variable for  $\kappa$  (see Table 4.1), the highest amplitude of chattering is observed to be near 5N.m. When the system moves with a constant velocity (after time 100s) on a circle since the center of mass is located ahead of the origin of the  $xy$ -frame, both controllers are producing time-varying brake forces to compensate for the Coriolis effects. The low-frequency oscillations (with large amplitude) in the produced control actions by both control laws during circling are due to the sinusoidal changes in the location of the center of mass of the system. Throughout the motion, the system also experiences high-frequency oscillations (with small amplitude) in the produced control torques as the result of the unbalanced port center wheel. The period of the high-frequency oscillations decreases as the velocity of the system increases.

## 4.6 Summary

In this chapter, the uncertain error dynamics of the output was introduced by applying the input-output linearization feedback transformation to the nominal plant. Accordingly, under the boundedness assumption of the uncertain terms, a robust

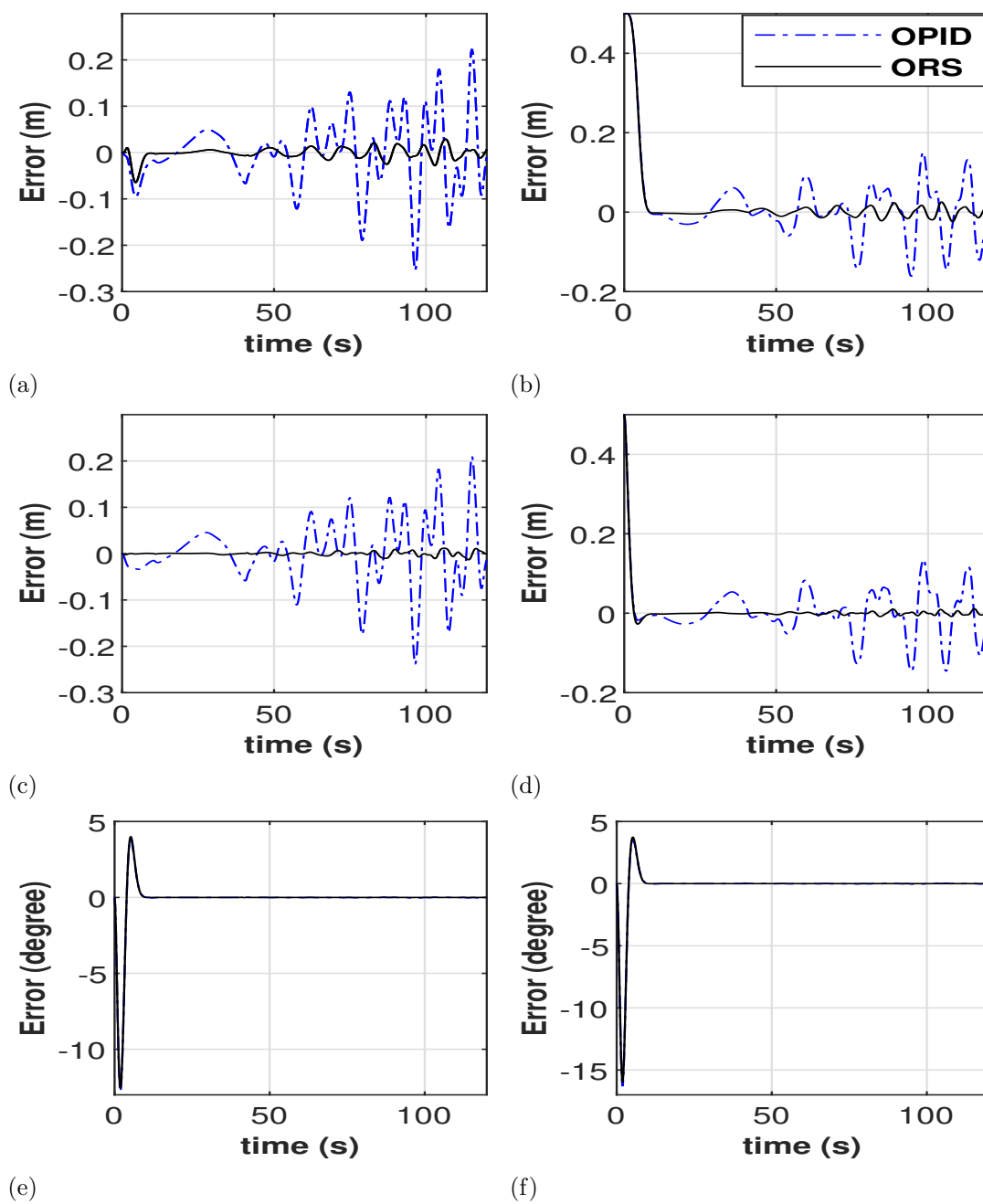


Figure 4.3: Performance comparison of OPID and ORS in terms of error in (a)  $x_b$ , (b)  $y_b$ , (c)  $y_1$ , (d)  $y_2$ , (e)  $\delta_p$ , and (f)  $\delta_s$

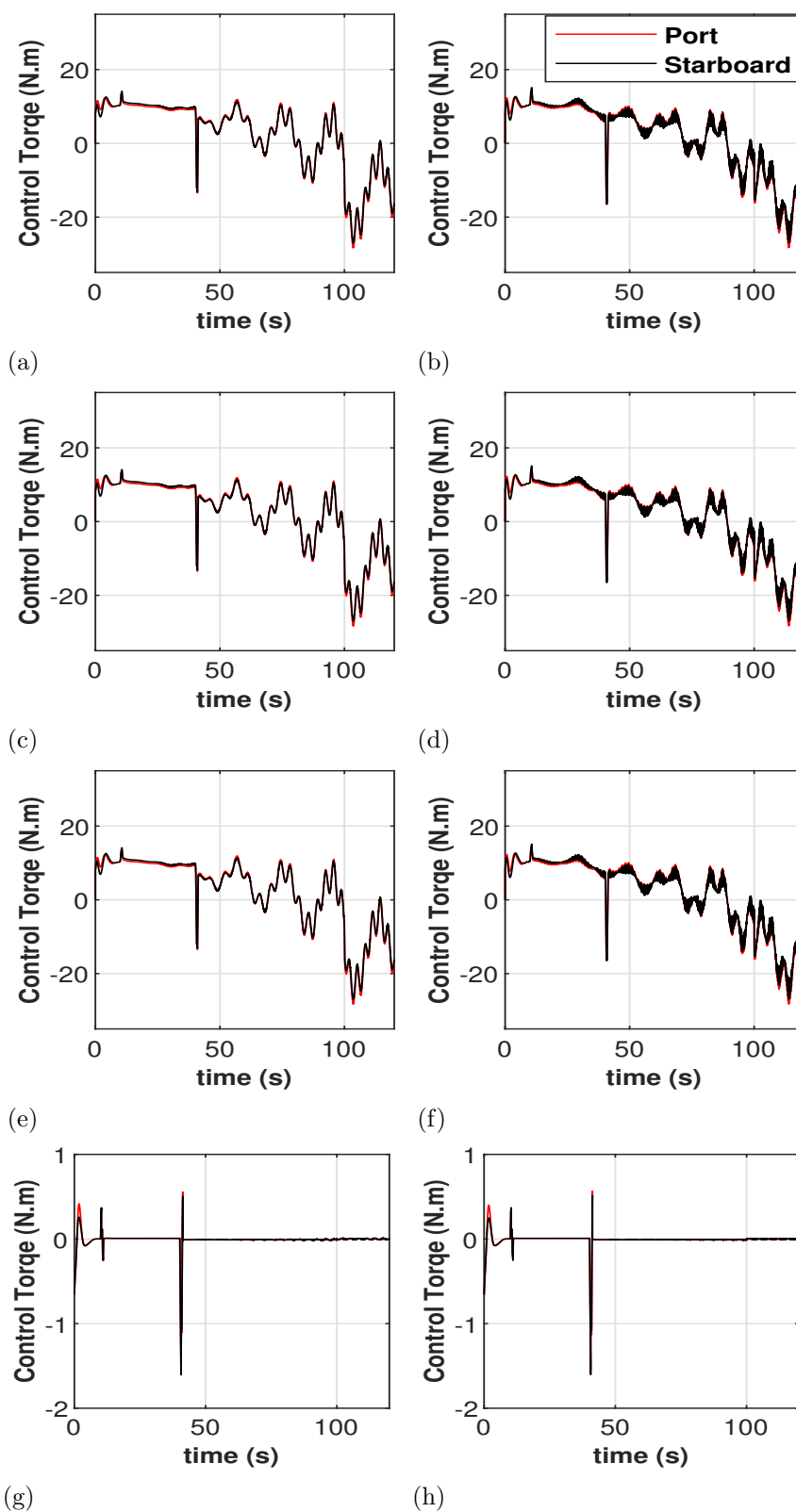


Figure 4.4: Comparison of control commands generated by OPID (left) and ORS (right) laws. From the top to the bottom row, the plots respectively correspond to torques at the front wheels, center wheels, rear wheels, and steering degrees of freedom.

output tracking control algorithm was proposed based on sliding mode control with an optimally designed sliding manifold. Stability of the system towards the sliding manifold was proved using Lyapunov's direct method. To alleviate the chattering effect, the method of boundary layer was implemented and the discontinuous switching control law was replaced by the continuous saturation function. The developed theory was implemented on a six-wheel autonomous Lunar rover and the efficacy of that was compared to a proposed optimal PID controller, in a simulation environment. It was shown that both control approaches were able to navigate the system from its initial location towards a desired trajectory and track it with an acceptable amount of error. However, the proposed robust control law reduced the error by one order of magnitude and demonstrated resilient behaviour. Further, the control actions in both control methods followed the same trend, but the robust control signals contained some chattering effects as the result of the proposed switching control law.

## Chapter 5

# Optimal Control Distribution and Traction Control

### 5.1 Overview

In Chapter 4, I improved the tracking performance by designing a robust optimal output-tracking control law. In this chapter, employing redundant control directions, an optimization algorithm is proposed to further enhance the system performance, without affecting the tracking performance. Then, the developed methodology is used to improve traction of autonomous rover/vehicle systems. Under some explained assumptions, the tractive and ground normal reaction forces are approximated. Such approximations are used in defining a cost function whose optimality results in maximizing traction. The proposed theory is implemented on the six-wheel type (1, 1) autonomous Lunar rover. Using a developed software-in-the-loop simulation environment, which includes a high-fidelity 3-dimensional model of the rover in Vortex Studio, the estimations of normal and tractive forces are validated. Additionally, the efficacy of the proposed dynamic traction controller is investigated using both MATLAB and Vortex simulation environments by comparing the results with the conventional right pseudo-inverse solution.

### 5.2 Optimal Control Distribution

In this section, I introduce the notion of optimal control distribution for the constrained mechanical systems considered in this thesis that are not kinematically redundant; however, they include redundant control directions. For such systems, the

variation of control input in the null directions not only does not affect the output dynamics, but it also leaves the internal dynamics unchanged. An optimization in these null directions may be implemented to improve force/moment interaction of the system with its environment. For autonomous rover/vehicle systems, this can result in a dynamic traction controller.

Let us consider a cost functional  $R$  for the closed-loop system defined by (3.9), (3.12), (3.23) and (4.14):

$$R(\mathbf{x}, \boldsymbol{\tau}, \mathbf{x}_d) = \int_0^{t_f} r(\mathbf{x}, \boldsymbol{\tau}, \mathbf{x}_d) d\tau, \quad (5.1)$$

which is optimized for a performance indicator  $r$  as the performance indicator and a given desired trajectory  $\mathbf{x}_d$  for the closed-loop system. Note.  $\tau$  denotes a dummy time. This optimization is formulated as follows:

$$\min_{\boldsymbol{\tau}(\cdot)} R(\mathbf{x}, \boldsymbol{\tau}, \mathbf{x}_d). \quad (5.2)$$

$$\text{subject to: (3.9), (3.12), (3.23), (4.14)} \quad (5.3)$$

Based on the variational principle, the necessary conditions of the optimality are obtained by

$$\delta R = \int_0^{t_f} \left( \frac{\partial r}{\partial \mathbf{x}} \delta \mathbf{x} + \frac{\partial r}{\partial \boldsymbol{\tau}} \delta \boldsymbol{\tau} + \frac{\partial r}{\partial \mathbf{x}_d} \delta \mathbf{x}_d \right) d\tau = 0, \quad (5.4)$$

$$\text{subject to: (3.9), (3.12), (3.23), (4.14)}$$

for an arbitrary variation of the system. Here,  $\delta$  means the variation of a curve. In this section, instead of formally appending the constraints to the performance indicator according to the Pontryagin's Maximum Principle, I simply reason the effects of the constraints on the variation of  $R$ .

Based on Assumption 3.1, system contains redundant control directions and the matrix  $B_r$  defined in (3.8) is not square. Hence, the lift from the right side of (3.12) to the space of actual control actions  $\boldsymbol{\tau}$  has infinite number of solutions. Let us decompose the vector of control actions

$$\boldsymbol{\tau} = \boldsymbol{\tau}_{\parallel} + \boldsymbol{\tau}_{\perp}. \quad (5.5)$$

Here,  $\boldsymbol{\tau}_{\perp}$  is the component of  $\boldsymbol{\tau}$  in  $\ker(B_r)$ , where  $\ker(\cdot)$  denotes the kernel of a matrix,

and it can be obtained by:

$$\boldsymbol{\tau}_\perp = W(\mathbf{q})\boldsymbol{\tau}_a, \quad (5.6)$$

where  $W(q) : Q \rightarrow \mathbb{R}^{s \times (s-b)}$  is a matrix whose columns span  $\ker(B_r)$  and  $\boldsymbol{\tau}_a \in \mathbb{R}^{s-b}$ . In addition,  $\boldsymbol{\tau}_\parallel$  is the component of  $\boldsymbol{\tau}$  orthogonal to  $\ker(B_r)$  and it is obtained by

$$\boldsymbol{\tau}_\parallel = B_r^T (B_r B_r^T)^{-1} \boldsymbol{\tau}_b, \quad (5.7)$$

for some  $\boldsymbol{\tau}_b \in \mathbb{R}^b$ . Therefore, the solutions of (3.12) take the following form:

$$\boldsymbol{\tau} = \boldsymbol{\tau}_\parallel + \boldsymbol{\tau}_\perp = B_r^T (B_r B_r^T)^{-1} \mathbf{u}_f + W(\mathbf{q})\boldsymbol{\tau}_a, \quad (5.8)$$

for an arbitrary  $\boldsymbol{\tau}_a$ , where  $\mathbf{u}_f := C_r \boldsymbol{\eta} + \mathbf{g}_r + M_r \boldsymbol{\mu}$  is the right hand side of (3.12). The solution of (3.12) in the orthogonal directions to  $\ker(B_r)$ , i.e., when  $\boldsymbol{\tau}_a = 0$ , is often known as the right pseudo-inverse.

As the desired and actual trajectories of the output are prescribed by the proposed control law in Chapter 4 and they are intended to be kept unchanged, and since the system is not kinematically redundant based on Assumption 3.3, the constraints in (5.4) can be translated into

$$\begin{aligned} \delta \mathbf{x}_d &= 0, \\ \delta \mathbf{x} &= 0, \\ \delta \boldsymbol{\tau}_\parallel &= 0. \end{aligned} \quad (5.9)$$

Hence, the necessary conditions in (5.4) converts into the following simple form:

$$\frac{\partial r}{\partial \boldsymbol{\tau}_a} = 0, \quad (5.10)$$

which is equivalent to minimizing  $r$ , assuming convexity of this function. Hereinafter,  $r$  is referred to as the cost function.

*Remark 5.1.* The orthogonal projection used in the determination of  $\boldsymbol{\tau}_\parallel$  minimizes the quadratic norm of  $\boldsymbol{\tau}$  and results in the uniform distribution of control actions in different control directions. If same actuators are used at all control directions, uniform distribution of the control actions means minimizing the dissipated energy in the system.

The block diagram of the proposed control algorithm along with the optimal distribution of control actions is depicted in Fig.5.1, where the vectors  $\mathbf{q}_m$  and  $\dot{\mathbf{q}}_m$

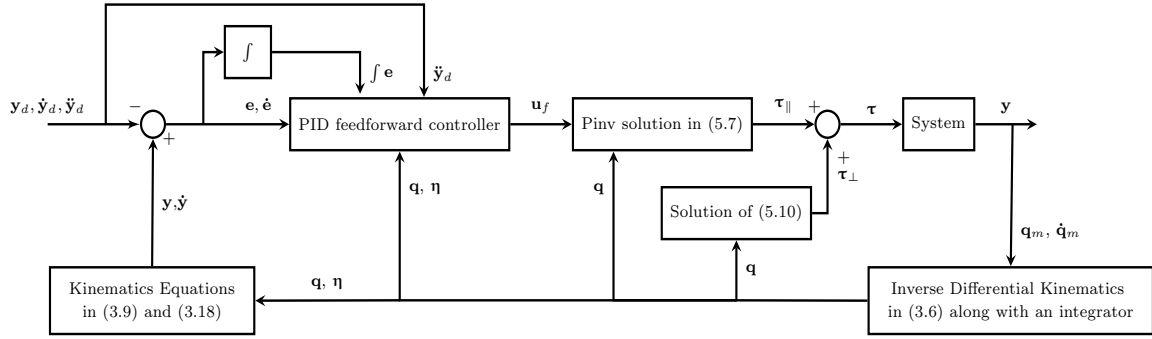


Figure 5.1: Control block diagram with optimal control distribution

are the set of measurable generalized coordinates and velocities. The states and the outputs of the system that are not measurable can be computed using the inverse differential kinematics relationship in (3.9), and the output equations in (3.17), and (3.18). For simplicity and emphasizing on the optimal control distribution, in this chapter, the error dynamics of the output is asymptotically stabilized only applying  $\mathbf{v}_{eq}$  using a PID controller, and it is assumed that system is not subject to any source of uncertainties.

### 5.3 Dynamic Traction Control

In this section, the introduced optimal control distribution in Section 5.2 is employed to improve the traction of planar autonomous rovers/vehicles by defining a proper cost function  $r$ . Such systems lose traction whenever the imposed zero-velocity constraints at wheel-ground contact points are violated. These constraints are satisfied by the virtue of continuously applying constraint forces, appearing as the vector of Lagrange multipliers in the dynamical equations. Since the wheel-ground contact points have zero velocity in the constrained directions, these constraint forces are indeed ground static frictions. Considering the Coulomb friction model, once at any contact point the ratio of such a force over the normal ground reaction force passes the static friction threshold, system experiences dynamic friction and violation of constraints. Therefore, to keep the system away from the verge of traction loss, the cost function  $r$  may be defined based on this ratio. In the following, I first calculate the tractive forces and then the normal forces, under the ideal nonholonomic assumption and

some technical conditions that hold for the majority of systems under investigation.

**Assumption 5.1.** I assume that the constraints not corresponded to zero velocity of wheel-ground contact points are all holonomic and integrated.

*Remark 5.2.* As shown in Section 3.2, the imposed constraints related to zero velocity condition of wheel-ground contact points may also result in holonomic constraints. However, since tractive forces at all wheels are required for traction optimization, I only integrate the holonomic constraints described in Assumption 5.1, and restrict the dynamics to the corresponding configuration manifold. This restriction does not affect the output-tracking control scheme presented in Chapter 4, which was derived by integrating all holonomic constraints.

Specifying the inclusion map  $\iota(\mathbf{q})$  and its Jacobian  $J(\mathbf{q})$ , and the matrix  $E$  in (3.4) for this restriction, the equations of motion of a planar vehicle is derived based on (3.6), where the magnitude of tractive forces are represented by the elements of the vector  $\boldsymbol{\lambda}$ . This vector can be determined by differentiating the constraint equations in (3.3) with respect to time and substituting  $\ddot{\mathbf{q}}$  by dynamical equations in (3.6).

$$\begin{aligned} 0 &= \frac{d}{dt}(A\dot{\mathbf{q}}) = A\ddot{\mathbf{q}} + \dot{A}\dot{\mathbf{q}}, \\ &\rightarrow AM^{-1}(-C\dot{\mathbf{q}} + B\boldsymbol{\tau} + A^T\boldsymbol{\lambda}) + \dot{A}\dot{\mathbf{q}} = 0, \end{aligned} \quad (5.11)$$

where

$$\dot{A}(\mathbf{q}, \dot{\mathbf{q}}) = \sum_{j=1}^n \frac{\partial A(\mathbf{q})}{\partial \mathbf{q}_j} \dot{\mathbf{q}}_j. \quad (5.12)$$

*Note.* Since the planar autonomous rovers/vehicles are considered,  $\mathbf{g} \equiv 0$  in (3.6).

From (5.11) it can be deduced that:

$$\boldsymbol{\lambda}(\mathbf{q}, \dot{\mathbf{q}}, \boldsymbol{\tau}) = -(AM^{-1}A^T)^{-1} \left( AM^{-1}(-C\dot{\mathbf{q}} + B\boldsymbol{\tau}) + \dot{A}\dot{\mathbf{q}} \right). \quad (5.13)$$

Since the matrix  $A$  is full rank and the mass matrix  $M$  is everywhere nonsingular,  $\boldsymbol{\lambda}$  can be uniquely determined from (5.13). I reformat (5.13) to achieve

$$\boldsymbol{\lambda} = V(\mathbf{q}, \dot{\mathbf{q}}) + D(\mathbf{q})\boldsymbol{\tau}, \quad (5.14)$$

where

$$\begin{aligned} V(\mathbf{q}, \dot{\mathbf{q}}) &:= -(AM^{-1}A^T)^{-1}(-AM^{-1}C\dot{\mathbf{q}} + \dot{A}\dot{\mathbf{q}}), \\ D(\mathbf{q}) &:= -(AM^{-1}A^T)^{-1}AM^{-1}B. \end{aligned}$$

**Assumption 5.2.** I assume that the system is always in quasi-static condition in the vertical (perpendicular to the plane of motion), roll, and pitch directions.

Let us denote the  $\mathbf{g}$ -dimensional vector of normal reaction forces at all wheels by  $\mathbf{n}$ . Considering the forces and moments transferred to the chassis and based on Assumption 5.2,  $\mathbf{n}$  can be generally formulated as:

$$\mathbf{n} = \mathbf{k}(\boldsymbol{\varsigma}, \boldsymbol{\epsilon}, g_u) + \Phi(\boldsymbol{\varsigma}, \boldsymbol{\epsilon}, \mathbf{q})\boldsymbol{\lambda} + \Pi(\boldsymbol{\varsigma}, \boldsymbol{\epsilon}, \mathbf{q})\boldsymbol{\tau}, \quad (5.15)$$

where  $\boldsymbol{\varsigma}$  is a vector of inertia and geometric parameters of the system,  $\boldsymbol{\epsilon}$  is a vector of elasticity constants at suspension springs exploited when the problem is underdetermined,  $g_u$  is the gravitational constant,  $\mathbf{k} \in \mathbb{R}^g$ ,  $\Phi \in \mathbb{R}^{g \times m}$ , and  $\Pi \in \mathbb{R}^{g \times 5}$ . Since the terms included in (5.15) are dependant on the structure of the system, they are discussed in more details in Section 5.4 for a specific autonomous rover system.

I define a vector  $\mathbf{n}' \in \mathbb{R}^m$  such that its  $i^{th}$  component corresponds to the normal reaction force at the wheel-ground contact point generating the  $i^{th}$  component of  $\boldsymbol{\lambda}$ . Let us introduce a matrix  $L_n : \mathbb{R}^g \rightarrow \mathbb{R}^m$  mapping the vector of normal reaction forces  $\mathbf{n}$  to the vector  $\mathbf{n}'$  i.e.,

$$\mathbf{n}' = L_n \mathbf{n}. \quad (5.16)$$

I also introduce a diagonal matrix  $\mathcal{U} \in \mathbb{R}^{m \times m}$  whose  $i^{th}$  diagonal element corresponds to the static friction coefficient related to the  $i^{th}$  component of  $\mathbf{n}'$ .

*Remark 5.3.* The vector  $\boldsymbol{\lambda}$  specified in (5.13) only includes the linearly independent constraint forces, and obtaining individual tractive forces at all wheels is infeasible in most applications. Additional information such as the amount of slippage, tire elasticity, or 3D dynamics of the system is required to solve this underdetermined problem.

**Assumption 5.3.** For simplicity, I assume uniform distribution of tractive forces among the involved wheels with linearly dependant constraint directions, as discussed in Remark 5.3. The average of normal reaction forces at the involved wheels is used in the definition of  $\mathbf{n}'$ . I also assume that such linear dependencies in the constraint directions only exist in the lateral tractive forces at the wheels.

This assumption is valid for the majority of autonomous rovers/vehicles including type (1, 1) and type (2, 0).

Now that the functionality of tractive forces and normal reaction forces are specified under the explained assumptions, they can be employed to define the cost function  $r$  with the aim of improving traction. For this purpose, a seemingly proper choice for  $r$  would be a quadratic norm of a vector containing the ratio of tractive forces over corresponding normal reaction forces by the inverse of static friction coefficients. Minimizing this norm results in uniform distribution of tractive ratios with respect to the static friction coefficients and maximizing traction [85–89]. However, this cost function makes the necessary condition of optimality in (5.10) nonlinear with respect to  $\boldsymbol{\tau}_a$  and numerical methods must be employed to solve for the optimal solution, impeding its real-time implementation in dynamic tasks. In addition, consideration of the magnitude of tractive forces without including their directions, as suggested by this cost function, fails to realistically improve the vehicles' traction on various trajectories. For example, if I consider lateral along with the longitudinal tractive forces when optimizing traction on a straight line, an unnecessary lateral tractive force distribution is produced that deteriorates the overall traction of the system.

To alleviate the shortcomings associated with the existing traction control systems, I develop a two-stage optimization algorithm that separately considers the lateral and longitudinal tractive forces with respect to the main body coordinate frame. Additionally, I propose the cost function  $r$  to be a quadratic norm of the difference between the tractive forces and their corresponding normal forces scaled by the static friction coefficients. This cost function is linear with respect to  $\boldsymbol{\tau}_a$  and its minimization reduces the quadratic norm of the vector of tractive ratios. To consider the sign of tractive forces in this cost function, I introduce the notion of required acceleration at the system's center of mass.

**Assumption 5.4.** I assume that the configuration manifold of the system is in the form of a trivial fiber bundle with fibers being isomorphic to a Lie group and control torques are only applied on the shape space of the system. The only external forces to the system resulting in the change of momentum are assumed to be the tractive forces [97]. I assume that the dynamical equation (3.6) is derived such that the first 3 rows (planar motion) correspond to the derivative of the total momentum of the system about the origin of the main body coordinate frame. Further, the system's center of mass is assumed fixed in the main body coordinate frame.

Under Assumption 5.4, I introduce the Jacobian  $J_c = \begin{bmatrix} \bar{J}_c(\mathbf{q}) & \mathbb{O}_{3 \times n-3} \end{bmatrix}$  such that  $\dot{\mathbf{y}}_c = J_c \dot{\mathbf{q}}$  where  $\mathbf{y}_c \in \mathbb{R}^3$  is the location of the system's center of mass in the inertial coordinate frame expressed in the main body coordinate frame. Pre-multiplying both sides of (3.6) by the matrix  $J_c^T$ , I have

$$J_c^T M \ddot{\mathbf{q}} + J_c^T C \dot{\mathbf{q}} = J_c^T B \boldsymbol{\tau} + J_c^T A^T \boldsymbol{\lambda}. \quad (5.17)$$

Based on Assumption 5.4,  $J_c^T B \boldsymbol{\tau} = \mathbb{O}_{3 \times 1}$  and it can be eliminated from (5.17). In addition, I can replace  $\ddot{\mathbf{q}}$  in (5.17) by

$$\ddot{\mathbf{q}} = \dot{N} \dot{\boldsymbol{\eta}} + N \ddot{\boldsymbol{\eta}}. \quad (5.18)$$

Accordingly (5.17) becomes

$$J_c^T M (\dot{N} \dot{\boldsymbol{\eta}} + N \ddot{\boldsymbol{\eta}}) + J_c^T C \dot{\mathbf{q}} = J_c^T A^T \boldsymbol{\lambda}. \quad (5.19)$$

Based on (3.13), it can be deduced that  $\dot{\boldsymbol{\eta}} = \boldsymbol{\mu}$  where  $\boldsymbol{\mu}$  is determined based on the designed control input  $\mathbf{u}$  through (3.24). Additionally, based on (3.12), the relationship between  $\boldsymbol{\mu}$  and  $\boldsymbol{\tau}$  is

$$\boldsymbol{\mu} = M_r^{-1} (B_r \boldsymbol{\tau} - C_r \boldsymbol{\eta}). \quad (5.20)$$

Substituting  $\dot{\boldsymbol{\eta}}$  in (5.19) by (5.20)

$$J_c^T M (\dot{N} \boldsymbol{\mu} + N M_r^{-1} (B_r \boldsymbol{\tau} - C_r \boldsymbol{\eta})) + J_c^T C \dot{\mathbf{q}} = J_c^T A^T \boldsymbol{\lambda}. \quad (5.21)$$

Considering decomposition (5.5), since the component  $\boldsymbol{\tau}_\perp \in \ker(B_r)$ , (5.21) reads

$$J_c^T M (\dot{N} \boldsymbol{\mu} + N M_r^{-1} (B_r \boldsymbol{\tau}_\parallel - C_r \boldsymbol{\eta})) + J_c^T C \dot{\mathbf{q}} = J_c^T A^T \boldsymbol{\lambda}. \quad (5.22)$$

The obtained vector on the left side of (5.22) specifies the total required force and moment at the system's center of mass, where forces and moments are decoupled, expressed in the main body frame. Let us denote this vector by  $\mathbf{h}$ .

$$\mathbf{h} := J_c^T M (\dot{N} \boldsymbol{\mu} + N M_r^{-1} (B_r \boldsymbol{\tau}_\parallel - C_r \boldsymbol{\eta})) + J_c^T C \dot{\mathbf{q}}. \quad (5.23)$$

Additionally, a matrix whose columns specify the contribution of each component of

$\lambda$  in  $\mathbf{h}$ , denoted by  $K$  is

$$K := J_c^T A^T. \quad (5.24)$$

In the following subsections the traction optimization procedure is detailed first for motion on a straight line, and then for moving on a general curve. It is noteworthy that the motion on a straight line or on a curve can be distinguished by measuring the steering angle in autonomous rovers with steering degrees of freedom. If the steering angle is zero, it means that system is moving on a straight line. In type  $(2, 0)$  rovers, estimation of the main body angular velocity can be used to examine whether the system moves on a line or on a curve.

### 5.3.1 Moving on a Straight Line

Let us decompose the vector of tractive forces  $\lambda$  as

$$\lambda = \begin{bmatrix} \lambda_f \\ \lambda_l \end{bmatrix}, \quad (5.25)$$

where  $\lambda_f \in \mathbb{R}^g$  is the vector of longitudinal tractive forces whose dimension is specified in Assumption 5.3 and  $\lambda_l \in \mathbb{R}^{m-g}$  is the vector of lateral tractive forces with respect to the local coordinate frame attached to the wheels. Similarly, the vector  $V$  and the matrix  $D$  in (5.14) can be written in the following form:

$$V = \begin{bmatrix} V_f \\ V_l \end{bmatrix}, \quad D = \begin{bmatrix} D_f \\ D_l \end{bmatrix}. \quad (5.26)$$

When the system is moving on a straight line, I consider the following cost function for traction optimization.

$$r_f = \frac{1}{2} (\mathcal{U}_f \mathbf{n} - \Xi_f \lambda_f)^T (\mathcal{U}_f \mathbf{n} - \Xi_f \lambda_f) \quad (5.27)$$

where  $\mathcal{U}_f \in \mathbb{R}^{g \times g}$  is a diagonal matrix whose elements are the static friction coefficients at each wheel in longitudinal direction. Here,  $\Xi_f$  is the sign specifier for the total

required longitudinal forces at the system's center of mass:

$$\Xi_f = \begin{cases} 1 & \mathbf{h}_1(\mathbf{x}, \boldsymbol{\tau}_{\parallel}) \geq 0, \\ -1 & \mathbf{h}_1(\mathbf{x}, \boldsymbol{\tau}_{\parallel}) < 0, \end{cases} \quad (5.28)$$

where  $\mathbf{h}_1$  is the first component of  $\mathbf{h}$ .

*Note.* Based on Assumption 5.3, in (5.27) the vector  $\mathbf{n}$  includes all required normal reaction forces.

Substituting  $\mathbf{n}$  in (5.27) by (5.15),  $r_f$  becomes

$$r_f = \frac{1}{2}(\mathcal{U}_f(\mathbf{k} + \Phi\boldsymbol{\lambda} + \Pi\boldsymbol{\tau}) - \Xi_f\boldsymbol{\lambda}_f)^T(\mathcal{U}_f(\mathbf{k} + \Phi\boldsymbol{\lambda} + \Pi\boldsymbol{\tau}) - \Xi_f\boldsymbol{\lambda}_f). \quad (5.29)$$

Substituting  $\boldsymbol{\lambda}$  in (5.29) by (5.14) and based on decomposition in (5.26), I have

$$r_f = \frac{1}{2}(\mathcal{U}_f(\mathbf{k} + \Phi(V + D\boldsymbol{\tau}) + \Pi\boldsymbol{\tau}) - \Xi_f(V_f + D_f\boldsymbol{\tau}))^T(\mathcal{U}_f(\mathbf{k} + \Phi(V + D\boldsymbol{\tau}) + \Pi\boldsymbol{\tau}) - \Xi_f(V_f + D_f\boldsymbol{\tau})). \quad (5.30)$$

Substituting  $\boldsymbol{\tau}$  by (5.5) and based on (5.6), I can introduce

$$\begin{aligned} \mathbf{p}_f &= \mathcal{U}_f(\mathbf{k} + \Phi(V + D\boldsymbol{\tau}_{\parallel}) + \Pi\boldsymbol{\tau}_{\parallel}) - \Xi_f(V_f + D_f\boldsymbol{\tau}_{\parallel}), \\ Q_f &= (\mathcal{U}_f\Phi D + \mathcal{U}_f\Pi - \Xi_f D_f)W. \end{aligned}$$

**Assumption 5.5.** I assume that the matrix  $Q_f$  is everywhere full rank.

Accordingly, (5.30) becomes

$$r_f = \frac{1}{2}(\mathbf{p}_f + Q_f\boldsymbol{\tau}_a)^T(\mathbf{p}_f + Q_f\boldsymbol{\tau}_a), \quad (5.31)$$

and the necessary condition for the optimal solution  $\boldsymbol{\tau}_a$  is obtained as

$$Q_f^T(\mathbf{p}_f + Q_f\boldsymbol{\tau}_a) = \mathbb{O}_{(s-b) \times 1}. \quad (5.32)$$

Since the sign specifier  $\Xi_f$  is only a function of system's states and  $\boldsymbol{\tau}_{\parallel}$ , this condition is linear with respect to  $\boldsymbol{\tau}_a$ ; and hence, the optimal solution  $\boldsymbol{\tau}_a^*$  is calculated by

$$\boldsymbol{\tau}_a^* = -(Q_f^T Q_f)^{-1} Q_f^T \mathbf{p}_f, \quad (5.33)$$

where  $Q_f^T Q_f$  is an invertible square matrix, since  $Q_f$  is assumed to be full rank, uniquely determining the optimal solution.

This optimal distribution of control actions may result in wheel-fighting. In this thesis, I call a rover's wheel to fight against the rover's motion, if the corresponding tractive force  $\lambda_i$  at the wheel has negative contribution in the total required force at system's center of mass  $\mathbf{h}$ , i.e.,

$$\mathbf{h} \cdot K_i \lambda_i < 0, \quad (5.34)$$

where the operator  $\cdot$  represents the scalar product between two vectors and  $K_i$  is the  $i^{\text{th}}$  column of matrix  $K$ .

To investigate the wheel-fighting phenomenon, I calculate the longitudinal tractive forces corresponding to the optimal control input  $\boldsymbol{\tau}^* := \boldsymbol{\tau}_{\parallel} + W\boldsymbol{\tau}_a^*$  by

$$\boldsymbol{\lambda}_f^* = V_f + D_f \boldsymbol{\tau}^*, \quad (5.35)$$

and their contributions in the required force  $\mathbf{h}$  by

$$c_i = \mathbf{h} \cdot K_i \boldsymbol{\lambda}_{fi}^*, \quad (5.36)$$

where  $\boldsymbol{\lambda}_{fi}^*$  is the  $i^{\text{th}}$  component of the vector  $\boldsymbol{\lambda}_f^*$ . I define the vector of fighting tractive forces  $\boldsymbol{\lambda}_{fa} \in \mathbb{R}^b$  that contains the longitudinal tractive forces whose contributions in the required force is less than a small positive number  $\epsilon$ . Accordingly, I form the vector  $V_{fa}$  and the matrix  $D_{fa}$  by respectively collecting the rows of  $V_f$  and  $D_f$  corresponding to the components of  $\boldsymbol{\lambda}_{fa}$ . To prevent wheel-fighting, I kill the fighting tractive forces generated due to the proposed optimal distribution of control actions. I first find the subspace of  $\ker(B_r)$ , where  $\boldsymbol{\lambda}_{fa} = 0$ , through solving the following equation for  $\boldsymbol{\tau}_a$ :

$$\begin{aligned} V_{fa} + D_{fa}(\boldsymbol{\tau}_{\parallel} + W\boldsymbol{\tau}_a) &= 0, \\ \rightarrow D_{fa}W\boldsymbol{\tau}_a &= -(V_{fa} + D_{fa}\boldsymbol{\tau}_{\parallel}). \end{aligned} \quad (5.37)$$

The space of all  $\boldsymbol{\tau}_a$  that satisfy (5.37) and kill the fighting tractive forces can be identified by

$$\boldsymbol{\tau}_a = \boldsymbol{\tau}_{a\parallel} + W_n \boldsymbol{\tau}_{an}, \quad (5.38)$$

where

$$\boldsymbol{\tau}_{a\parallel} = -(D_{fa}W)^T ((D_{fa}W)(D_{fa}W)^T)^{-1} (V_{fa} + D_{fa}\boldsymbol{\tau}_{\parallel}) \in \mathbb{R}^{s-b} \quad (5.39)$$

is the right pseudo-inverse solution of (5.37),  $W_n \in \mathbb{R}^{(s-b) \times (s-b-h)}$  is a matrix whose columns span  $\ker(D_{f_a}W)$ , i.e.,  $D_{f_a}W W_n = 0$ , and  $\boldsymbol{\tau}_{an} \in \mathbb{R}^{(s-b-h)}$  is an arbitrary vector. To kill the fighting tractive forces, I orthogonally project the vector of optimal control distribution  $\boldsymbol{\tau}_a^*$  onto the subspace identified by (5.38). A sub-optimal solution  $\boldsymbol{\tau}_a^{* \prime}$  is then obtained by

$$\boldsymbol{\tau}_a^{* \prime} = \boldsymbol{\tau}_{a\parallel} + W_n \boldsymbol{\tau}_{an\parallel}, \quad (5.40)$$

where

$$\boldsymbol{\tau}_{an\parallel} := W_n^T (W_n W_n^T)^{-1} (\boldsymbol{\tau}_a^* - \boldsymbol{\tau}_{a\parallel}), \quad (5.41)$$

is the right pseudo-inverse solution.

*Remark 5.4.* The solution  $\boldsymbol{\tau}_a^{* \prime}$  is not optimizing the defined cost function  $r_f$ , but since the orthogonal projection is used, it is the closest solution to  $\boldsymbol{\tau}_a^*$  in the space of control distributions killing the fighting tractive forces. The optimality of  $\boldsymbol{\tau}_a^{* \prime}$  can be investigated applying Karush–Kuhn–Tucker theorem which is out of scope of this thesis [98].

*Remark 5.5.* If the dimension of  $\boldsymbol{\lambda}_{f_a}$  is greater than or equal to that of  $\boldsymbol{\tau}_a$ , i.e.  $h \geq s-b$ , the optimization becomes over-constrained, and the pseudo inverse solution provides the best control distribution, i.e  $\boldsymbol{\tau}_a = 0$ .

Since I may introduce new fighting directions when applying  $\boldsymbol{\tau}_a^{* \prime}$ , the above explained algorithm may be repeated for the sub-optimal control distribution  $\boldsymbol{\tau}_a^{* \prime}$  in the restricted subspace of  $\ker(B_r)$ . In this process, I shrink the space of sub-optimal solutions by adding new constraints, until I find a solution or exit without obtaining a distribution. In the latter case,  $\boldsymbol{\tau}_a = 0$  provides the best control distribution. The complete flowchart of this optimization algorithm is depicted in Fig.5.2.

### 5.3.2 Moving on a Curve

In this thesis, I propose a two-stage optimization algorithm for traction improvement when the system is moving on a curve. In the first stage, I focus on the traction improvement in the lateral direction of the main body coordinate frame. Often, this negatively impacts the traction in the longitudinal direction due to generating a moment about system's center of mass, which will be minimized as part of the objective function proposed for the first stage of optimization. The rover's traction

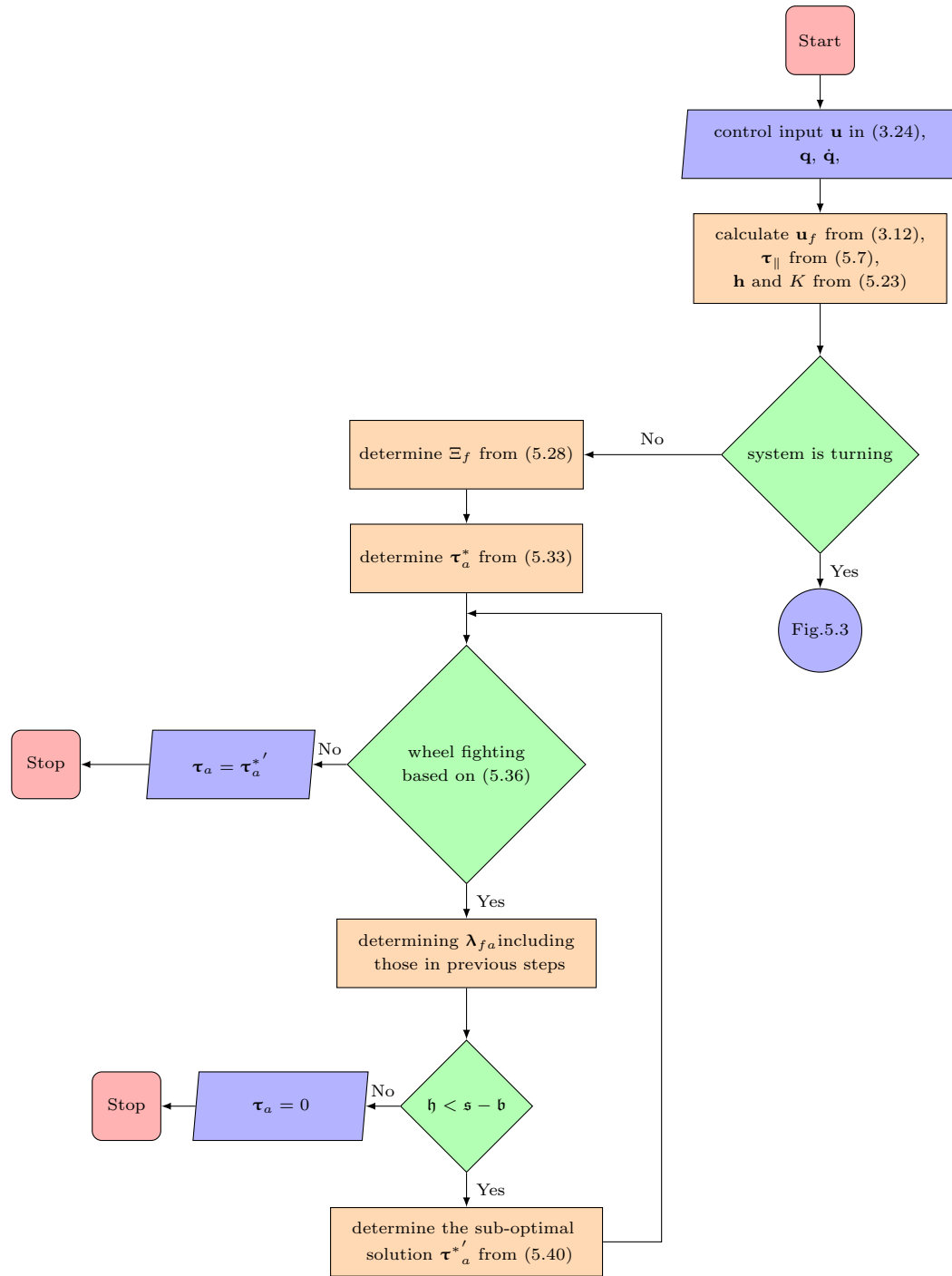


Figure 5.2: Flowchart of the proposed traction optimization algorithm in linear motion

in the longitudinal direction of the wheels is then optimized separately in the second stage.

### Lateral Traction Optimization

This stage of optimization suffers from a number of difficulties that prevents us from using a similar cost function that presented in Section 5.3.1 to optimize the lateral traction of the system: (i) The steering angles in a steerable system result in the contribution of both  $\boldsymbol{\lambda}_l$  and  $\boldsymbol{\lambda}_f$  in the lateral direction of the motion. I must then consider decomposition of the lateral and longitudinal tractive forces in the Euclidean space, which inevitably introduces coupling between them. (ii) Linearly dependent lateral tractive forces often exist in the system, making the problem of identifying all tractive forces underdetermined, and hence, making the definition of the corresponding normal forces problematic (Remark 5.3 and Assumption 5.3). (iii) The coupling between the lateral and longitudinal traction optimization must be addressed.

Let  $\boldsymbol{\lambda}_{lb} \in \mathbb{R}^{\mathfrak{k}}$  ( $\mathfrak{k} = \mathfrak{m} - \mathfrak{g}$ ) be the vector of tractive forces in the lateral direction of the motion corresponding to the components of  $\boldsymbol{\lambda}_l$ . Each component of  $\boldsymbol{\lambda}_{lb}$  represents the component of the corresponding lateral tractive force (identified by an element of  $\boldsymbol{\lambda}_l$ ) in the lateral direction of the main body, along with any existing component of longitudinal tractive forces in that direction. Such a coupling appears at steerable wheels. The functionality of  $\boldsymbol{\lambda}_{lb}$  is defined by

$$\boldsymbol{\lambda}_{lb} = \Upsilon_l(\mathbf{q})\boldsymbol{\lambda}, \quad (5.42)$$

where  $\Upsilon_l: \mathbb{R}^{\mathfrak{m}} \rightarrow \mathbb{R}^{\mathfrak{k}}$ . I also denote the vector of normal reaction forces corresponding to the components of  $\boldsymbol{\lambda}_{lb}$  by  $\mathbf{n}'_l$ , which is formed based on the definition of  $\mathbf{n}'$  and Assumption 5.3. The static friction coefficients for the lateral direction of the main body are obtained according to the coupling between the components of  $\boldsymbol{\lambda}_l$  and  $\boldsymbol{\lambda}_f$  and the projections performed onto the lateral direction of the motion in the definition of  $\boldsymbol{\lambda}_{lb}$ :

$$\mathfrak{U}_l = \Upsilon_l(\mathbf{q})\mathfrak{U}. \quad (5.43)$$

Then, the elements of the vector  $\Upsilon_l(\mathbf{q})\mathfrak{U}\mathbf{n}' = \Upsilon_l(\mathbf{q})\mathfrak{U}L_n\mathbf{n}$  represent the multiplication of the static friction coefficients in the lateral direction of the main body and the normal reaction forces corresponding to the components of  $\boldsymbol{\lambda}_{lb}$ .

Traction optimization in the lateral direction of the motion leads to an optimal

distribution of the components of  $\boldsymbol{\lambda}_{lb}$  based on the magnitude of the elements of  $\Upsilon_l(\mathbf{q})\mathcal{U}\mathbf{n}'$ . This distribution results in generating an excess moment about system's center of mass in comparison with the required moment, i.e.  $\mathbf{h}_3$ , the third component of  $\mathbf{h}$ . This excess moment has to be compensated by longitudinal tractive forces. In other words, traction improvement in lateral direction negatively impacts traction in the longitudinal direction. Hence, the difference between generated moment at system's center of mass by components of  $\boldsymbol{\lambda}_{lb}$  and the  $\mathbf{h}_3$ , weighted by a positive constant  $v$  must be included in the definition of the cost function. Let us introduce a row vector  $\Upsilon_t: \mathbb{R}^{\mathfrak{t}} \rightarrow \mathbb{R}$  mapping the components of  $\boldsymbol{\lambda}_{lb}$  to their generated torque at system's center of mass, denoted by  $m_{lb}$ . Therefore,

$$m_{lb} = \Upsilon_t \Upsilon_l(\mathbf{q})\boldsymbol{\lambda}. \quad (5.44)$$

Based on the above considerations, the cost function  $r_l$  for traction optimization in the lateral direction of the motion is defined as:

$$r_l = (\Gamma\mathbf{n} - \Upsilon\boldsymbol{\lambda} - \boldsymbol{\kappa})^T \Lambda (\Gamma\mathbf{n} - \Upsilon\boldsymbol{\lambda} - \boldsymbol{\kappa}), \quad (5.45)$$

where

$$\Gamma := \begin{bmatrix} \Upsilon_l(\mathbf{q})\mathcal{U}L_n \\ \mathbb{O}_{1 \times \mathfrak{g}} \end{bmatrix} \quad \Upsilon := \begin{bmatrix} \Xi_l \Upsilon_l(\mathbf{q}) \\ -\Upsilon_t \Upsilon_l(\mathbf{q}) \end{bmatrix} \quad \boldsymbol{\kappa} := \begin{bmatrix} \mathbb{O}_{\mathfrak{t} \times 1} \\ \mathbf{h}_3(\mathbf{x}, \boldsymbol{\tau}_{\parallel}) \end{bmatrix} \quad \Lambda := \begin{bmatrix} \mathbb{I}_{\mathfrak{t} \times \mathfrak{t}} & \mathbb{O}_{\mathfrak{t} \times 1} \\ \mathbb{O}_{1 \times \mathfrak{t}} & v \end{bmatrix}. \quad (5.46)$$

Here, the parameter  $\Xi_l$  is the sign specifier for the total required lateral forces at the system's center of mass:

$$\Xi_l = \begin{cases} 1 & \mathbf{h}_2(\mathbf{x}, \boldsymbol{\tau}_{\parallel}) \geq 0 \\ -1 & \mathbf{h}_2(\mathbf{x}, \boldsymbol{\tau}_{\parallel}) < 0 \end{cases} \quad (5.47)$$

where  $\mathbf{h}_2$  is the second component of  $\mathbf{h}$ .

*Remark 5.6.* As determination of the terms  $\Upsilon_l$ ,  $L_n$ , and  $\Upsilon_t$  is dependant on the structure and the type of the autonomous rover/vehicle, it is discussed in more detail in section 5.4 for a specific autonomous rover system.

Substituting  $\mathbf{n}$  in (5.45) by (5.15),  $r_l$  becomes

$$r_l = (\Gamma(\mathbf{k} + \Phi\boldsymbol{\lambda} + \Pi\boldsymbol{\tau}) - \Upsilon\boldsymbol{\lambda} - \boldsymbol{\kappa})^T \Lambda (\Gamma(\mathbf{k} + \Phi\boldsymbol{\lambda} + \Pi\boldsymbol{\tau}) - \Upsilon\boldsymbol{\lambda} - \boldsymbol{\kappa}). \quad (5.48)$$

Substituting  $\lambda$  in (5.48) by (5.14) I have

$$r_l = (\Gamma(\mathbf{k} + \Phi(V + D\boldsymbol{\tau}) + \Pi\boldsymbol{\tau}) - \Upsilon(V + D\boldsymbol{\tau}) - \boldsymbol{\kappa})^T \Lambda(\Gamma(\mathbf{k} + \Phi(V + D\boldsymbol{\tau}) + \Pi\boldsymbol{\tau}) - \Upsilon(V + D\boldsymbol{\tau}) - \boldsymbol{\kappa}). \quad (5.49)$$

Substituting  $\boldsymbol{\tau}$  by (5.5) and introducing

$$\begin{aligned} \mathbf{p}_l &= \Gamma(\mathbf{k} + \Phi(V + D\boldsymbol{\tau}_{\parallel}) + \Pi\boldsymbol{\tau}_{\parallel}) - \Upsilon(V + D\boldsymbol{\tau}_{\parallel}) - \boldsymbol{\kappa}, \\ Q_l &= (\Gamma\Phi D + \Gamma\Pi - \Upsilon D)W, \end{aligned} \quad (5.50)$$

(5.48) becomes

$$\frac{1}{2}(\mathbf{p}_l + Q_l\boldsymbol{\tau}_a)^T \Lambda(\mathbf{p}_l + Q_l\boldsymbol{\tau}_a). \quad (5.51)$$

Hence, the necessary condition for the optimal solution  $\boldsymbol{\tau}_a^*$  is

$$Q_l^T \Lambda Q_l \boldsymbol{\tau}_a^* = -Q_l^T \Lambda \mathbf{p}_l \iff Q_l \boldsymbol{\tau}_a^* = \mathbf{p}_l, \quad (5.52)$$

when  $Q_l$  is full-rank, which holds for car-like rovers containing steering and with wheels located on parallel axes when the steering angles are non-zero.

**Assumption 5.6.** I assume that the dimension of the vector  $\lambda_b$  is less than the number of redundant control directions, i.e.  $\mathfrak{k} < \mathfrak{s} - \mathfrak{b}$ .

Based on Assumption 5.6 the matrix  $Q_l^T \Lambda Q_l$  is not full-rank. Accordingly, (5.52) has infinite number of solutions. Additionally, based on the structure of autonomous rovers and particularly for car-like rovers, even the matrix  $Q_l$  is close to be rank deficient at small steering angles. To remove this rank deficiency, I consider the singular value decomposition of  $Q_l$ , and identify the singular values close to zero using a tolerance. These singular values are then removed and a well-conditioned full-rank matrix  $Q'_l$  is introduced. The space of optimal solutions of (5.52) can be obtained as the summation of an arbitrary vector lied in  $\ker(Q'_l)$ , and the unique vector  $\boldsymbol{\tau}_{l\parallel}^*$  in the subspace orthogonal to  $\ker(Q'_l)$ , i.e.,

$$\boldsymbol{\tau}_{a1}^* = \boldsymbol{\tau}_{l\parallel}^* + Q'_{ln} \boldsymbol{\tau}_{ln}. \quad (5.53)$$

Here,  $Q'_{ln}$  is a matrix whose columns span  $\ker(Q'_l)$  and the vector  $\boldsymbol{\tau}_{ln}$  is an arbitrary vector, such that  $\boldsymbol{\tau}_{l\parallel}^* = Q_l'^T (Q'_l Q_l'^T)^{-1} \mathbf{p}_l$ . Note that the value of  $\boldsymbol{\tau}_{ln}$  does not change

the optimal lateral tractive distribution.

### Longitudinal Traction Optimization

Now that the traction optimization is performed for the lateral directions and the space of optimal solutions is obtained in (5.57), the second stage of optimization is performed within this space concerning the traction improvement in the longitudinal direction of the wheels. Let  $\boldsymbol{\lambda}_{lb}^*$  be the vector of the optimal lateral tractive forces obtained from the first stage of optimization, i.e.,

$$\boldsymbol{\lambda}_{lb}^* = \Upsilon_l(V + D(\boldsymbol{\tau}_{\parallel} + W\boldsymbol{\tau}_{l\parallel}^*)). \quad (5.54)$$

Accordingly, the vector of required forces and moments at the system's center of mass  $\mathbf{h}$  must be updated. I denote the updated vector by

$$\mathbf{h}_l := \mathbf{h} - K\Upsilon_l^T\boldsymbol{\lambda}_{lb}^*. \quad (5.55)$$

The second optimization can be defined as finding an arbitrary vector  $\boldsymbol{\tau}_{ln}$  minimizing the following cost function:

$$r_{fl} = \frac{1}{2}(\mathcal{U}_f\mathbf{n} - \Xi_{fl}\boldsymbol{\lambda}_f)^T(\mathcal{U}_f\mathbf{n} - \Xi_{fl}\boldsymbol{\lambda}_f), \quad (5.56)$$

which is similar to  $r_f$  in Section 5.3.1. Here, the sign specifier  $\Xi_{fl}$  is a diagonal matrix whose components are determined based on  $\mathbf{h}_l$ . If the required moment around the center of mass, i.e. the third component of  $\mathbf{h}_l$ , is positive (counter clock wise), the components of  $\Xi_{fl}$  behind the elements of  $\boldsymbol{\lambda}_f$  related to the port side must be  $-1$  and those related to the starboard side must be  $1$ . On the other hand if the third component of  $\mathbf{h}_l$  is negative (clock wise), this order is switched. Components of  $\Xi_{fl}$  behind the elements of  $\boldsymbol{\lambda}_f$  which are not producing any torques about system's center of mass are also determined based on the sign of longitudinal required force at the center of mass, i.e. the first component of  $\mathbf{h}_l$ .

Let us substitute  $\boldsymbol{\tau}$  and  $\Xi_f$  in (5.30), respectively by

$$\boldsymbol{\tau} = \boldsymbol{\tau}_{\parallel} + W(\boldsymbol{\tau}_{l\parallel} + Q'_l\boldsymbol{\tau}_{ln}). \quad (5.57)$$

and  $\Xi_{fl}$ . Introducing

$$\begin{aligned}\mathbf{p}_{fl} &:= \mathcal{U}_f(\mathbf{k} + \Phi(V + D\boldsymbol{\tau}_{\parallel} + DW\boldsymbol{\tau}_{l\parallel}) + \Pi(\boldsymbol{\tau}_{\parallel} + W\boldsymbol{\tau}_{l\parallel})) \\ &\quad - \Xi_{fl}(V_f + D_f(\boldsymbol{\tau}_{\parallel} + W\boldsymbol{\tau}_{l\parallel})), \\ Q_{fl} &:= (\mathcal{U}_f\Phi D + \mu\Pi - \Xi_{fl}D_f)WQ'_{ln},\end{aligned}$$

the  $r_{fl}$  becomes

$$r_{fl} = \frac{1}{2}(\mathbf{p}_{fl} + Q_{fl}\boldsymbol{\tau}_{ln})^T(\mathbf{p}_{fl} + Q_{fl}\boldsymbol{\tau}_{ln}). \quad (5.58)$$

Then the necessary condition for the optimal solution  $\boldsymbol{\tau}_{ln}^*$  becomes

$$Q_{fl}^T Q_{fl} \boldsymbol{\tau}_{ln} = -Q_{fl}^T \mathbf{p}_{fl}. \quad (5.59)$$

Since  $Q = (\mathcal{U}_f\Phi D + \mu\Pi - \Xi_{fl}D_f)W$  is assumed to be full rank, and generally, the number of longitudinal tractive forces are more than the dimension of  $\boldsymbol{\tau}_{ln}$ , the matrix  $Q_{fl}^T Q_{fl}$  is invertible and the optimal solution  $\boldsymbol{\tau}_{ln}^*$  can be uniquely determined as

$$\boldsymbol{\tau}_{ln}^* = -(Q_{fl}^T Q_{fl})^{-1} Q_{fl}^T \mathbf{p}_{fl}. \quad (5.60)$$

The same procedure for preventing the wheel fighting as explained in 5.3.1 is implemented. The only difference here is that during examining the contributions, the total required force at the center of mass in lateral direction is not considered (it is related to the first optimization). In other words, I replace the second component of  $\mathbf{h}_l$  by zero.

*Remark 5.7.* Since  $\mathfrak{k}$  is often small, existence of the wheel fighting in the lateral direction after the first optimization is less probable. However, I can test the contribution of generated lateral forces on the lateral required force and if system experiences fighting, the optimization is not performed and only the pseudo inverse solution is used. The same applies whenever the number of tractive forces that must be killed is more than or equal to the dimension of the vector  $\boldsymbol{\tau}_{ln}$ .

## 5.4 Implementation on a Six-wheel Lunar Rover

*Remark 5.8.* For simplicity, in this section, I consider that the steering torque is only applied to the port front wheel. Accordingly,  $\dim(\boldsymbol{\tau}) = \mathfrak{s} = 7$  and the last column

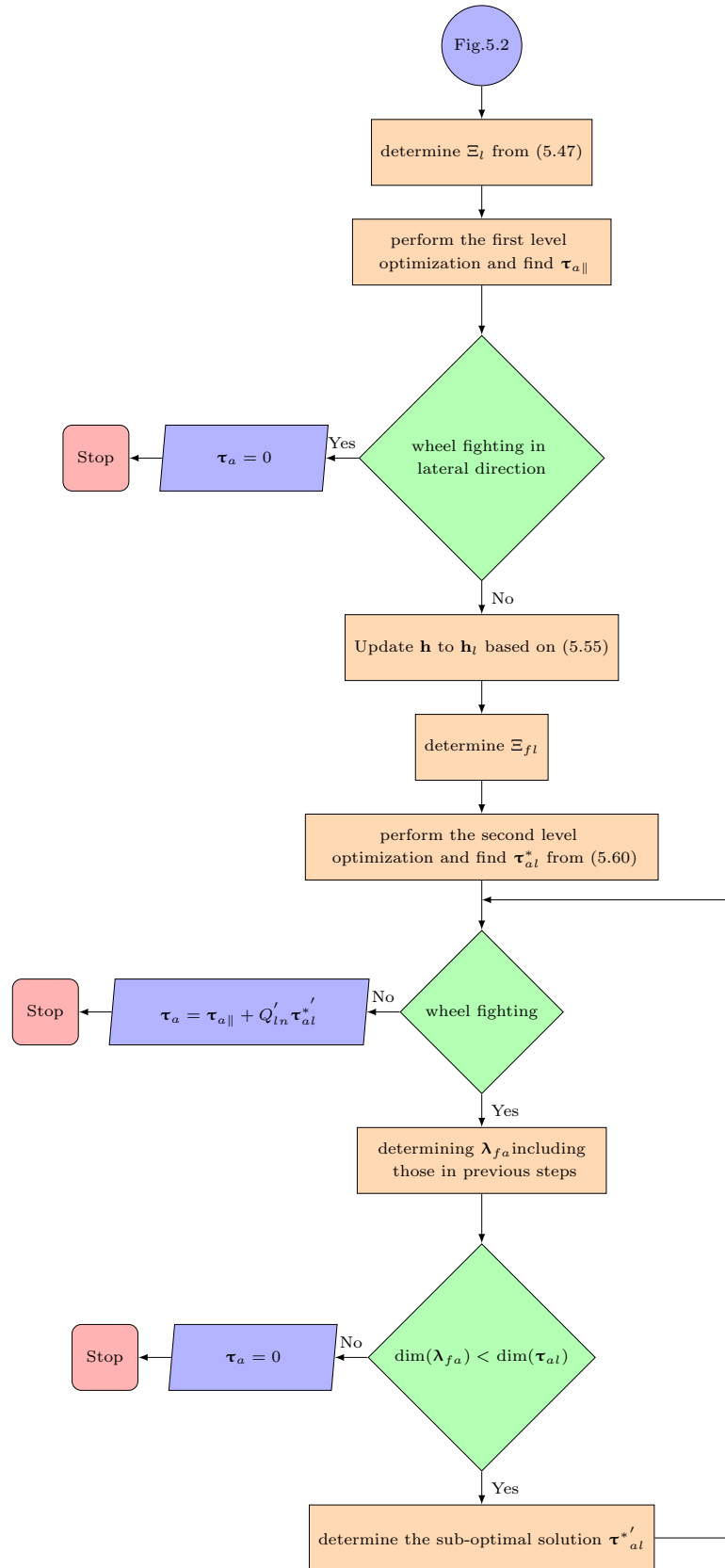


Figure 5.3: Flow chart of the proposed traction optimization algorithm in turning

of matrix  $\hat{B}$  in (3.2) must be eliminated and its fifth row must contain only zeros. It also stabilizes the input-output linearized error dynamics of the system using only a simple proportional integral derivative control law (PID).

To begin with, let us eliminate the non-tractive holonomic constraint forces by performing a proper restriction of the configuration manifold. For the system under study, only the constraint between steering degrees of freedom (Ackerman condition) is non-tractive. That constraint is stated in the first row of matrix  $\hat{A}$  in (3.33). Accordingly the restricted configuration manifold changes to  $Q = \mathbb{R}^3 \times \mathbb{T}^7$  whose elements are  $\mathbf{q} = [x_b \ y_b \ \theta \ \psi_s \ \psi_1 \ \psi_2 \ \psi_3 \ \psi_4 \ \psi_p \ \delta_p]$ . The inclusion map  $\iota(\mathbf{q})$  also becomes

$$\hat{\mathbf{q}} = \iota_Q(\mathbf{q}) = \begin{bmatrix} x_b & y_b & \theta & \psi_s & f_A(\delta_p) & \psi_1 & \psi_2 & \psi_3 & \psi_4 & \psi_p & \delta_p \end{bmatrix}^T, \quad (5.61)$$

and the non zero elements of its Jacobin are

$$\begin{aligned} J_{1,1} = J_{2,2} = J_{3,3} = J_{4,4} = J_{6,5} &= J_{7,6} = J_{8,7} = J_{9,8} = J_{10,9} = J_{11,10} = 1, \\ J_{5,10} &= \frac{df_A}{d\delta_p}(\delta_p). \end{aligned} \quad (5.62)$$

The dynamical equations described in the restricted configuration manifold  $Q$  in (3.6), needs to get updated according to the new restriction. Consequently, the matrix  $E$  changes to  $E = [\mathbb{O}_{8 \times 1} \quad \mathbb{I}_{8 \times 8}]$ .

By updating the matrix  $N$  to the following matrix

$$N = \begin{bmatrix} \frac{R_w}{L} \cos(\theta)(L \cos(\delta_p) + c \sin(\delta_p)) & 0 \\ \frac{R_w}{L} \sin(\theta)(L \cos(\delta_p) + c \sin(\delta_p)) & 0 \\ \frac{R_w}{L} \sin(\delta_p) & 0 \\ N_{4,1} & 0 \\ \cos(\delta_p) & 0 \\ \frac{2c}{L} \sin(\delta_p) + \cos(\delta_p) & 0 \\ \cos(\delta_p) & 0 \\ \frac{2c}{L} \sin(\delta_p) + \cos(\delta_p) & 0 \\ 1 & 0 \\ 0 & 1 \end{bmatrix}, \quad (5.63)$$

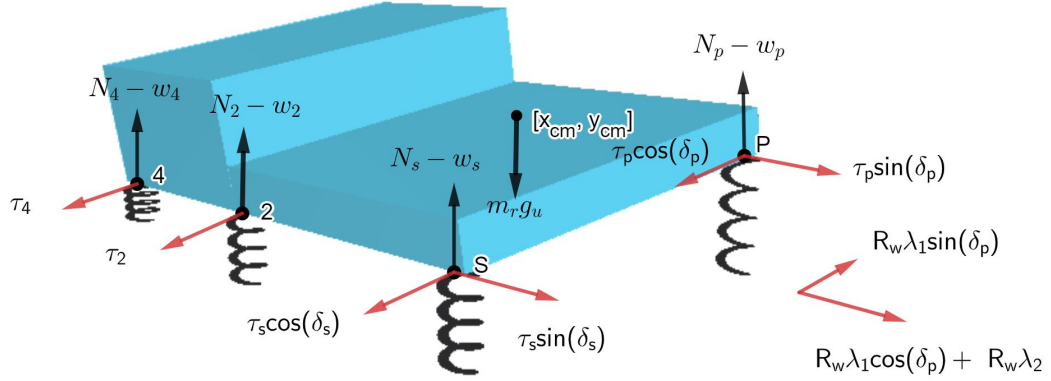


Figure 5.4: Free body diagram of the system under study in the roll, pitch, and vertical directions

where

$$N_{4,1} = \sin(\delta_p) \left( \frac{2c}{L} \cos(\delta_s) + \sin(\delta_s) \right) + \cos(\delta_p) \cos(\delta_s),$$

the reduced projected state space representation of the system in the configuration manifold restricted by non-tractive holonomic constraints is obtained based on (3.8).

Based on the determined matrices, the vector of tractive constraint forces  $\boldsymbol{\lambda} \in \mathbb{R}^8$  for the system under study, can now be calculated based on (5.13). In respect to the arrangement of constraints in the constraint matrix  $A = EJ^T \hat{A}$ , the first two components of  $\boldsymbol{\lambda}$  corresponding to the tractive forces in the lateral directions of the wheel  $\lambda_l$  and the rest are corresponding to  $\boldsymbol{\lambda}_f$ .

For the system under study, the normal reaction forces can be estimated based on Assumption 5.2. The free body diagram of the main body assuming that all control torques and lateral tractive forces are positive is depicted in Fig.5.4. In this figure, forces are illustrated by black arrows and moments are illustrated by red arrows. Additionally,  $\lambda_1$  and  $\lambda_2$  respectively denote the first and second components of  $\boldsymbol{\lambda}$  and  $\tau_i$  denotes the throttle/brake control torque applied to each wheel,  $N_i$  denotes the ground normal reaction forces and  $w_i$  denotes the weight of the wheels (indices are chosen based on Fig.3.1).

*Remark 5.9.* Since the planar motion is assumed, the moments generated by lateral tractive forces ( $\boldsymbol{\lambda}_b$ ) around the wheel-body joints, are approximately equal to the multiplication of the tractive forces and radius of the wheels. Additionally, such moments along with the control torques applied to wheels can be transferred to the

main body with a negative sign, based on Assumption 5.2.

**Assumption 5.7.** All wheels have equal weight denoted by  $w_w$ .

According to Assumption 5.2, the summation of all forces in the vertical direction is equal to zero, i.e.,

$$N_1 + N_2 + N_3 + N_4 + N_p + N_s - m_r g_u - 6w_w = 0, \quad (5.64)$$

Additionally, the summations of all moments produced at point 4, See Fig.5.4, in the pitch and roll directions are equal to zero, i.e.,

$$\begin{aligned} +^{\wedge} \sum M_{roll4} &= (N_1 + N_2)L_0 + (N_p + N_s)(L_0 + L) \\ &\quad - (x_{cm} + L_0)m_r g_u - 2w_w(2L_0 + L) + R_w \boldsymbol{\Phi}_1^T \boldsymbol{\lambda} + \boldsymbol{\pi}_1^T \boldsymbol{\tau} = 0, \end{aligned} \quad (5.65)$$

$$\begin{aligned} +^{\vee} \sum M_{pitch4} &= (N_1 + N_3 + N_p)2c - (y_{cm} + c)m_r g_u \\ &\quad - 6w_w c + R_w \boldsymbol{\Phi}_2^T \boldsymbol{\lambda} + \boldsymbol{\pi}_2^T \boldsymbol{\tau} = 0, \end{aligned} \quad (5.66)$$

where  $\sum M_{roll4}$  is the total moment produced at point 4 in roll direction,  $\sum M_{pitch4}$  is the total moment produced at point 4 in pitch direction, and

$$\begin{aligned} \boldsymbol{\Phi}_1 &= \begin{bmatrix} -\sin(\delta_p) & 0 & 0 & 0 & 0 & 0 & 0 & 0 \end{bmatrix}^T \\ \boldsymbol{\pi}_1 &= \begin{bmatrix} \cos(f_A) & 1 & 1 & 1 & 1 & \cos(\delta_p) & 0 \end{bmatrix}^T \\ \boldsymbol{\Phi}_2 &= \begin{bmatrix} \cos(\delta_p) & 1 & \mathbb{O}_{1 \times 6} \end{bmatrix}^T \\ \boldsymbol{\pi}_2 &= \begin{bmatrix} \sin(f_A) & \mathbb{O}_{1 \times 4} & \sin(\delta_p) & 0 \end{bmatrix}^T \end{aligned}$$

are determined based on the sequence of components in vectors  $\boldsymbol{\tau}$  and  $\boldsymbol{\lambda}$ . Clearly, these equations are not enough to obtain all normal reaction forces and the problem is underdetermined. To resolve this, I assume that the difference between the normal reaction forces and the weight of the wheels are transferred to the main body through suspension springs which are only allowed to deform in the vertical direction, i.e., such forces are equal to the multiplication of the suspension springs' stiffness and

their deformation. Let us denote the deformations of the suspension spring at  $A$  by  $\Delta_A$ . Assuming that the main body is rigid and the displacement angles in roll direction, denoted by  $\Delta_r$ , and in pitch direction, denoted by  $\Delta_p$ , is small, the following relationships between the deformations of the springs can be derived:

$$\begin{aligned}
\Delta_2 &= \Delta_A - L_0\Delta_r, \\
\Delta_s &= \Delta_A - (L + L_0)\Delta_r, \\
\Delta_3 &= \Delta_A - (2c)\Delta_p, \\
\Delta_1 &= \Delta_A - L_0\Delta_r - 2c\Delta_p, \\
\Delta_p &= \Delta_A - (L + L_0)\Delta_r - 2c\Delta_p,
\end{aligned} \tag{5.67}$$

where  $\Delta_1$ ,  $\Delta_2$ ,  $\Delta_3$  respectively denote the vertical deformation of the springs located at the wheels 1, 2, and 3,  $\Delta_s$  is the vertical deformation of the suspension spring corresponding to starboard front wheel, and  $\Delta_p$  is the vertical deformation of the port front wheel's suspension spring. Let us denote the stiffness of the suspension springs corresponding to front wheels by  $k_f$ , center wheels by  $k_c$ , and rear wheels by  $k_r$ . Based on the first and third equations in (5.67) I can substitute  $\Delta_r$  and  $\Delta_p$  by

$$\begin{aligned}
\Delta_r &= -\frac{\Delta_2 - \Delta_A}{L_0}, \\
\Delta_p &= -\frac{\Delta_3 - \Delta_A}{2c},
\end{aligned} \tag{5.68}$$

in the remaining equations in (5.67). Additionally, the deformations can be substituted by the corresponding ratio of vertical forces ( $N_i - w_w$ ) over stiffness of the springs. Consequently, the following additional equations between the normal reaction forces are obtained:

$$\begin{aligned}
-\frac{1}{k_f}(N_s - w_w) - \frac{L}{L_0k_r}(N_4 - w_w) + \frac{L + L_0}{L_0k_c}(N_2 - w_w) &= 0, \\
-\frac{1}{k_c}(N_1 - w_w) + \frac{1}{k_c}(N_2 - w_w) + \frac{1}{k_r}(N_3 - w_w) - \frac{1}{k_r}(N_4 - w_w) &= 0, \\
-\frac{1}{k_f}(N_p - w_w) + \frac{L + L_0}{L_0k_c}(N_2 - w_w) + \frac{1}{k_r}(N_3 - w_w) - \frac{L + L_0}{L_0k_r}(N_4 - w_w) &= 0.
\end{aligned} \tag{5.69}$$

Based on (5.64),(5.65),(5.66), and (5.69), the matrices  $\Phi$ ,  $\Pi$ , and the vector  $\mathbf{k}$  in (5.15)

are determined as:

$$\mathbf{k} = \Psi^{-1} \begin{bmatrix} m_r g_u + 6w_w \\ (x_{cmt} + L_0)m_r g_u + 2w_w(2L_0 + L) \\ (y_{cmt} + c)m_r g_u + 6w_w c \\ \left(-\frac{1}{k_f} + \frac{L}{L_0 k_r} - \frac{L+L_0}{L_0 k_c}\right)w_w \\ 0 \\ \left(-\frac{1}{k_f} + \frac{L+L_0}{L_0 k_c} + \frac{1}{k_r} - \frac{L+L_0}{L_0 k_r}\right)w_w \end{bmatrix} \quad (5.70)$$

$$\Phi = \Psi^{-1} \begin{bmatrix} \mathbb{O}_{1 \times 8} \\ -R_w \boldsymbol{\Phi}_1^T \\ -R_w \boldsymbol{\Phi}_2^T \\ \mathbb{O}_{3 \times 8} \end{bmatrix}, \quad \Pi = \Psi^{-1} \begin{bmatrix} \mathbb{O}_{1 \times 7} \\ -\boldsymbol{\pi}_2^T \\ -\boldsymbol{\pi}_4^T \\ \mathbb{O}_{3 \times 7} \end{bmatrix},$$

where the matrix  $\Psi$  is

$$\Psi = \begin{bmatrix} 1 & 1 & 1 & 1 & 1 & 1 \\ L_0 & L_0 & 0 & 0 & L + L_0 & L + L_0 \\ 2c & 0 & 2c & 0 & 2c & 0 \\ 0 & \frac{L+L_0}{L_0 k_c} & 0 & \frac{-L}{L_0 k_r} & 0 & -\frac{1}{k_f} \\ -\frac{1}{k_c} & \frac{1}{k_c} & \frac{1}{k_r} & -\frac{1}{k_r} & 0 & 0 \\ 0 & \frac{L+L_0}{L_0 k_c} & \frac{1}{k_r} & -\frac{L+L_0}{L_0 k_r} & -\frac{1}{k_f} & 0 \end{bmatrix}. \quad (5.71)$$

*Note.* Matrix  $\Psi$  is full rank.

Based on the structure of matrices  $\Phi$ ,  $\Pi$  and the vector  $\mathbf{k}$ , equation (5.15) results in the vector of normal reaction forces

$$\mathbf{n}^T = \begin{bmatrix} N_1 & N_2 & N_3 & N_4 & N_p & N_s \end{bmatrix}. \quad (5.72)$$

For the system under study, based on the linearity dependency of the constraints

discussed in Section 3.4 the tractive forces in the lateral directions of each wheel can not be determined using (5.13), i.e., (5.13) only gives the summation of such forces at front and center axes and determination of their distribution between the two involved wheels on the port and the starboard sides requires more information.

**Assumption 5.8.** I assume that the lateral tractive forces on each axis is equally distributed between the involved wheels.

Based on assumption 5.8, I consider the average of normal reaction forces at the involved wheels as their corresponding normal reaction forces in the traction optimization cost function. In other word the matrix  $L_n$  in (5.16) is determined as

$$L_n = \begin{bmatrix} 0 & \frac{1}{2} & 0 & 0 & 1 & 0 & 0 & 0 \\ 0 & \frac{1}{2} & 0 & 0 & 0 & 1 & 0 & 0 \\ 0 & 0 & 0 & 0 & 0 & 0 & 1 & 0 \\ 0 & 0 & 0 & 0 & 0 & 0 & 0 & 1 \\ \frac{1}{2} & 0 & 1 & 0 & 0 & 0 & 0 & 0 \\ \frac{1}{2} & 0 & 0 & 1 & 0 & 0 & 0 & 0 \end{bmatrix}^T. \quad (5.73)$$

The matrix  $B_r$  can be calculated based on (3.9). Accordingly, matrix  $W$  in (5.6) whose columns span  $\ker(B_r)$  can be determined as :

$$W = \begin{bmatrix} \frac{L}{\beta} & 0 & 0 & 0 & 0 & 1 & 0 \\ \frac{L \cos(\delta_p) + 2c \sin(\delta_p)}{\beta} & 0 & 0 & 0 & 1 & 0 & 0 \\ \frac{L \cos(\delta_p)}{\beta} & 0 & 0 & 1 & 0 & 0 & 0 \\ \frac{L \cos(\delta_p) + 2c \sin(\delta_p)}{\beta} & 0 & 1 & 0 & 0 & 0 & 0 \\ \frac{L \cos(\delta_p)}{\beta} & 1 & 0 & 0 & 0 & 0 & 0 \end{bmatrix}, \quad (5.74)$$

where

$$\beta = L \cos(\delta_p) \cos(f_A) + 2c \sin(\delta_p) \cos(f_A) + L \sin(\delta_p) \sin(f_A).$$

For the system under study, the matrix  $J_c$  in (5.23) is also obtained as

$$J_c = R_z(\theta) \begin{bmatrix} 1 & 0 & -x_{cmt} \sin(\theta) - y_{cmt} \cos(\theta) & \mathbb{O}_{1 \times 7} \\ 0 & 1 & x_{cmt} \cos(\theta) - y_{cmt} \sin(\theta) & \mathbb{O}_{1 \times 7} \\ 0 & 0 & & 1 & \mathbb{O}_{1 \times 7} \end{bmatrix} \quad (5.75)$$

where  $R_z(\theta)$  is the elementary rotation matrix about the vertical axes,  $x_{cmt}$  and  $y_{cmt}$  are the location of system's center of mass in the main body coordinate frame. Now that every terms involved in (5.23) are determined the vector  $\mathbf{h}$  and the matrix  $K$  can be calculated based on (5.23) and (5.24).

*Remark 5.10.* Since system contains steering degrees of freedom, there is a coupling between the components of  $\boldsymbol{\lambda}_f$  and  $\boldsymbol{\lambda}_l$  corresponding to the front wheels in generation of tractive forces in the lateral and longitudinal direction of the motion.

Based on Remark 5.10, the matrix  $\Upsilon_l$  and the row vector  $\Upsilon_t$  in (5.46) are obtained as

$$\Upsilon_l = \begin{bmatrix} \cos(\delta_p) & 0 & \sin(\delta_p) & \sin(\delta_s) & 0 & 0 & 0 & 0 \\ 0 & 1 & 0 & 0 & 0 & 0 & 0 & 0 \end{bmatrix}, \quad (5.76)$$

$$\Upsilon_t = \begin{bmatrix} (L - x_{cmt}) & -x_{cmt} & (L - x_{cmt}) & (L - x_{cmt}) & 0 & 0 & 0 & 0 \end{bmatrix}.$$

The first row of matrix  $\Upsilon_l$  indicates couplings between the longitudinal and lateral tractive forces at front wheels and the projections performed onto the lateral direction of the motion.

## 5.5 Validation of Estimated Values

In this section, the accuracy of the estimated tractive forces and ground normal reaction forces is evaluated by developing a software-in-the-loop simulation platform using Vortex Studio 2020b. Vortex Studio is a high-fidelity simulation platform developed by CM Labs Simulation Inc, providing a real-time multi-body-dynamics simulation engine along with different wheel-soil interaction tire models [99–103]. First the mechanism is developed as six wheels assembled on the main body using the defined car wheel constraint. The designed suspension springs can be seen in Table.5.1 along with high damping ratios for satisfaction of the quasi-static assumption in vertical,

roll, and pitch directions. The amount of damping ratios are  $10000(\frac{Ns}{m})$ ,  $15000(\frac{Ns}{m})$ , and  $20000(\frac{Ns}{m})$  respectively for front, center and rear wheels. The Ackerman condition is dictated to the front wheels, and all wheel-body constraints are designed as ideal joints. Fig 5.5 depicts the designed mechanism in Vortex.

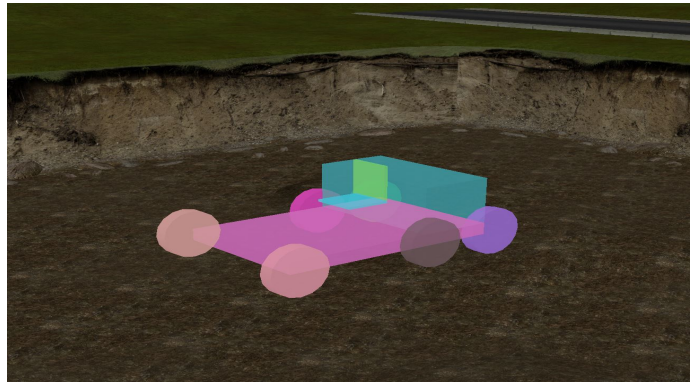


Figure 5.5: The designed mechanism in Vortex

As for the tire models I used “Coulomb Model: Scaled Box Fast”. This model is defined based on dry friction and the term “box” refers to the fact that friction cone is modeled as a box with independent lateral and longitudinal friction coefficients. In other words, when, at contact points I experience a static friction and zero relative velocity, the friction forces can lie anywhere inside a box. The term ”scaled” refers to the specification of a scale between the static friction coefficient and dynamic friction coefficient [104]. For simplicity, I made the rolling resistance at all wheels and the lateral friction at rear wheels equal to zero. Accordingly, system is not subject to any sources of disturbances, except for those coming from the force distribution at wheel-ground contact patch.

A software in the loop simulation environment is developed by connecting the developed model in Vortex to the controller generated in MATLAB Simulink R2019b through UDP communication tool box. The sensory data are received from the model in Vortex and appropriate control command in the form of a control torque command is calculated in Simulink and be sent to the model in Vortex. The values of kinematic and dynamic parameters used in the model along with controller gains can be seen in Table.5.1. The considered desired trajectory for the system is moving on a straight line for the first 30 seconds with a velocity profile contains periodic acceleration deceleration phases with time varying magnitudes. The equation of this velocity

Rover Parameters			
$L$ [m]	$L_0$ [m]	$c$ [m]	$R_w$ [m]
1	0.5	0.55	0.2
$l$ [m]	$x_{cm}$ [m]	$y_{cm}$ [m]	$m_r$ [Kg]
1	0.05	0	600
$m_w$ [Kg]	$J_r$ [Kg/m <sup>2</sup> ]	$J_{wy}$ [Kg/m <sup>2</sup> ]	$J_{wz}$ [Kg/m <sup>2</sup> ]
40	450	1	1
$g_u$ [m/s <sup>2</sup> ]			
1.632			
Suspension Spring Constants			
$k_f$ [N/m]	$k_c$ [N/m]	$k_r$ [m/s]	
30000	45000	60000	
Controller Gains			
$K_p$	$K_I$	$K_d$	
48	64	12	

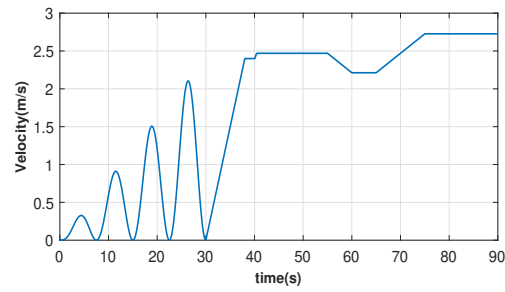
Table 5.1: Kinematic and dynamic parameters of the Lunar rover, suspension spring constants, and controller gains

profile is

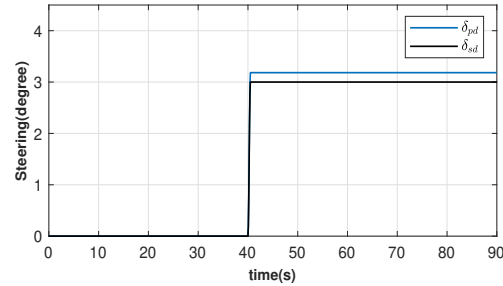
$$0.4t \sin\left(\frac{4\pi}{30}\right)^2. \quad (5.77)$$

Then, system accelerates with constant acceleration equal to 0.3 for 8 seconds and continues its motion with a constant velocity until 55<sup>th</sup> second of the simulation. At 40<sup>th</sup> second a fast steering command is applied in a form of a trapezoidal velocity profile and system starts circling. At 55<sup>th</sup> second I apply a breaking command with constant acceleration equal to 0.05 for five seconds. After circling with the reduced constant velocity for another 5 seconds, I apply a constant acceleration command with magnitude equal to 0.05 for 10 seconds. Afterwards system continues with increased constant velocity for the rest of the simulation time. This desired trajectory can be seen in Fig.5.6

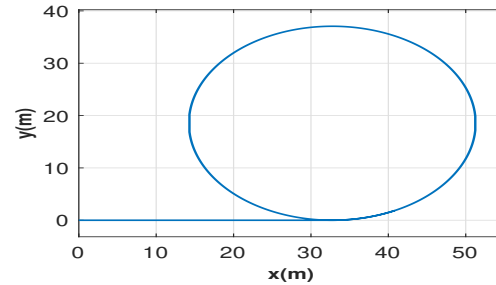
While the system tracks this desired trajectory, the estimated normal forces and tractive forces are compared with the actual values. For simplicity, this comparison is performed when the pseudo-inverse solution is applied, i.e.  $\boldsymbol{\tau}_a = 0$ . It is also noteworthy that the default values in Vortex are considered for the tire deformation and damping. The comparison of the estimated normal forces and actual values at



(a)



(b)



(c)

Figure 5.6: Desired Trajectory. (a) Desired Velocity (b) Desired Steering Angle (c) desired path

all wheels can be seen in Fig.5.8 and the comparison of the estimated longitudinal tractive forces and estimated values can be seen in Fig.5.7. Such comparison for lateral tractive forces is also shown in Fig.5.9

During motion on the straight line the estimated values of the normal forces perfectly match the actual one for front and rear wheels. However, a small discrepancy can be seen in the estimations of the normal forces at center wheels. That can be justified based on the rigid body assumption I made to deal with the indeterminacy of the problem. When the system starts turning, asymmetric distribution of the

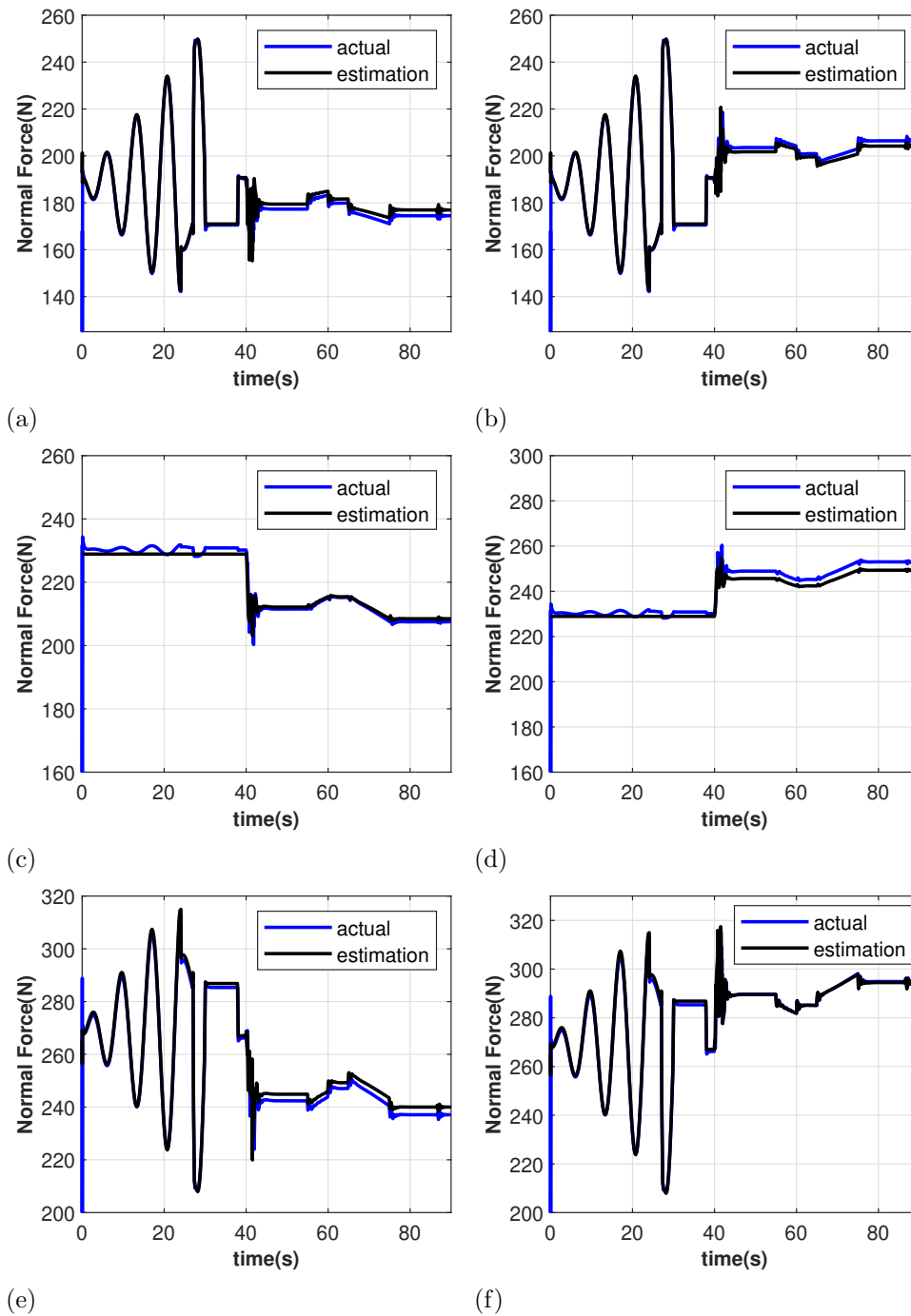


Figure 5.7: Comparison of the estimated normal reaction forces and the actual values. Plots on the left correspond to the wheels at port side and plots on the right correspond to the wheels on starboard side. Sequentially, rows correspond to the front, center, and rear wheels.

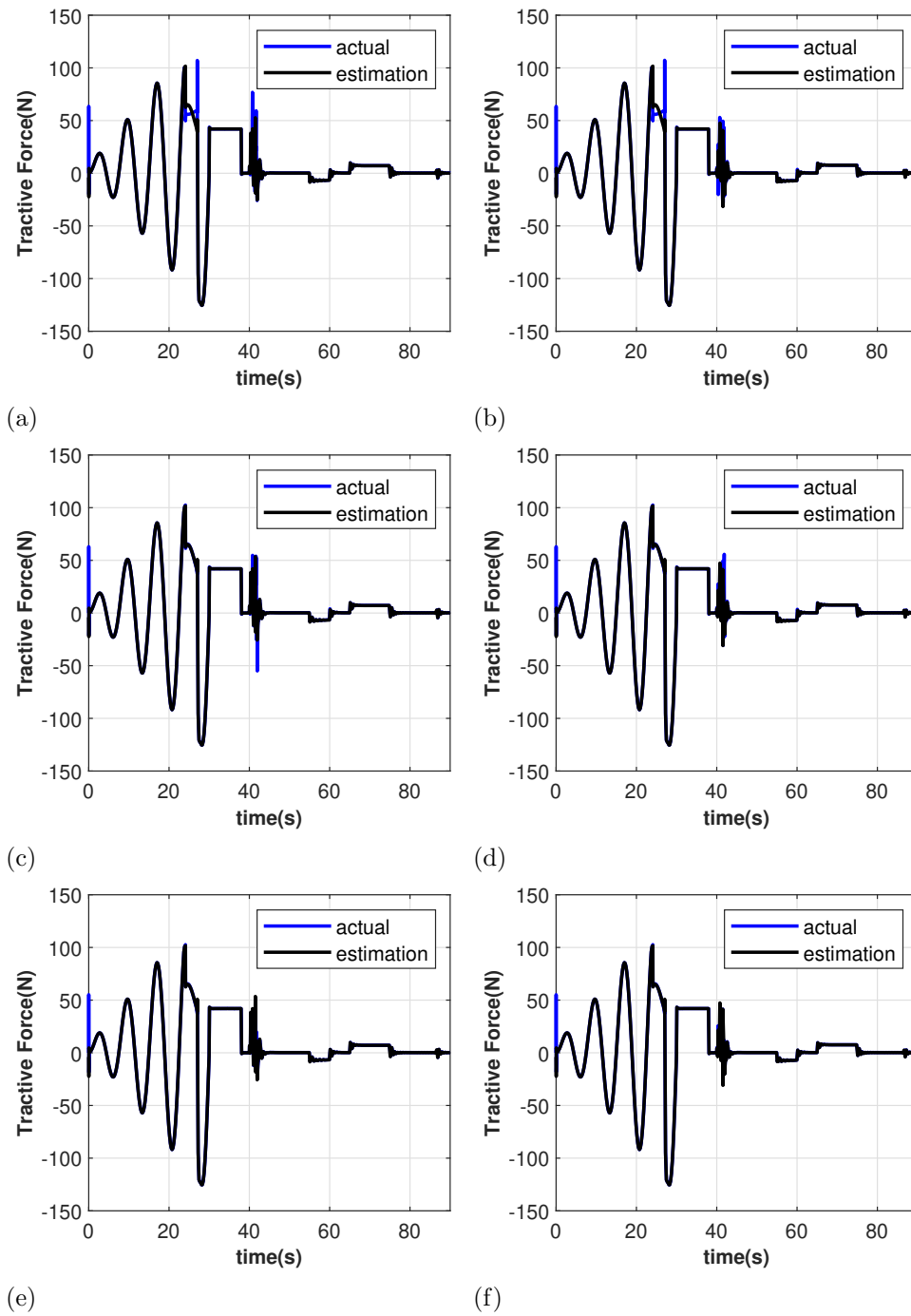


Figure 5.8: Comparison of the estimated longitudinal tractive forces and the actual values. Plots on the left correspond to the wheels at port side and plots on the right correspond to the wheels on starboard side. Sequentially, rows correspond to the front, center, and rear wheels.

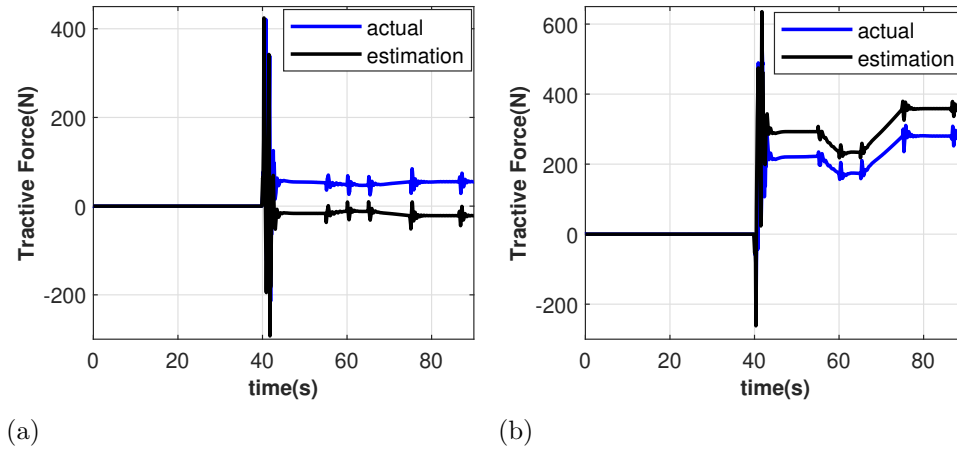


Figure 5.9: Comparison of the estimated Lateral tractive forces and the actual values using default tire deformation. The plot on left corresponds to the front wheels and the plot on right corresponds to the center wheels.

normal forces at contact patch gets violated and that results in a generation of the torque in roll direction. Accordingly, a slight offset between the actual values and the estimated values during circling can be observed. Concerning the longitudinal tractive forces, I have a perfect match except for the 24<sup>th</sup> second of the simulation. At this time, the pseudo-inverse solution initiates the dynamic friction regime at front wheels. Consequently, the nonholonomic constraint equations are not valid anymore and that justifies the observed discrepancy at 24<sup>th</sup> second of the simulation.

Although the estimated lateral tractive forces captures the trend of actual values but in reality such forces are distributed differently between different axes. The reason behind that is the distribution of the tractive forces at the contact patch which is not considered in our estimations. Such distribution produces a considerable amount of torque in the yaw direction and system itself distribute the lateral tractive forces for compensating that. This can be addressed by increasing the coefficient  $\nu$  or by decreasing tire deflection to reduce the area of contact patches. Fig.5.9 indicates the improvement of estimations while the tire deflection is reduced (Note that this figure is corresponded to different desired trajectory depicted in Fig.5.21). As it can be observed by decreasing the tire deformation and moving towards the point contact, better estimation for lateral tractive forces is obtained. However, at 75<sup>th</sup> second of the simulation a sudden drop can be seen in the actual values of the lateral tractive forces at center wheels. This is due to the initiation of the dynamic friction phase

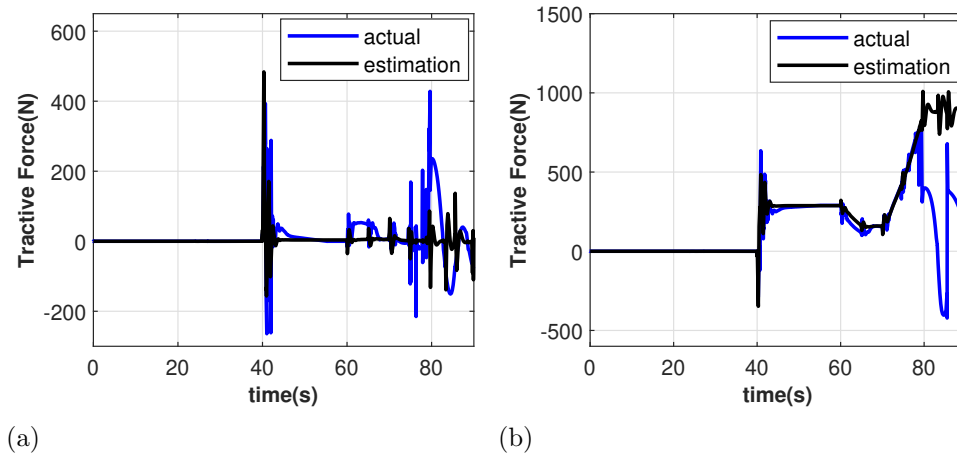


Figure 5.10: Comparison of the estimated Lateral tractive forces and the actual values after decreasing tire deformation. The plot on left corresponds to the front wheels and the plot on right corresponds to the center wheels.

in the lateral direction. It can be observed that system completely drifts and gets out of the prescribed path and since the nonholonomic constraints are violated, the estimated values for the tractive forces are not trustworthy anymore.

Additionally, violation of the point contact assumption, leads to an adhesion force which system has to overcome in order to steer. This can justify the huge amount of forces generated when the sharp steering command is applied.

## 5.6 Simulation Results

In this section the proposed traction optimization algorithm is evaluated using the simulation platform developed in MATLAB R2019b containing an ideal model of the system. In this simulation, the input-output linearized error dynamics of the output has been stabilized applying a Proportional Integral derivative control law (PID) and no disturbances are applied to the system. Table 5.2 indicates the kinematic and dynamic parameters of the simulated system along with the suspension constants and the design parameters defined in the traction optimization algorithm and controller.

The matrix  $\mathcal{U}$  is also considered as

$$\mathcal{U} = \begin{bmatrix} 1.2 & 0 & 0 & 0 & 0 & 0 & 0 & 0 \\ 0 & 1.2 & 0 & 0 & 0 & 0 & 0 & 0 \\ 0 & 0 & 0.6 & 0 & 0 & 0 & 0 & 0 \\ 0 & 0 & 0 & 0.6 & 0 & 0 & 0 & 0 \\ 0 & 0 & 0 & 0 & 0.6 & 0 & 0 & 0 \\ 0 & 0 & 0 & 0 & 0 & 0.6 & 0 & 0 \\ 0 & 0 & 0 & 0 & 0 & 0 & 0.6 & 0 \\ 0 & 0 & 0 & 0 & 0 & 0 & 0 & 0.6 \end{bmatrix}. \quad (5.78)$$

The considered desired trajectory for this simulation can be seen in Fig.5.6. To show

Rover Parameters			
$L$ [m]	$L_0$ [m]	$c$ [m]	$R_w$ [m]
1	0.5	0.55	0.2
$l$ [m]	$x_{cm}$ [m]	$y_{cm}$ [m]	$m_r$ [Kg]
1	0.05	0	600
$m_w$ [Kg]	$J_r$ [Kg/m <sup>2</sup> ]	$J_{wy}$ [Kg/m <sup>2</sup> ]	$J_{wz}$ [Kg/m <sup>2</sup> ]
40	450	1	1
$g_u$ [m/s <sup>2</sup> ]			
1.632			
Suspension Spring Constants			
$k_f$ [N/m]	$k_c$ [N/m]	$k_r$ [m/s]	
30000	45000	60000	
Controller and Traction Optimization Parameters			
$K_p$	$K_I$	$K_d$	$v$
48	64	12	2

Table 5.2: Kinematic and dynamic parameters of the Lunar rover, suspension spring constants, and controller and traction optimization parameters

the effectiveness of the proposed traction optimization algorithm, I ran the simulation once without any control torque distribution and considering only the pseudo-inverse solution, I denote the result of that with "Pinv", and once by activating the proposed traction optimization algorithm, I denote the result of this run by "Optimal". The comparison of the generated normal reaction forces and the generated tractive forces in longitudinal and lateral direction at each wheel is depicted in Figures 5.11, 5.12,

and 5.13.

For the system under study, based on (5.15) and the matrix  $\Pi$  defined in (5.70), at small steering angles only the summation of control torques applied to the system has considerable effect on the normal reaction forces. Therefore, different ways of distributing them between different control directions does not considerably impact the normal reaction forces. Similarly, based on the matrix  $\Phi$  defined in (5.70), at small steering angles the distribution of lateral tractive forces between different axes does not considerably affect the normal forces. Consequently, as the steering angle in the defined desired trajectory is small, traction optimization is not considerably affecting the normal reaction forces.

When the system is not moving, based on the structure of the system and as the center of mass is closer to the rear and center wheels, normal forces at those axes are higher than front wheels. When the system is moving on a straight line, as the steering angle is zero,  $y_{cm} = 0$ , and the lateral tractive forces are also equal to zero, only the quasi-static condition in pitch direction is applied for determination of the distribution of normal forces. Accordingly, the normal reaction forces at each axes is uniformly distributed between the port and starboard wheels. Based on the rigidity assumption of the main body, during acceleration/deceleration phase on a straight line, the normal reaction forces at center axis remains constant. However, when the system accelerates the reaction of commanded control torques applied to the main body results in an increase in the reaction forces at rear wheels and less normal reaction forces at front wheels (front wheels moves a little bit upward). On the other hand, deceleration has an opposite impact and makes normal forces at front and rear axes closer to each other.

When the system starts turning, the effect of the generated lateral tractive forces results in a distribution of normal reaction forces between inner and outer wheels. To neutralize the generated reaction torque by lateral tractive forces in the roll direction, inner wheels must produce less normal forces than outer wheels. Based on the positive steering command, in our case port wheels are inner wheels and starboard wheels are outer. However the summation of the normal forces at port and starboard side for the wheels located on a same axis which is considered as the correspondent normal forces for lateral tractive forces, is specified by the static condition in the pitch direction

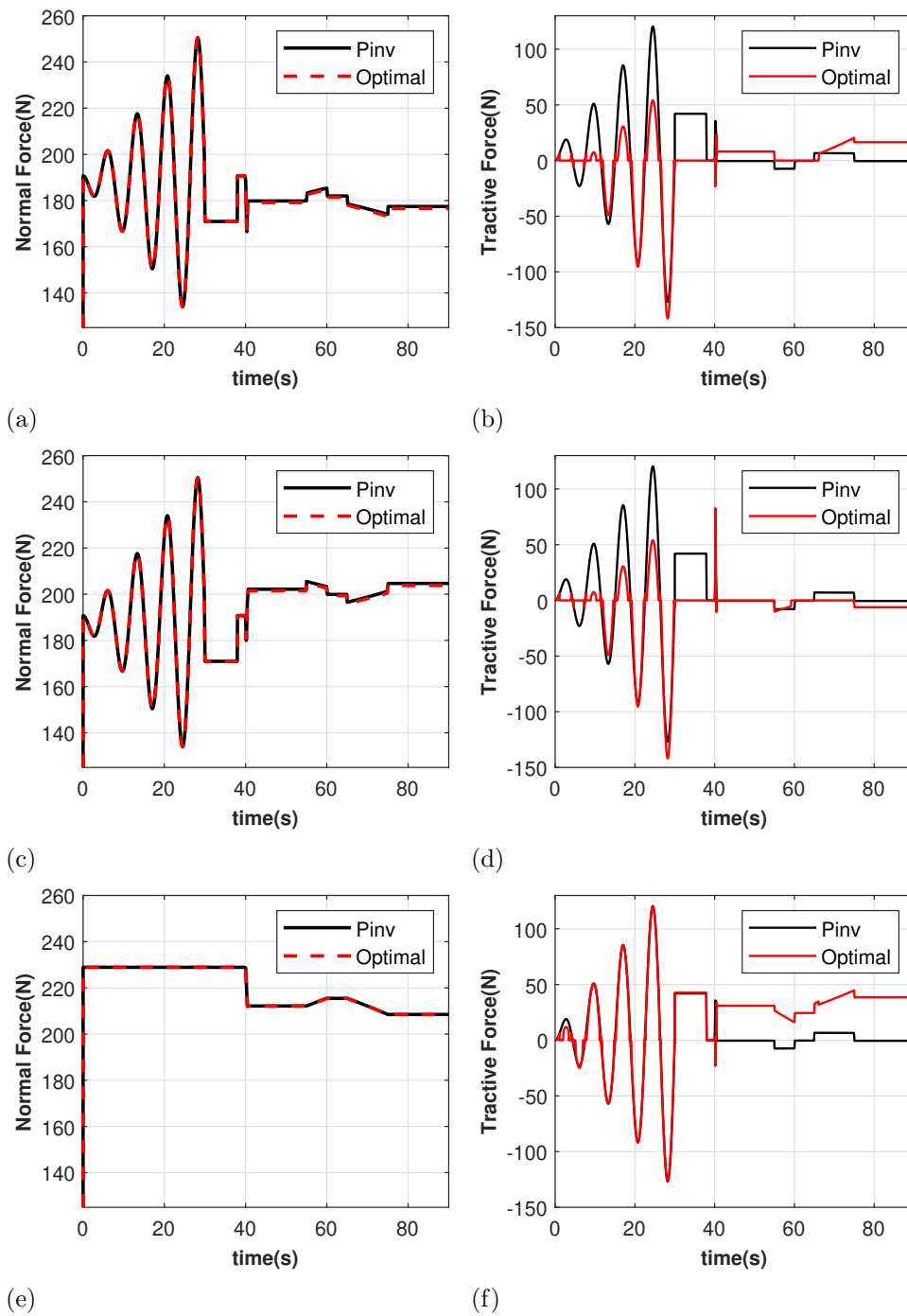


Figure 5.11: Comparison of the generated normal reaction forces and tractive forces in longitudinal direction in both front wheels and port center wheel. Normal reaction forces are depicted in left and longitudinal tractive forces are depicted in right. Sequentially, the rows illustrate the comparison for port front, starboard front, and port center wheels.

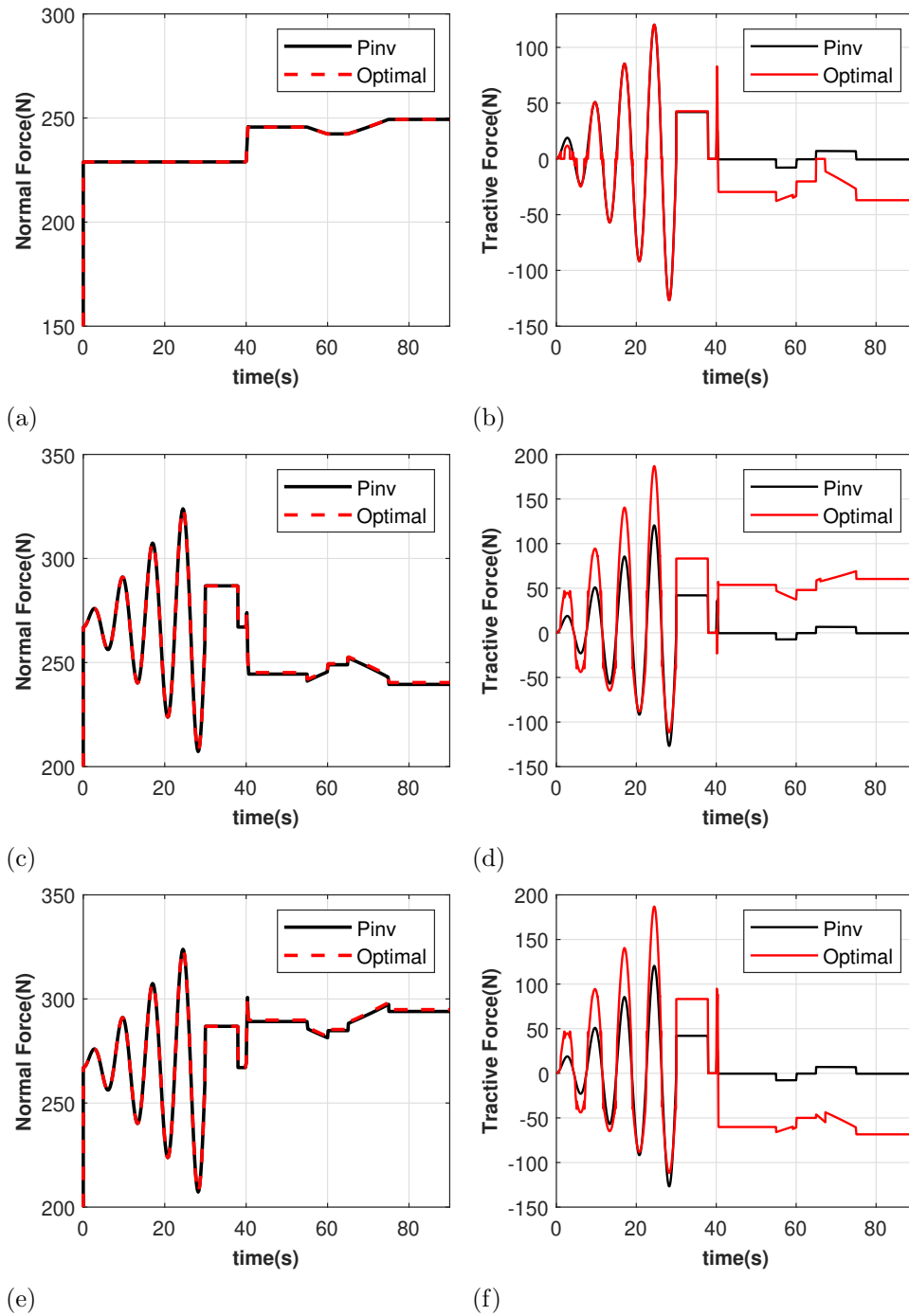


Figure 5.12: Comparison of the generated normal reaction forces and tractive forces in longitudinal direction in both rear wheels and starboard center wheel. Normal reaction forces are depicted in left and longitudinal tractive forces are depicted in right. Sequentially, the rows illustrate the comparison for starboard center, port rear, and starboard rear wheels.

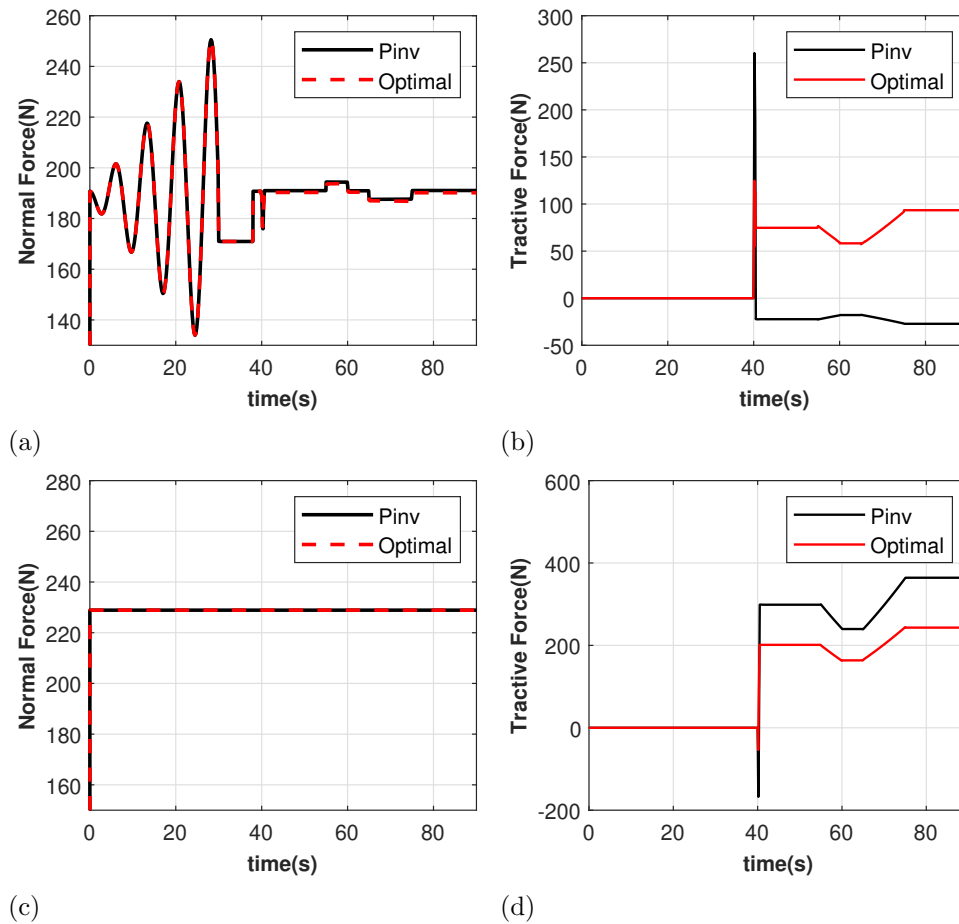


Figure 5.13: Comparison of the generated normal reaction forces and tractive forces in lateral direction in both front wheels and center wheels. Corresponded Normal reaction forces are depicted in left and lateral tractive forces are depicted in right. Sequentially, the rows illustrate the comparison for front and center wheels.

and it is only affected by the forward acceleration/deceleration.

In the first 40 seconds of the simulation, when the system follows an acceleration/deceleration trajectory on a straight line, it can be observed that as the required acceleration of the system's center of mass in the rotational direction is zero, and the lateral tractive forces are not involved in the optimization (they kept equal to zero), system experiences an equal distribution of the longitudinal tractive forces between port and starboard wheels on all axes. In the Pinv solution it can be seen that the whole required tractive force is uniformly distributed between all wheels. However, in Optimal solution in acceleration phase since the normal forces at rear

wheel are higher than front wheel and the difference between them also increases when higher acceleration command is applied, the optimal distribution increases the tractive forces at rear wheels and decreases that of front wheels. On the other hand, during deceleration phase the normal forces at rear wheels gets closer to that of front wheel and the optimal distribution generates almost the same distribution as of the Pinv solution. when the magnitude of the acceleration of the system is very small, based on the proposed projection (to alleviate the wheel fighting) all wheels have very small contributions and in that case I apply no optimal distribution and Pinv solution is considered. When the magnitude of acceleration increases, first the contribution of the tractive forces at front wheels are negative or so small and as it can be observed the proposed projection make them equal to zero and the sub-optimal solution is applied. In higher accelerations all wheels are involved and the optimal solution is applied. Since the normal reaction forces at center wheels remain constant, the optimal approach produces the same tractive forces as Pinv solution (except for the first seconds of the simulation when they contributions is also small and the sub-optimal solution is applied).

When the system starts turning, since the center of mass is close to the main body coordinate frame, in Pinv approach, system puts almost all the weight of lateral tractive forces on the center wheels. However in optimal solution lateral tractive forces are distributed between front and center axes according to the corresponded normal forces and by consideration of the difference between the resultant torque around the center of mass and the required value. This distribution of lateral tractive forces generates a torque that has to be compensated by distributing longitudinal tractive forces between port and starboard wheels. Based on the location of the center of mass, this generated torque is counter clock wise and accordingly the longitudinal tractive forces at port side has to be positive and at the starboard side has to be negative. Based on the second optimization, it can be observed that even such generated longitudinal tractive forces are distributed based on the normal forces. Most of the burden is on the rear wheels particularly on the starboard side. When the system moves with constant velocity, the summation of the total longitudinal tractive forces must be equal to zero since the longitudinal acceleration is zero. When the system accelerates the magnitudes of positive longitudinal forces gets higher and the negative ones gets lower to produce the required acceleration. The opposite pattern can be seen during deceleration. When the system is circling with low velocity since the generated torque

is small, the longitudinal tractive forces at front wheel in Optimal approach becomes so small or even in the opposite direction to the required one. It can be observed that in this case, the projection method gets activated and the sub-optimal solution kills them.

To sum up, Fig.5.14 indicates the root means square of the tractive ratios at all wheels in both longitudinal and lateral directions. It can be observed that during linear motion, at low accelerations when the sub-optimal solution is applied, optimal solution produces almost equal tractive ratios to Pinv. During deceleration also since the normal forces at different axes get closer to each other, Optimal approach produces also the same tractive ratios as Pinv. However a tractive ratios considerably are improved in the Optimal during high accelerations where is of more importance in terms of traction improvement. Particularly, optimal approach saved the system from dynamic friction at 24<sup>th</sup> second.

During circling, clearly optimal improves the tractive ratios in the lateral direction at the expense of increasing tractive ratios at longitudinal direction. Using Pinv, system is close to the verge of traction lost in the lateral direction when the steering command is applied or during circling with high velocity (last 15 seconds). In contrast, applying Optimal I reduced the tractive ratios in lateral directions while the tractive ratios in longitudinal directions are still acceptable.

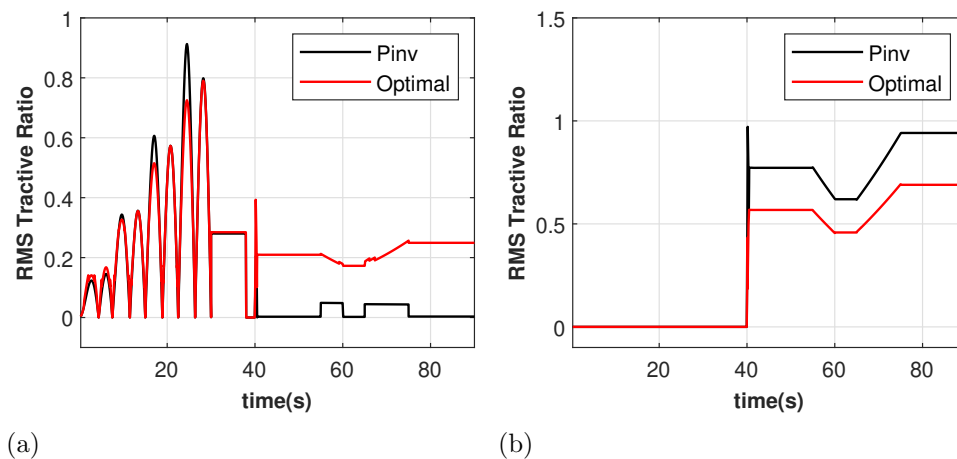


Figure 5.14: The root mean square of the tractive ratios in all wheels. (a) in the longitudinal direction and (b) in the lateral direction

Figures 5.15, 5.16, and 5.17 are comparing the applied control torques to the system in both approaches. As the steering degrees of freedom is dictated by the

desired trajectory, the control torque distribution and any choice from the kernel of the control directions is not affecting the steering torque and it can be seen that both Pinv and Optimal produce the same steering torque command. Uniform distribution of throttle/brake torques in Pinv solution can be observed from 6.7. However, in optimal, such control torques are distributed in a manner to produce the optimal distribution of the tractive forces.

*Remark 5.11.* For simplicity, I did not consider any saturation point in the produce control torque by systems' actuator. As for one future direction of this research, the proposed optimization can get improved by considering torque saturation by adding them as inequality constraints.

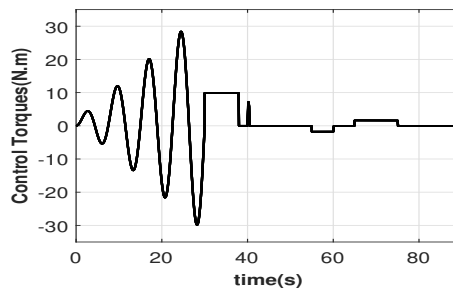


Figure 5.15: Control throttle/brake torques in Pinv

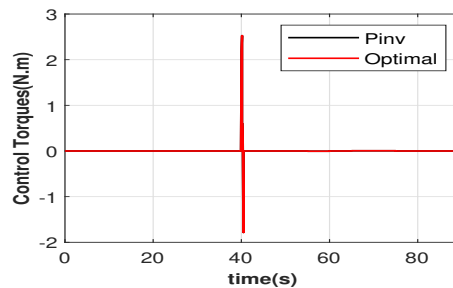
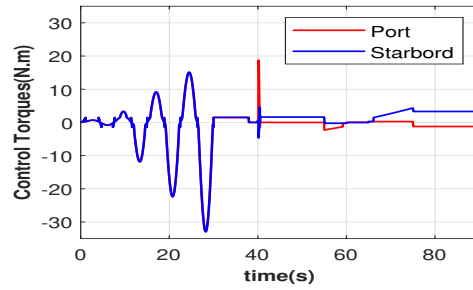


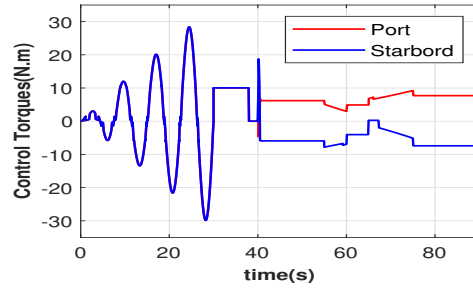
Figure 5.16: Comparison of steering torque in Pinv and Optimal

## 5.7 Experimentation

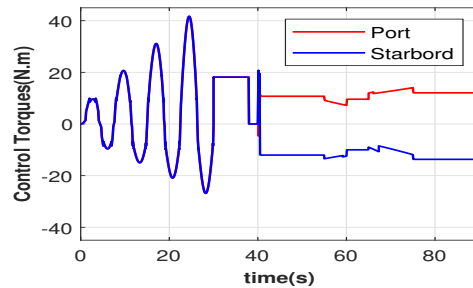
To evaluate the proposed traction optimization algorithm in real-world applications, in this section, I implemented that on a real system modeled in Vortex Studio using



(a)



(b)



(c)

Figure 5.17: Control throttle/brake torques in Optimal: (a) front wheels, (b) center wheels, (c) rear wheels

the developed software in the loop simulation environment. Two separate case studies are considered. For the first case study, I modeled our mechanism and controller with exactly the same parameters as in 5.2 with the same desired trajectory as in MATLAB simulation (Fig. 5.6), and the default values defined in Vortex for tire deformation. The static friction coefficients used in this case study are also the same as in (5.78). Fig. 5.18 compares the root mean square of the tractive ratios in Pinv and Optimal approach for both longitudinal and lateral directions in this case study. As it can be observed from Fig. 5.18 at 24<sup>th</sup> second the root mean square of the longitudinal tractive ratios in Pinv suddenly drops. This indicates that at front wheels the dynamic

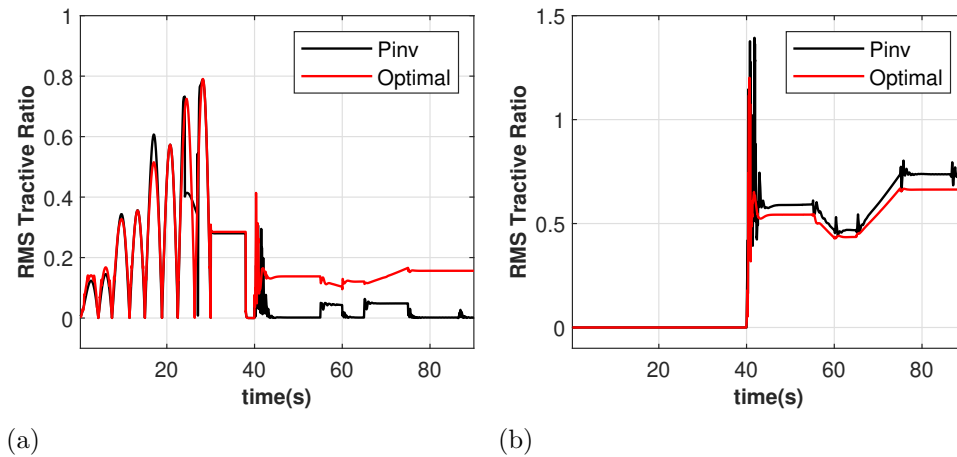


Figure 5.18: Tractive ratios at all wheels for case study 1: (a) longitudinal direction, (b) lateral direction

friction regime has begun but applying the optimal distribution I have saved the system and traction is maintained. When the steering command is applied and when the acceleration profile is changed during circling, it can be observed that in Pinv approach system gets closer to the verge of traction lost in lateral direction. That can be observed by the peaks at  $40^{th}$ ,  $55^{th}$ ,  $60^{th}$ ,  $65^{th}$ , and  $75^{th}$  seconds of the simulation. However traction is maximized applying the Optimal solution.

Although our controller is established on the assumption of ideal nonholonomic constraints, but since the look-ahead point is affected by the steering, loosing traction at some wheels will change the tractive forces and that may result in a disturbance applied at steering. With that being mentioned, it can be seen from Fig.5.19 that the error seen by the controller is slightly affected when traction is lost in Pinv. Otherwise, this figure shows that the error seen by the controller is almost the same in both approaches and that validate the fact that the optimal distribution is not affecting the dynamics of the system and tracking performance of the controller.

Finally the actual path that the system passed in both approaches are compared with the desired path in Fig.5.20. As it can be observed the path generated by the Optimal solution is closer to the desired trajectory.

For the second case study I reduce the tire deformation and increase the damping at tires from default value equal to 0.3 to 0.4 to improve the estimation of the lateral tractive forces. Consequently, I made the parameter  $\nu = 1$ . I also increase the friction



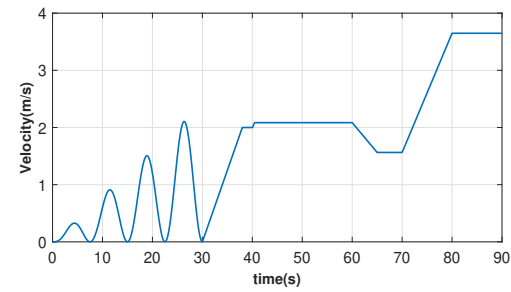
and change the center of mass of the main body to put the total center of mass of the system at the origin of the main body frame. Table.5.3 shows the parameter used in this case study.

Rover Parameters			
$L$ [m]	$L_0$ [m]	$c$ [m]	$R_w$ [m]
1	0.5	0.55	0.2
$l$ [m]	$x_{cm}$ [m]	$y_{cm}$ [m]	$m_r$ [Kg]
1	-0.0667	0	600
$m_w$ [Kg]	$J_r$ [Kg/m <sup>2</sup> ]	$J_{wy}$ [Kg/m <sup>2</sup> ]	$J_{wz}$ [Kg/m <sup>2</sup> ]
40	450	1	1
$g_u$ [m/s <sup>2</sup> ]			
1.632			
Suspension Spring Constants			
$k_f$ [N/m]	$k_c$ [N/m]	$k_r$ [m/s]	
30000	45000	60000	
Controller and Traction Optimization Parameters			
$K_p$	$K_I$	$K_d$	$v$
48	64	12	1

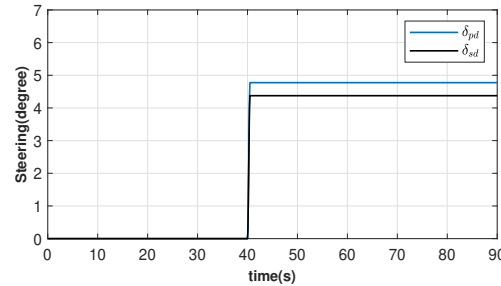
Table 5.3: Kinematic and dynamic parameters of the Lunar rover, suspension spring constants and design parameters defined in the simulation, in case study 2

Since the friction coefficients are increased I also change the desired trajectory to have more intense accelerations commands. Such desired trajectory can be seen in Fig.5.21.

Fig.5.22 compares the tractive ratios in both lateral and longitudinal directions using Pinv and Optimal approaches. As it can be observed, during motion on a straight line even the projected sub-optimal solution at small accelerations shows a better longitudinal traction than Pinv solution. The reasons are the higher friction coefficients and more difference between the normal forces at front and rear wheels by closing the center of mass to the rear wheels. In this case study, not only Optimal approach saved the system from traction lost in longitudinal direction at 24<sup>th</sup> second, but also it saved the system from lateral traction lost in 75<sup>th</sup> second of the simulation. It can be observed from Fig.5.23 that in Pinv, system completely drifted from its path

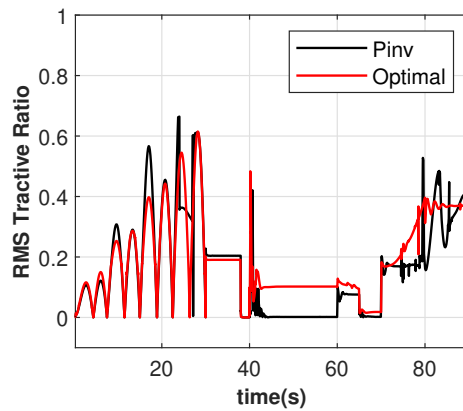


(a)

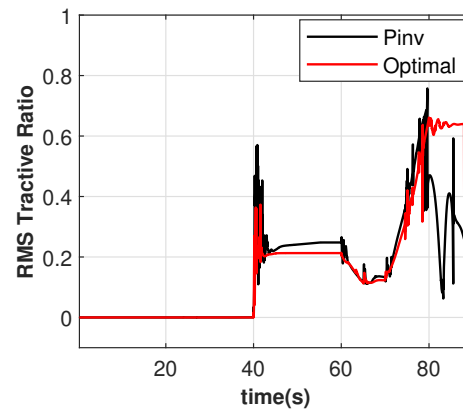


(b)

Figure 5.21: Desired trajectory in case study 2: (a) desired velocity, (b) desired steering



(a)



(b)

Figure 5.22: Tractive ratios at all wheels for case study 2: (a) longitudinal direction, (b) lateral direction

and it is unable to keep itself on the desired trajectory, however this is not seen in the optimal approach and system successfully followed the desired trajectory.

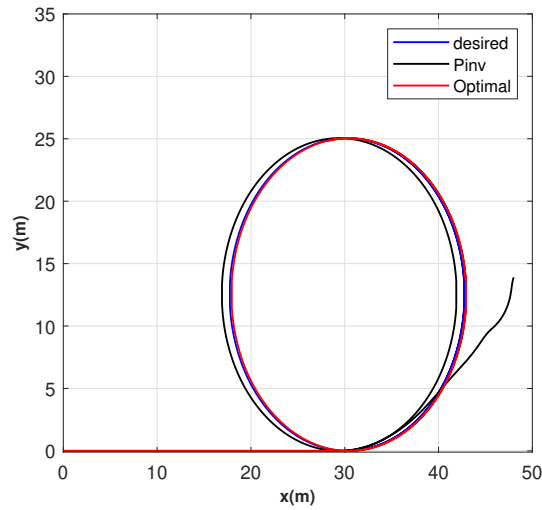


Figure 5.23: Comparison between the generated path by Pinv, Optimal, and the desired path in case study 2

## 5.8 Summary

In this chapter, an optimal distribution of control actions for constrained systems containing redundant control directions was introduced to enhance the force/moment environmental interaction of the system, without affecting the tracking performance. Such an optimal distribution was then employed in traction improvement of autonomous rover/vehicle systems. The optimization algorithm was developed such that (i) the necessary optimality condition was linear, (ii) the direction of tractive forces was considered, and (iii) among terramechanic parameters, only static friction coefficients were required for the wheel-ground interaction model. The estimation of tractive and normal forces exploited in the optimization cost function were compared to the values obtained from the developed software-in-the-loop simulation including the digital-twin model of the system and the results demonstrated an acceptable match. Finally, the efficacy of the proposed traction optimization algorithm was compared to the conventional pseudo-inverse solution using both MATLAB and Vortex simulations. The results showed that the proposed traction controller leads to a meaningful improvement in dynamic traction of the system.

## Chapter 6

# Robust Dynamic Traction Control

### 6.1 Overview

In this chapter, the proposed robust output-tracking control law in Chapter 4 and the traction optimization algorithm in Chapter 5 are integrated to develop a robust output-tracking for autonomous rovers with dynamic traction control. Firstly, I show that the output-tracking control law is independent of the restricted dynamic model used in its development, considering some or all of the holonomic constraints. Hence, I can employ different restricted models of the system for the output-tracking controller and the optimal control distribution. Secondly, the approximation of normal reaction forces and tractive forces in traction optimization is improved by designing a disturbance observer, under some explained assumptions. This observer is designed in the time domain and its convergence to the actual lumped effects of uncertainties is proved. Finally, the validity of the disturbance observer and the efficacy of the proposed control scheme are investigated using the developed simulation environment in MATLAB.

### 6.2 Robust Output-tracking Traction Control

To design an output-tracking controller with optimal dynamic traction that is robust against disturbances, the control law proposed in (5.8) for an optimal  $\boldsymbol{\tau}_a$ , obtained in Chapter 5, must be used along with the SMC in (4.14). Since I assume an undisturbed system model to approximate the normal reaction and tractive forces during the traction optimization, an observer is required to capture the effects of disturbances. Otherwise, I compromise the performance of the dynamic traction control, under

large external disturbances.

In Chapter 4, the control law in (4.14) is developed based on the system model in the configuration manifold resulted from integrating all holonomic constraints, here denoted by  $Q_1$ . However in Chapter 5, only the dynamics on a partially integrated configuration manifold (including non-tractive holonomic constraints), denoted by  $Q_2$ , is considered to perform the traction optimization. In this model, all linearly independent tractive forces can be estimated using (5.14). Let us denote the projected matrix of control directions on  $Q_1$  and  $Q_2$  by  $B_{r_1}$  and  $B_{r_2}$ , respectively. If  $\ker(B_{r_2}) \subseteq \ker(B_{r_1})$ , the controller design and the traction optimization can be performed independently. In other words, the pseudo-inverse solution of (3.12) and the optimal  $\boldsymbol{\tau}_a$  can be calculated using two separate descriptions of the system, since any optimal control distribution does not affect the output performance.

**Proposition 6.1.** *For the matrices  $B_{r_1}$  and  $B_{r_2}$  defined as above,  $\ker(B_{r_2}) \subseteq \ker(B_{r_1})$ .*

*Proof.* Let us denote the Jacobian of the inclusion map from  $Q_2$  to  $\hat{Q}$  by  $J_2$  and the Jacobian of the inclusion map from  $Q_2$  to  $Q_1$  by  $J_1$ .  $Q_1$  is assumed to be obtained by two consecutive restrictions: (i) restricting by non-tractive holonomic constraints, and (ii) by restricting the remaining tractive holonomic constraints. The constraint matrix on  $Q_2$  is obtained by (3.4) as  $A_2 = E_2 \hat{A} J_2$  and that on  $Q_1$  is  $A_1 = E_1 E_2 \hat{A} J_2 J_1$ , where matrices  $E_1$  and  $E_2$  are only parameterizing constant matrices. Let us denote matrices whose columns span  $\ker(A_1)$  and  $\ker(A_2)$  by  $N_1$  and  $N_2$ . Accordingly I have

$$E_1 E_2 \hat{A} J_2 J_1 N_1 = 0. \quad (6.1)$$

Consequently,  $\text{im}(J_1 N_1) \subseteq \text{im}(N_2)$ , and hence,  $\ker(N_2^T) \subseteq \ker((J_1 N_1)^T)$ . In addition, based on (3.6) and (3.8), it can be deduced that  $B_{r_2} = N_2^T J_2^T \hat{B}$  and  $B_{r_1} = N_1^T J_1^T J_2^T \hat{B}$ , and this completes the proof. ■

**Assumption 6.1.** For simplicity, in this chapter I assume that system is only subject to the sources of disturbances in the form of unknown applied external forces and the inertia parameters are completely known.

Let us introduce a vector  $\mathbf{d} \in \mathbb{R}^b$  whose components are the lumped effect of external disturbances on the corresponding components of the output. In this case,

the uncertain error dynamics of the output under the introduced input-output linearization feedback in (4.13) becomes

$$\ddot{\mathbf{e}} = \mathbf{v} + \mathbf{d}, \quad (6.2)$$

where the control law  $\mathbf{v}$  is designed in Chapter 4 to asymptotically stabilize the output error while it is robust against the uncertain term  $\mathbf{d}$  (I assume that  $\mathbf{d} < \epsilon_2$ ). Since the error is asymptotically stable and the input-output dynamics is decoupled at different input channels due to input-output linearization, the vector  $\mathbf{d}$  can be estimated by extending the results of [3]. The proposed observer in [3] is designed for SISO nonlinear systems. The idea is to estimate  $\mathbf{d}$  from the control input  $\mathbf{v}$  by embedding the not perturbed input-output dynamics of the system as an auxiliary system in the control loop.

Let us denote the input of this auxiliary system by  $\mathbf{h}_o \in \mathbb{R}^b$  and the output of that by  $\mathbf{e}_2 \in \mathbb{R}^b$ . While the system is not perturbed the input-output map is a double integrator, i.e.

$$\begin{aligned} \dot{\mathbf{e}}_2 &= \int_0^t \mathbf{h}_o(\tau) d\tau, \\ \mathbf{e}_2 &= \int_0^t \left( \int_0^\tau \mathbf{h}_o(\tau_1) d\tau_1 \right) d\tau. \end{aligned} \quad (6.3)$$

**Proposition 6.2.** *Introducing a positive definite diagonal matrix  $K_o \in \mathbb{R}^{b \times b}$  whose components are very large, if*

$$\mathbf{h}_o = K_o(\dot{\mathbf{e}} - \dot{\mathbf{e}}_2), \quad (6.4)$$

$$\hat{\mathbf{d}} = \mathbf{h}_o - \mathbf{v}, \quad (6.5)$$

*then,  $\hat{\mathbf{d}}$  is an estimation of  $\mathbf{d}$  with a small difference.*

*Proof.* From (6.4) it can be deduced that

$$\dot{\mathbf{e}} = K_o^{-1} \mathbf{h}_o + \dot{\mathbf{e}}_2. \quad (6.6)$$

Differentiating (6.6) with respect to time I have

$$\ddot{\mathbf{e}} = K_o^{-1} \dot{\mathbf{h}}_o + \ddot{\mathbf{e}}_2. \quad (6.7)$$

As  $\dot{\mathbf{e}}$ , and  $\ddot{\mathbf{e}}$  are bounded,  $\mathbf{h}_o$ , and  $\dot{\mathbf{h}}_o$  are bounded and since the components of  $K_o^{-1}$

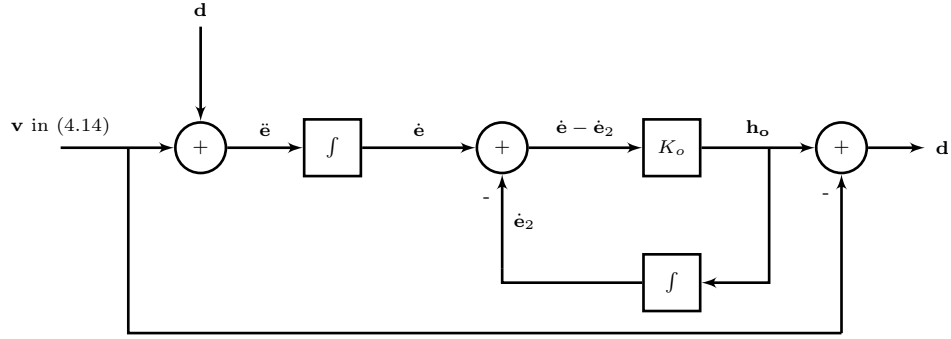


Figure 6.1: Block Diagram of the proposed observer

are very small, I can neglect the term  $K_o^{-1}\dot{\mathbf{h}}_o$ . Substituting  $\ddot{\mathbf{e}}$  by (6.2) and  $\ddot{\mathbf{e}}_2$  by (6.3)

$$\begin{aligned} \mathbf{v} + \mathbf{d} &= \mathbf{h}_o, \\ \Rightarrow \hat{\mathbf{d}} &= \mathbf{h}_o - \mathbf{v} \approx \mathbf{d}. \end{aligned} \quad (6.8)$$

■

The block diagram of the proposed observer can be seen in Fig.6.1. Now that the vector  $\mathbf{d}$  is estimated, it can be used in the traction optimization algorithm to improve the estimation of normal forces and tractive forces based on the following assumption.

**Assumption 6.2.** I assume that system subjects only to one source of disturbance force with known direction, denoted by  $\hat{J}_d$ .

*Remark 6.1.* The vector  $\mathbf{d}$  only considers the projected lumped effect of disturbances on the output that has to be lifted to the space of generalized forces to estimate tractive and normal forces based on (5.13) and (5.15). Accordingly, the designed observer based on the input output map is not helpful if the direction of the disturbance forces are unknown or system is subject to multiple sources of disturbances. Consequently, such observer design has to be enhanced for more realistic scenarios and that is a future direction of this research.

The relationship between  $\mathbf{d}$  and the magnitude of the applied disturbance force, denoted by  $\varpi$ , based on (4.12) is

$$\mathbf{d} = P_d \varpi, \quad (6.9)$$

where

$$P_d := FM_r^{-1}N^T J^T J_d^T.$$

Consequently  $\omega$  can be determined by the pseudo-inverse solution as

$$\omega = P_d^T (P_d P_d^T)^{-1} \mathbf{d}. \quad (6.10)$$

Now (5.13) can be updated to include the estimated disturbance

$$\lambda(\mathbf{q}, \dot{\mathbf{q}}, \boldsymbol{\tau}) = -(AM^{-1}A^T)^{-1} \left( AM^{-1}(-C\dot{\mathbf{q}} + B\boldsymbol{\tau} + J_d^T \omega) + \dot{A}\dot{\mathbf{q}} \right), \quad (6.11)$$

and give a better approximation of tractive forces. As entering the observed disturbance force into the estimation of normal reaction forces is dependent on the structure of the system and the direction of the disturbance, it is discussed in more detail in the implementation section.

It is also noteworthy that this observed disturbance force can also be considered during the calculation of the total required force at systems center of mass  $\mathbf{h}$ . That is, (5.23) needs to be updated to include the estimated disturbance.

$$\mathbf{h} := J_c^T M(\dot{N}\boldsymbol{\eta} + NM_r^{-1}(B_r\boldsymbol{\tau}_{\parallel} + N^T J_d^T \omega - C_r\boldsymbol{\eta})) + J_c^T C\dot{\mathbf{q}} - J_c^T J_d^T \omega. \quad (6.12)$$

### 6.3 Implementation on a Six-wheel Lunar Rover

I consider the applied external disturbance force as the friction force applied to rear wheels. Accordingly  $J_d = J^T \hat{J}_d$  where  $J$  is the Jacobian of the inclusion map after integrating holonomic constraints and  $\hat{J}_d$  is defined in (4.45). In addition the estimations of normal reaction forces can be improved by redefining the vector  $\mathbf{k}$  in (5.70) and adding  $-R_w\omega$  to the third component.

The combination of the robust output tracking control law and traction optimization algorithm along with the developed disturbance observer is evaluated using the simulation platform developed in MATLAB. The inertia and geometric parameters and parameters involved in traction optimization, used in the simulation are same as Table.5.2, and the controller parameter is same as Table.4.1. All uncertain terms are equal to zero except for the one related to the lateral friction at rear wheels which is specified as  $70N$ . The observer gain in (6.4) is also defined as  $K_o = 10\mathbb{I}_{2 \times 2}$ .

*Remark 6.2.* During motion on a straight line in contrast to what is expected  $\mathbf{d} \neq 0$ ,

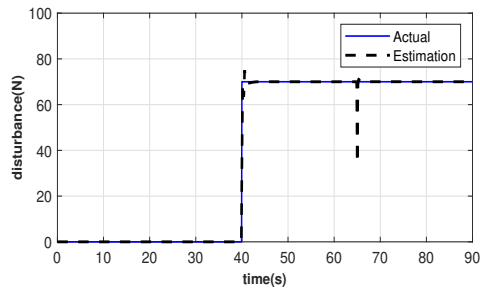


Figure 6.2: Comparison of the actual and estimated lateral disturbance force at rear wheels

due to the numerical error. Additionally, the matrix  $J_d$  is rank deficient on such trajectories. These two result in a spike in estimation of  $\hat{\omega}$  using (6.10). To resolve this issue I applied the singular value decomposition proposed in Section 5.3.2 to (6.10).

I consider the desired trajectory same as Fig.5.6, and the results are depicted in the following figures. Fig.6.2 compares the actual values I defined for the disturbance applied at rear wheels and what I estimate at the observer. As it can be observed, I have a good estimation of the disturbance force applied as the lateral friction at rear wheels. The peak appears at 65<sup>th</sup> second of the simulation is due to the numerical error appears at  $\mathbf{d}$  when the sudden acceleration command is applied and the projection of that onto the disturbance at rear wheels. Fig 6.3 shows what happens if the applied

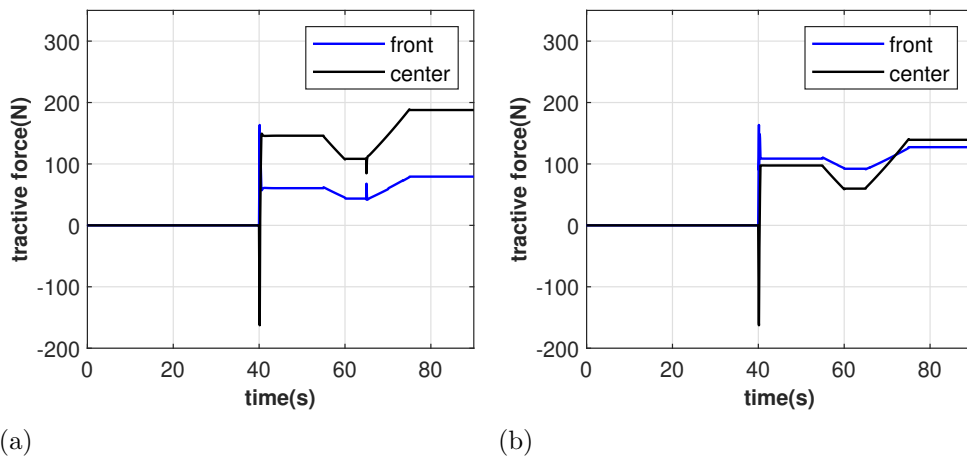


Figure 6.3: Comparison of the distribution of lateral tractive forces in Optimal with (left) and without (right) disturbance observer

disturbance is not considered in the traction optimization. As it can be observed from the right figure, the controller is not sensing the applied force at rear wheel and produce the same amount of lateral tractive forces at front wheels as no disturbance is applied. In the large portion of the simulation time the produced lateral tractive force at front wheels is even higher than that of center wheels, although I know that center wheels are experiencing higher normal reaction forces and the traction optimization algorithm is actually deteriorating traction. However, when the observer is designed and the effect of disturbances is considered, the lateral tractive forces are distributed between front and center axes with respect to the generated normal reaction forces. The remaining plots are comparing the distribution of longitudinal, and lateral tractive forces and the normal reaction forces along with the control inputs to the system. The reason why chattering effects do not appear in the produced control actions is that a constant force is considered as the perturbation. Since the designed sliding manifold contains an integral term, this term completely addressed the applied constant disturbance force.

## 6.4 Summary

In this chapter, the robust output-tracking control law developed in Chapter 4 was combined with the traction optimization algorithm proposed in Chapter 5. I showed that the design of the robust output-tracking control law and the determination of the optimal control distribution were independent. Under some explained assumptions, an observer was proposed to improve the estimations of normal and tractive forces, and its convergence to the actual disturbance force was proved. This observer is implementable on multi-input-multi-output input-output linearizable nonlinear systems and since it is designed in time domain, it is needless of low-pass filters. Simulation results showed an acceptable match between the output of the observer and the actual applied disturbances. Additionally, it was demonstrated that not considering the effect of disturbances in the traction optimization algorithm led to a wrong distribution of control actions, which could be resolved by employing the developed observed.

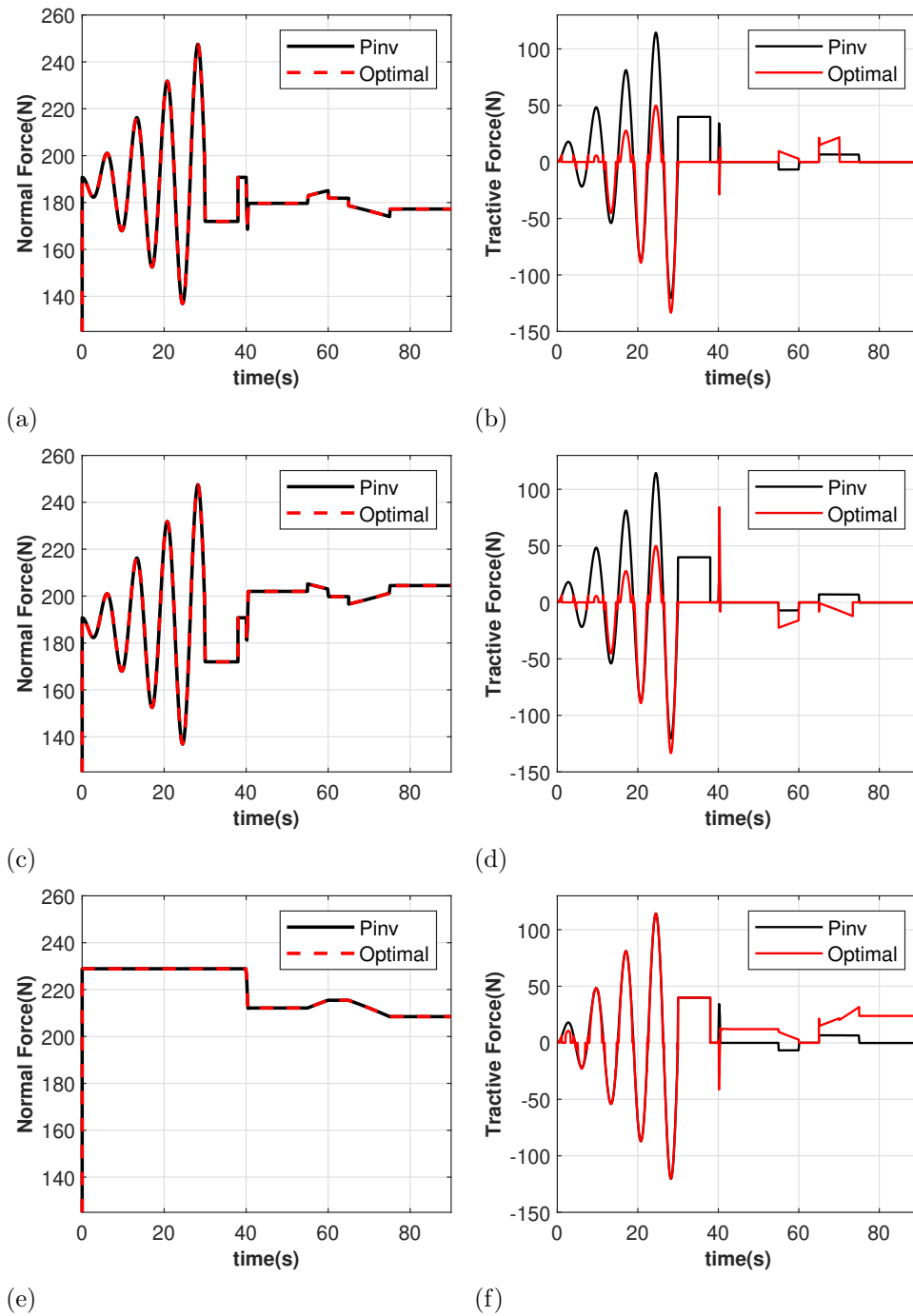


Figure 6.4: Comparison of the generated normal reaction forces and tractive forces in longitudinal direction in both front wheels and port center wheel applying robust traction controller. Normal reaction forces are depicted in left and longitudinal tractive forces are depicted in right. Sequentially, the rows illustrate the comparison for port front, starboard front, and port center wheels.

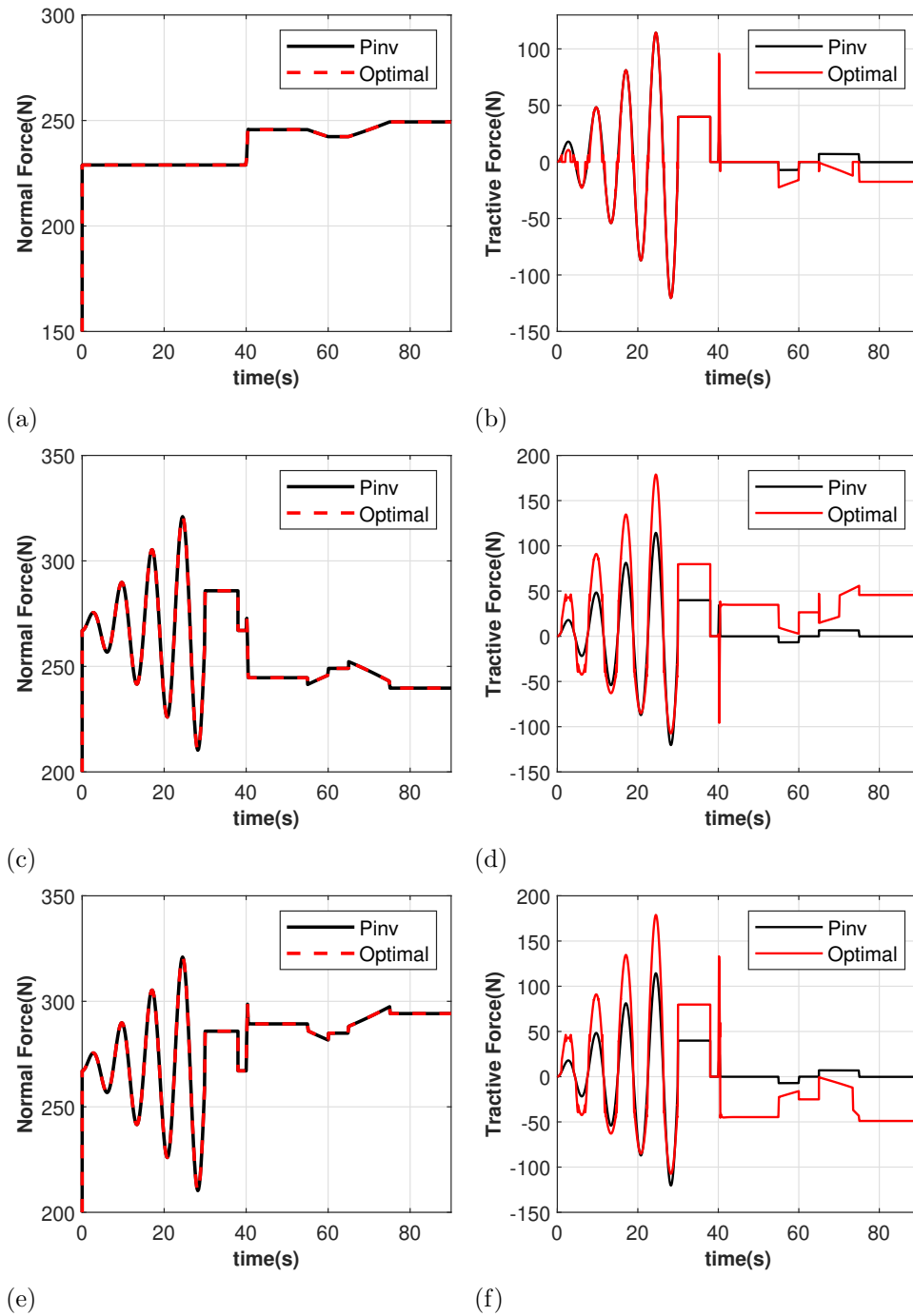


Figure 6.5: Comparison of the generated normal reaction forces and tractive forces in longitudinal direction in both rear wheels and starboard center wheel applying robust traction controller. Normal reaction forces are depicted in left and longitudinal tractive forces are depicted in right. Sequentially, the rows illustrate the comparison for starboard center, port rear, and starboard rear wheels.

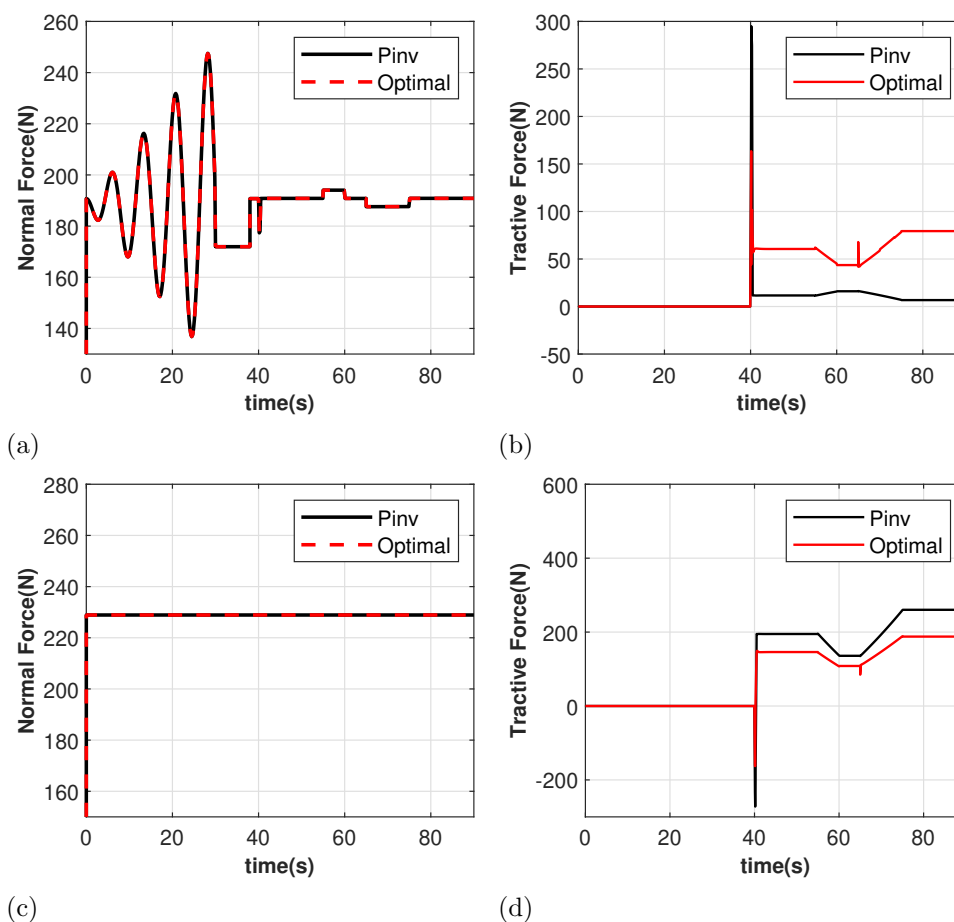


Figure 6.6: Comparison of the generated normal reaction forces and tractive forces in lateral direction in both front wheels and center wheels applying robust traction controller. Corresponded Normal reaction forces are depicted in left and lateral tractive forces are depicted in right. Sequentially, the rows illustrate the comparison for front and center wheels.

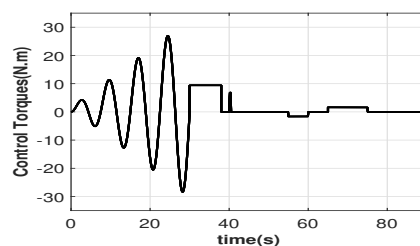


Figure 6.7: Control throttle/brake torques in Pinv robust control

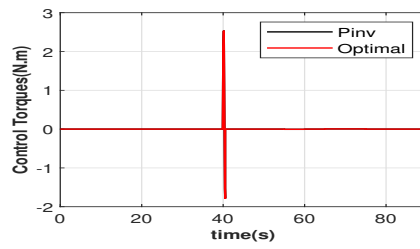
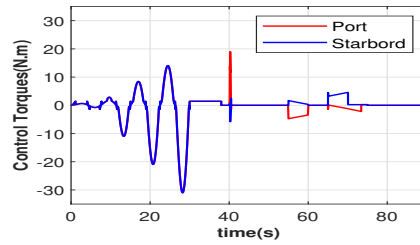
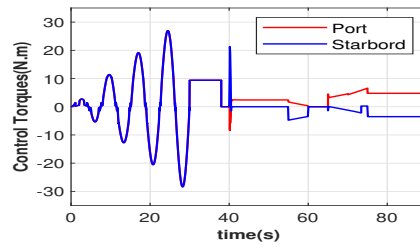


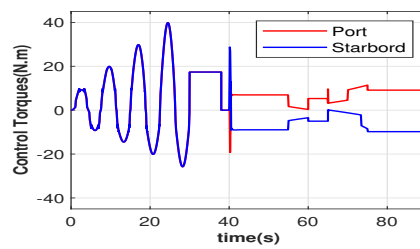
Figure 6.8: Comparison of steering torque in Pinv and Optimal Traction



(a)



(b)



(c)

Figure 6.9: Control throttle/brake torques in optimal robust traction control: (a) front wheels, (b) center wheels, (c) rear wheels

## Chapter 7

# Conclusions and Future Directions

In this thesis, a robust output-tracking control law for autonomous rover systems along with an optimal distribution of control actions with the aim of improving dynamic traction were proposed. First a class of mechanical control systems subject to mixed holonomic and nonholonomic constraints in Pfaffian form was considered and the reduced projected state space representation of such systems in their holonomically restricted configuration manifold was determined. I showed that such systems are fully locally reachable, not full-state feedback linearizable, and input-output linearizable applying static feedback if the input-output decoupling matrix is everywhere invertible. Under the input-output linearizability assumption, the internal-external state decomposition was discussed. Furthermore, I proposed an observability decomposition of the internal states used in the stability analysis of the internal dynamics. Then, an uncertain error dynamics of the system's output was developed and asymptotically stabilized by proposing a SMC strategy. Our developed SMC contains optimally designed sliding manifold and it is applicable to the systems with complex dynamics subject to bounded time-dependent complex matched uncertainties. The developed control law was used in the output-tracking control of a six-wheel autonomous Lunar rover, in a simulation environment. The results were compared with those obtained using the optimal PID control strategy. I showed that although the optimal PID demonstrated an acceptable performance in terms of both error and control actions, the addition of the proposed switching control law improved the error performance by one order of magnitude without considerably affecting the control actions.

In the second phase, the redundant control directions were exploited to design a dynamic traction control strategy for autonomous rovers/vehicles systems. Under

some explained assumptions, the tractive and normal reaction forces were computed and used in the definition of an optimization cost function. I designed this cost function in a manner that (i) the necessary condition of optimality became linear, (ii) the directions of the tractive forces were considered, and (iii) the required information about wheel-ground dynamics was minimal. The proposed dynamic traction controller was implemented on the six-wheel autonomous Lunar rover studied in the previous phase. A software-in-the-loop simulation environment was developed based on a high-fidelity 3-dimensional model of the system in Vortex Studio that captured realistic wheel-ground interactions and tire models. The MATLAB simulation of the system and estimation of normal and tractive forces were validated using this digital twin of the system. The MATLAB and software-in-the-loop simulation results demonstrated meaningful improvement in the dynamic traction of rover systems with high velocities and accelerations. The traction control strategy was able to save the system from traction loss in multiple occasions.

In the last phase, the robust output-tracking control law developed in the first phase and the dynamic traction controller proposed in the second phase were integrated. Firstly, I showed that different models of the system could be employed in the design of the robust output-tracking control law and the traction optimization algorithm. Under some explained assumptions, I proposed an observer to improve the estimation of normal forces and tractive forces used in the traction optimization. This observer is applicable to the MIMO input-output linearizable nonlinear systems and since it is designed in the time domain, it is needless of low-pass filters. Simulation results indicated the validity of the observed lumped effect of the disturbances on the output of the system and the improvement in the traction optimization considering such observations in the defined cost function.

A possible future direction of this research is developing a gain-scheduling technique instead of employing switching control law, to ensure robustness of the output tracking control. The resulting controller captures the effect of the trajectory on the uncertain terms that leads to a robust chattering-free output-tracking control with small gains. In addition, the proposed traction optimization algorithm can be enhanced by considering the actuators' saturation as inequality constraints during optimization. Traction can also be considered during path planning phase. Using optimal control theory, a trajectory from an initial state to a terminal state can be determined in which a quadratic norm of the vector of tractive ratios gets minimized.

Finally, the proposed observer can be improved by capturing the lumped effect of the disturbances at generalized force level instead of the output level. This way, the estimation of tractive forces can be performed while the system is subject to more than one sources of uncertainties with unknown directions.

## List of References

- [1] A. M. Bloch, “Nonholonomic mechanics and control,” Springer, 2003.
- [2] T. Peynot and S. Lacroix, “Enhanced locomotion control for a planetary rover,” in *Proceedings 2003 IEEE/RSJ International Conference on Intelligent Robots and Systems (IROS 2003)*(Cat. No. 03CH37453), vol. 1, pp. 311–316, IEEE, 2003.
- [3] S. Ding, W.-H. Chen, K. Mei, and D. J. Murray-Smith, “Disturbance observer design for nonlinear systems represented by input–output models,” *IEEE Transactions on Industrial Electronics*, vol. 67, no. 2, pp. 1222–1232, 2019.
- [4] B. He, S. Wang, and Y. Liu, “Underactuated robotics: a review,” *International Journal of Advanced Robotic Systems*, vol. 16, no. 4, p. 1729881419862164, 2019.
- [5] R. M. Murray, Z. Li, S. S. Sastry, and S. S. Sastry, *A mathematical introduction to robotic manipulation*. CRC press, 1994.
- [6] B. Siciliano, L. Sciavicco, L. Villani, and G. Oriolo, *Robotics: modelling, planning and control*. Springer Science & Business Media, 2010.
- [7] A. Van der Schaft and B. Maschke, “On the hamiltonian formulation of non-holonomic mechanical systems,” *Reports on mathematical physics*, vol. 34, no. 2, pp. 225–233, 1994.
- [8] J. Kovecses, J.-C. Piedboeuf, and C. Lange, “Dynamics modeling and simulation of constrained robotic systems,” *IEEE/ASME Transactions on mechatronics*, vol. 8, no. 2, pp. 165–177, 2003.
- [9] X. Yun and N. Sarkar, “Unified formulation of robotic systems with holonomic and nonholonomic constraints,” *IEEE Transactions on Robotics and Automation*, vol. 14, no. 4, pp. 640–650, 1998.
- [10] M. De Leon, “A historical review on nonholonomic mechanics,” *Revista de la Real Academia de Ciencias Exactas, Fisicas y Naturales. Serie A. Matematicas*, vol. 106, no. 1, pp. 191–224, 2012.
- [11] J. I. Ne\_emark and N. A. Fufaev, *Dynamics of nonholonomic systems*, vol. 33. American Mathematical Soc., 2004.
- [12] E. Jarzebowska, “Dynamics modeling of nonholonomic mechanical systems: theory and applications,” *Nonlinear Analysis: Theory, Methods & Applications*, vol. 63, no. 5-7, pp. e185–e197, 2005.

- [13] M. de León, J. C. Marrero, and D. M. de Diego, “Mechanical systems with nonlinear constraints,” *International journal of theoretical physics*, vol. 36, no. 4, pp. 979–995, 1997.
- [14] I. Kolmanovsky and N. McClamroch, “Developments in nonholonomic control problems,” *IEEE Control Systems Magazine*, vol. 15, no. 6, pp. 20–36, 1995.
- [15] A. Bloch and N. McClamroch, “Control of mechanical systems with classical nonholonomic constraints,” in *Proceedings of the 28th IEEE Conference on Decision and Control*, pp. 201–205 vol.1, 1989.
- [16] G. Walsh, D. Tilbury, S. Sastry, R. Murray, and J. Laumond, “Stabilization of trajectories for systems with nonholonomic constraints,” *IEEE Transactions on Automatic Control*, vol. 39, 1994.
- [17] Z.-P. Jiang and H. Nijmeijer, “A recursive technique for tracking control of nonholonomic systems in chained form,” *IEEE Transactions on Automatic Control*, vol. 44, no. 2, pp. 265–279, 1999.
- [18] N. Sarkar, X. Yun, and V. Kumar, “Control of mechanical systems with rolling constraints: Application to dynamic control of mobile robots,” *The International Journal of Robotics Research*, vol. 13, no. 1, pp. 55–69, 1994.
- [19] R. Chhabra and M. R. Emami, “A unified approach to input-output linearization and concurrent control of underactuated open-chain multi-body systems with holonomic and nonholonomic constraints,” *Journal of Dynamical and Control Systems*, vol. 22, pp. 129–168, 2016.
- [20] R. Chhabra, M. R. Emami, and Y. Karshon, “Reduction of hamiltonian mechanical systems with affine constraints: A geometric unification,” *Journal of Computational and Nonlinear Dynamics*, vol. 12, no. 2, 2017.
- [21] R. Chhabra, “Dynamical reduction and output-tracking control of the lunar exploration light rover (lelr),” in *2016 IEEE Aerospace Conference*, pp. 1–8, IEEE, 2016.
- [22] P. Dorato, “A historical review of robust control,” *IEEE Control Systems Magazine*, vol. 7, no. 2, pp. 44–47, 1987.
- [23] I. R. Petersen and R. Tempo, “Robust control of uncertain systems: Classical results and recent developments,” *Automatica*, vol. 50, no. 5, pp. 1315–1335, 2014.
- [24] H. K. Khalil and J. W. Grizzle, *Nonlinear systems*, vol. 3. Prentice hall Upper Saddle River, NJ, 2002.
- [25] R. Freeman and P. V. Kokotovic, *Robust nonlinear control design: state-space and Lyapunov techniques*. Springer Science & Business Media, 2008.
- [26] E. Tahoumi, F. Plestan, M. Ghanes, and J.-P. Barbot, “New robust control schemes based on both linear and sliding mode approaches: Design and application to an electropneumatic actuator,” *IEEE Transactions on Control Systems Technology*, 2019.

- [27] E. Kayacan and J. Peschel, “Robust model predictive control of systems by modeling mismatched uncertainty,” *IFAC-PapersOnLine*, vol. 49, no. 18, pp. 265–269, 2016. 10th IFAC Symposium on Nonlinear Control Systems NOLCOS 2016.
- [28] J. Xu, Y. Du, Y.-H. Chen, and H. Guo, “Optimal robust control design for constrained uncertain systems: a fuzzy-set theoretic approach,” *IEEE Transactions on Fuzzy Systems*, vol. 26, no. 6, pp. 3494–3505, 2018.
- [29] Y. Wu, A. Isidori, and R. Lu, “Output regulation of invertible nonlinear systems via robust dynamic feedback-linearization,” *IEEE Transactions on Automatic Control*, 2021.
- [30] L. Le-Tien and A. Albu-Schäffer, “Robust adaptive tracking control based on state feedback controller with integrator terms for elastic joint robots with uncertain parameters,” *IEEE Transactions on Control Systems Technology*, vol. 26, no. 6, pp. 2259–2267, 2018.
- [31] M. Souzanchi-K., A. Arab, M.-R. Akbarzadeh-T., and M. M. Fateh, “Robust impedance control of uncertain mobile manipulators using time-delay compensation,” *IEEE Transactions on Control Systems Technology*, vol. 26, no. 6, pp. 1942–1953, 2018.
- [32] S. Ding, L. Liu, and J. H. Park, “A novel adaptive nonsingular terminal sliding mode controller design and its application to active front steering system,” *International Journal of Robust and Nonlinear Control*, vol. 29, no. 12, pp. 4250–4269, 2019.
- [33] Z. Wang, S. Ge, and T. Lee, “Robust motion/force control of uncertain holonomic/nonholonomic mechanical systems,” *IEEE/ASME Transactions on Mechatronics*, vol. 9, no. 1, pp. 118–123, 2004.
- [34] J. Su and W.-H. Chen, “Further results on “reduced order disturbance observer for discrete-time linear systems”,” *Automatica*, vol. 93, pp. 550–553, 2018.
- [35] J. Yang, J. Sun, W. X. Zheng, and S. Li, “Periodic event-triggered robust output feedback control for nonlinear uncertain systems with time-varying disturbance,” *Automatica*, vol. 94, pp. 324–333, 2018.
- [36] J. Yang and W. X. Zheng, “Offset-free nonlinear mpc for mismatched disturbance attenuation with application to a static var compensator,” *IEEE Transactions on Circuits and Systems II: Express Briefs*, vol. 61, no. 1, pp. 49–53, 2013.
- [37] J. Cheng, J. H. Park, H. R. Karimi, and H. Shen, “A flexible terminal approach to sampled-data exponentially synchronization of markovian neural networks with time-varying delayed signals,” *IEEE Transactions on Cybernetics*, vol. 48, no. 8, pp. 2232–2244, 2017.
- [38] S. Gambhire, D. R. Kishore, P. Londhe, and S. Pawar, “Review of sliding mode based control techniques for control system applications,” *International Journal of Dynamics and Control*, vol. 9, pp. 363–378, 2021.

- [39] Y. Xu, “Chattering free robust control for nonlinear systems,” *IEEE Transactions on Control Systems Technology*, vol. 16, no. 6, pp. 1352–1359, 2008.
- [40] J.-J. Slotine and S. S. Sastry, “Tracking control of non-linear systems using sliding surfaces, with application to robot manipulators,” *International journal of control*, vol. 38, no. 2, pp. 465–492, 1983.
- [41] V. I. Utkin, *Sliding modes in control and optimization*. Springer Science & Business Media, 2013.
- [42] A. Levant, “Principles of 2-sliding mode design,” *automatica*, vol. 43, no. 4, pp. 576–586, 2007.
- [43] S. Shi, S. Xu, B. Zhang, Q. Ma, and Z. Zhang, “Global second-order sliding mode control for nonlinear uncertain systems,” *International Journal of Robust and Nonlinear Control*, vol. 29, no. 1, pp. 224–237, 2019.
- [44] Y. Pan, C. Yang, L. Pan, and H. Yu, “Integral sliding mode control: Performance, modification, and improvement,” *IEEE Transactions on Industrial Informatics*, vol. 14, no. 7, pp. 3087–3096, 2018.
- [45] S. S. Ge, Z. Wang, and T. H. Lee, “Adaptive stabilization of uncertain nonholonomic systems by state and output feedback,” *Automatica*, vol. 39, no. 8, pp. 1451–1460, 2003.
- [46] Y. Hu, S. Ge, and C.-Y. Su, “Stabilization of uncertain nonholonomic systems via time-varying sliding mode control,” *IEEE Transactions on Automatic Control*, vol. 49, no. 5, pp. 757–763, 2004.
- [47] G. P. Incremona, M. Rubagotti, and A. Ferrara, “Sliding mode control of constrained nonlinear systems,” *IEEE Transactions on Automatic Control*, vol. 62, no. 6, pp. 2965–2972, 2017.
- [48] S. Ding, K. Mei, and S. Li, “A new second-order sliding mode and its application to nonlinear constrained systems,” *IEEE Transactions on Automatic Control*, vol. 64, no. 6, pp. 2545–2552, 2019.
- [49] M. Sarfraz, F. u. Rehman, and I. Shah, “Robust stabilizing control of nonholonomic systems with uncertainties via adaptive integral sliding mode: an underwater vehicle example,” *International Journal of Advanced Robotic Systems*, vol. 14, no. 5, p. 1729881417732693, 2017.
- [50] T. d. J. M. Sanguino, “50 years of rovers for planetary exploration: A retrospective review for future directions,” *Robotics and Autonomous Systems*, vol. 94, pp. 172–185, 2017.
- [51] G. Campion, G. Bastin, and B. Dandrea-Novel, “Structural properties and classification of kinematic and dynamic models of wheeled mobile robots,” *IEEE Transactions on Robotics and Automation*, vol. 12, no. 1, pp. 47–62, 1996.
- [52] Y. Kanayama, Y. Kimura, F. Miyazaki, and T. Noguchi, “A stable tracking control method for an autonomous mobile robot,” in *Proceedings., IEEE International Conference on Robotics and Automation*, pp. 384–389, IEEE, 1990.

- [53] J.-M. Yang and J.-H. Kim, "Sliding mode control for trajectory tracking of nonholonomic wheeled mobile robots," *IEEE Transactions on robotics and automation*, vol. 15, no. 3, pp. 578–587, 1999.
- [54] H. Ashrafiuon, S. Nersesov, and G. Clayton, "Trajectory tracking control of planar underactuated vehicles," *IEEE transactions on automatic control*, vol. 62, no. 4, pp. 1959–1965, 2016.
- [55] B. d'Andréa Novel, G. Campion, and G. Bastin, "Control of nonholonomic wheeled mobile robots by state feedback linearization," *The International journal of robotics research*, vol. 14, no. 6, pp. 543–559, 1995.
- [56] D. Wang and G. Xu, "Full-state tracking and internal dynamics of nonholonomic wheeled mobile robots," *IEEE/ASME Transactions on mechatronics*, vol. 8, no. 2, pp. 203–214, 2003.
- [57] X. Yun and Y. Yamamoto, "Stability analysis of the internal dynamics of a wheeled mobile robot," *Journal of Robotic Systems*, vol. 14, no. 10, pp. 697–709, 1997.
- [58] J. Pliego-Jiménez, R. Martínez-Clark, C. Cruz-Hernández, and A. Arellano-Delgado, "Trajectory tracking of wheeled mobile robots using only cartesian position measurements," *Automatica*, vol. 133, p. 109756, 2021.
- [59] Z. Wang, G. Li, X. Chen, H. Zhang, and Q. Chen, "Simultaneous stabilization and tracking of nonholonomic wmsr with input constraints: Controller design and experimental validation," *IEEE Transactions on Industrial Electronics*, vol. 66, no. 7, pp. 5343–5352, 2019.
- [60] P. Kachroo and M. Tomizuka, "Vehicle traction control and its applications," 1994.
- [61] H.-S. Tan and M. Tomizuka, "A discrete-time robust vehicle traction controller design," in *1989 American Control Conference*, pp. 1053–1060, IEEE, 1989.
- [62] K. Jalali, T. Uchida, J. McPhee, and S. Lambert, "Development of a fuzzy slip control system for electric vehicles with in-wheel motors," *SAE International Journal of Alternative Powertrains*, vol. 1, no. 1, pp. 46–64, 2012.
- [63] G. Mauer, "A fuzzy logic controller for an abs braking system," *IEEE Transactions on Fuzzy Systems*, vol. 3, no. 4, pp. 381–388, 1995.
- [64] S. K. Mazumdar and C. C. Lim, "The application of neural networks to anti-skid brake system design," in *Proceedings of ICNN'95-International Conference on Neural Networks*, vol. 5, pp. 2409–2414, IEEE, 1995.
- [65] D. Wang and C. B. Low, "Modeling and analysis of skidding and slipping in wheeled mobile robots: Control design perspective," *IEEE Transactions on Robotics*, vol. 24, no. 3, pp. 676–687, 2008.
- [66] C.-F. Huang and T.-J. Yeh, "Anti slip balancing control for wheeled inverted pendulum vehicles," *IEEE Transactions on Control Systems Technology*, vol. 28, no. 3, pp. 1042–1049, 2020.

- [67] H. A. Hashim and A. E. E. Eltoukhy, “Nonlinear filter for simultaneous localization and mapping on a matrix lie group using imu and feature measurements,” *IEEE Transactions on Systems, Man, and Cybernetics: Systems*, pp. 1–12, 2021.
- [68] H. A. Hashim and F. L. Lewis, “Nonlinear stochastic estimators on the special euclidean group  $se(3)$  using uncertain imu and vision measurements,” *IEEE Transactions on Systems, Man, and Cybernetics: Systems*, vol. 51, no. 12, pp. 7587–7600, 2021.
- [69] K. Noori and K. Jenab, “Fuzzy reliability-based traction control model for intelligent transportation systems,” *IEEE Transactions on Systems, Man, and Cybernetics: Systems*, vol. 43, no. 1, pp. 229–234, 2013.
- [70] Y. Zhou, H. Li, and L. Kneip, “Canny-vo: Visual odometry with rgb-d cameras based on geometric 3-d–2-d edge alignment,” *IEEE Transactions on Robotics*, vol. 35, no. 1, pp. 184–199, 2019.
- [71] Y. Zhou, G. Gallego, and S. Shen, “Event-based stereo visual odometry,” *IEEE Transactions on Robotics*, vol. 37, no. 5, pp. 1433–1450, 2021.
- [72] Z. Lei, P. Cui, H. Ju, and X. Peng, “Traction control on loose soil for a redundantly actuated mobile robot,” in *International Conference on Intelligent Robotics and Applications*, pp. 1155–1164, Springer, 2008.
- [73] Y. P. Li, M. H. Ang, and W. Lin, “Slip modelling, detection and control for redundantly actuated wheeled mobile robots,” in *2008 IEEE/ASME International Conference on Advanced Intelligent Mechatronics*, pp. 967–972, IEEE, 2008.
- [74] N. Sidek and N. Sarkar, “Dynamic modeling and control of nonholonomic mobile robot with lateral slip,” in *Third International Conference on Systems (icons 2008)*, pp. 35–40, IEEE, 2008.
- [75] Q. Lu, D. Zhang, W. Ye, J. Fan, S. Liu, and C.-Y. Su, “Targeting posture control with dynamic obstacle avoidance of constrained uncertain wheeled mobile robots including unknown skidding and slipping,” *IEEE Transactions on Systems, Man, and Cybernetics: Systems*, vol. 51, no. 11, pp. 6650–6659, 2021.
- [76] D. Tavernini, M. Metzler, P. Gruber, and A. Sorniotti, “Explicit nonlinear model predictive control for electric vehicle traction control,” *IEEE Transactions on Control Systems Technology*, vol. 27, no. 4, pp. 1438–1451, 2019.
- [77] D. M. Helmick, S. I. Roumeliotis, Y. Cheng, D. S. Clouse, M. Bajracharya, and L. H. Matthies, “Slip-compensated path following for planetary exploration rovers,” *Advanced Robotics*, vol. 20, no. 11, pp. 1257–1280, 2006.
- [78] R. Gonzalez, D. Apostolopoulos, and K. Iagnemma, “Improving rover mobility through traction control: simulating rovers on the moon,” *Autonomous Robots*, vol. 43, no. 8, pp. 1977–1988, 2019.

- [79] S. Wu, L. Li, Y. Zhao, and M. Li, "Slip ratio based traction coordinating control of wheeled lunar rover with rocker bogie," *Procedia Engineering*, vol. 15, pp. 510–515, 2011.
- [80] T. Kawabe, M. Nakazawa, I. Notsu, and Y. Watanabe, "A sliding mode controller for wheel slip ratio control system," *Vehicle system dynamics*, vol. 27, no. 5-6, pp. 393–408, 1997.
- [81] V. Ivanov, D. Savitski, and B. Shyrokau, "A survey of traction control and antilock braking systems of full electric vehicles with individually controlled electric motors," *IEEE Transactions on Vehicular Technology*, vol. 64, no. 9, pp. 3878–3896, 2014.
- [82] E. Reichensdörfer, D. Odenthal, and D. Wollherr, "On the stability of nonlinear wheel-slip zero dynamics in traction control systems," *IEEE Transactions on Control Systems Technology*, vol. 28, no. 2, pp. 489–504, 2020.
- [83] R. Gonzalez and K. Iagnemma, "Slippage estimation and compensation for planetary exploration rovers. state of the art and future challenges," *Journal of Field Robotics*, vol. 35, no. 4, pp. 564–577, 2018.
- [84] K. Iagnemma and C. C. Ward, "Classification-based wheel slip detection and detector fusion for mobile robots on outdoor terrain," *Autonomous Robots*, vol. 26, no. 1, pp. 33–46, 2009.
- [85] K. Iagnemma and S. Dubowsky, "Traction control of wheeled robotic vehicles in rough terrain with application to planetary rovers," *The international Journal of robotics research*, vol. 23, no. 10-11, pp. 1029–1040, 2004.
- [86] P. Lamon and R. Siegwart, "Wheel torque control in rough terrain-modeling and simulation," in *Proceedings of the 2005 IEEE international conference on robotics and automation*, pp. 867–872, IEEE, 2005.
- [87] N. Sarkar and X. Yun, "Traction control of wheeled vehicles using dynamic feedback approach," in *Proceedings. 1998 IEEE/RSJ International Conference on Intelligent Robots and Systems. Innovations in Theory, Practice and Applications (Cat. No. 98CH36190)*, vol. 1, pp. 413–418, IEEE, 1998.
- [88] L.-Y. Hsu and T.-L. Chen, "An optimal wheel torque distribution controller for automated vehicle trajectory following," *IEEE transactions on vehicular technology*, vol. 62, no. 6, pp. 2430–2440, 2013.
- [89] S. Barthelmes and U. Konigorski, "Model-based chassis control system for an over-actuated planetary exploration rover," *at-Automatisierungstechnik*, vol. 68, no. 1, pp. 58–71, 2020.
- [90] H. Guo, Z. Yin, D. Cao, H. Chen, and C. Lv, "A review of estimation for vehicle tire-road interactions toward automated driving," *IEEE Transactions on Systems, Man, and Cybernetics: Systems*, vol. 49, no. 1, pp. 14–30, 2019.
- [91] B. H. G. Barbosa, N. Xu, H. Askari, and A. Khajepour, "Lateral force prediction using gaussian process regression for intelligent tire systems," *IEEE Transactions on Systems, Man, and Cybernetics: Systems*, pp. 1–12, 2021.

- [92] A. Isidori, *Nonlinear control systems*. Springer Science & Business Media, 2013.
- [93] R. Hermann and A. Krener, “Nonlinear controllability and observability,” *IEEE Transactions on automatic control*, vol. 22, no. 5, pp. 728–740, 1977.
- [94] H. Nijmeijer and A. J. Van der Schaft, *Nonlinear dynamical control systems*, vol. 175. Springer, 1990.
- [95] D. E. Kirk, *Optimal control theory: an introduction*. Courier Corporation, 2004.
- [96] J.-J. E. Slotine, W. Li, *et al.*, *Applied nonlinear control*, vol. 199. Prentice hall Englewood Cliffs, NJ, 1991.
- [97] A. M. Bloch, M. Reyhanoglu, and N. H. McClamroch, “Control and stabilization of nonholonomic dynamic systems,” *IEEE Transactions on Automatic control*, vol. 37, no. 11, pp. 1746–1757, 1992.
- [98] D. P. Bertsekas, “Nonlinear programming,” *Journal of the Operational Research Society*, vol. 48, no. 3, pp. 334–334, 1997.
- [99] “Vortex studio release 6.8.1,” tech. rep., CM Labs Simulations Inc., Montreal, Canada.
- [100] H. Özakıyol, C. Karaman, and Z. Bingul, “Robotics toolbox for kinematic analysis and design of hybrid multibody systems,” pp. 401–406, 07 2017.
- [101] A. Enzenhöfer, S. Andrews, M. Teichmann, and J. Kövecses, “Comparison of mixed linear complementarity problem solvers for multibody simulations with contact,” in *VRIPHYS*, 2018.
- [102] A. Peiret, E. Karpman, L. L. Kovács, J. Kövecses, D. Holz, and M. Teichmann, “Modelling of off-road wheeled vehicles for real-time dynamic simulation,” *Journal of Terramechanics*, vol. 97, pp. 45–58, 2021.
- [103] E. M. Botta, C. Miles, and I. Sharf, “Simulation and tension control of a tether-actuated closing mechanism for net-based capture of space debris,” *Acta Astronautica*, vol. 174, pp. 347–358, 2020.
- [104] “Theory guide: Vortex software’s multibody dynamics engine,” tech. rep., CM Labs Simulations Inc., Montreal, Canada.

## Appendix A

### Matrices $\hat{M}$ and $\hat{C}$

The nonzero elements of the matrix  $\hat{M}$  are:

$$\begin{aligned}
 \hat{M}_{1,1} &= \hat{M}_{2,2} = m_r + 6m_w, \\
 \hat{M}_{1,3} &= \hat{M}_{3,1} = (2(L_0 - L)m_w - x_{cm}m_r) \sin(\theta) - y_{cm}m_r \cos(\theta), \\
 \hat{M}_{2,3} &= \hat{M}_{3,2} = 2m_w(L - L_0) \cos(\theta) + m_r(x_{cm} \cos(\theta) - y_{cm} \sin(\theta)), \\
 \hat{M}_{3,3} &= 6(m_w c^2 + J_{wz}) + 2m_w(L^2 + L_0^2) + m_r(x_{cm}^2 + y_{cm}^2 + J_r), \\
 \hat{M}_{3,5} &= \hat{M}_{5,3} = \hat{M}_{3,11} = \hat{M}_{11,3} = \hat{M}_{5,5} = \hat{M}_{11,11} = J_{wz}, \\
 \hat{M}_{4,4} &= \hat{M}_{6,6} = \dots = \hat{M}_{10,10} = J_{wy},
 \end{aligned}$$

where  $m_r$  is the mass of the main body,  $m_w$  is the mass of the wheels,  $J_r$  is the moment of inertia of the main body about the  $z$ -axis (out of the plane) at its center of mass,  $J_{wy}$  denotes the moment of inertia of the wheels about their axes of rotation, and  $J_{wz}$  is the the moment of inertia of the wheels about the  $z_0$ -axis. Accordingly, based on the Lagrange d'Alembert principle, the matrix  $\hat{C}$  is obtained as

$$\hat{C}(\theta, \dot{\hat{\mathbf{q}}}) = \left( \frac{\partial \hat{M}}{\partial \theta} \right) \dot{\theta} + [\mathbb{O}_{2 \times 11} \quad , \quad \frac{1}{2} \dot{\hat{\mathbf{q}}}^T \frac{\partial \hat{M}}{\partial \theta} \quad , \quad \mathbb{O}_{8 \times 11}]^T$$

## Appendix B

### Matrices $A_l$ and $B_l$

The nonzero elements of the constant matrix  $A_L$  in (4.20) are:

$$\begin{aligned}A_{L1,3} &= A_{L2,4} = A_{L3,5} = A_{L4,6} = 1 \\A_{L5,11} &= -\frac{1}{K_{v1,1}} \\A_{L6,12} &= -\frac{1}{K_{v2,2}} \\A_{L9,3} &= -K_{e1,1} \\A_{L10,4} &= -K_{e2,2} \\A_{L9,7} &= A_{L10,8} = A_{L11,9} = A_{L12,10} = -1\end{aligned}$$

where  $A_{Li,j}$  refers to the element  $(i, j)$  of the matrix  $A_L$ ,  $K_{vi,j}$  denotes the element  $(i, j)$  of the weighting matrix  $K_v$ , and  $K_{ei,j}$  denotes the element  $(i, j)$  of the weighting matrix  $K_e$ . Choosing the weighting matrices  $K_v$  and  $K_e$  as the identity matrix, and selecting  $t_f = 10$ s the determinant of the matrix  $B_{Lf1,2}$  is  $1.54 \times 10^{12}$ ; and hence this matrix is well-conditioned.